A Non-Dimensional Framework for Colloidal Aggregation Based on DLVO-Theory: A Coarse-Grained Simulation Study

Application to Molten Salt Reactors

MSc. Thesis Applied Physics
P.A. Jager

Delft University of Technology

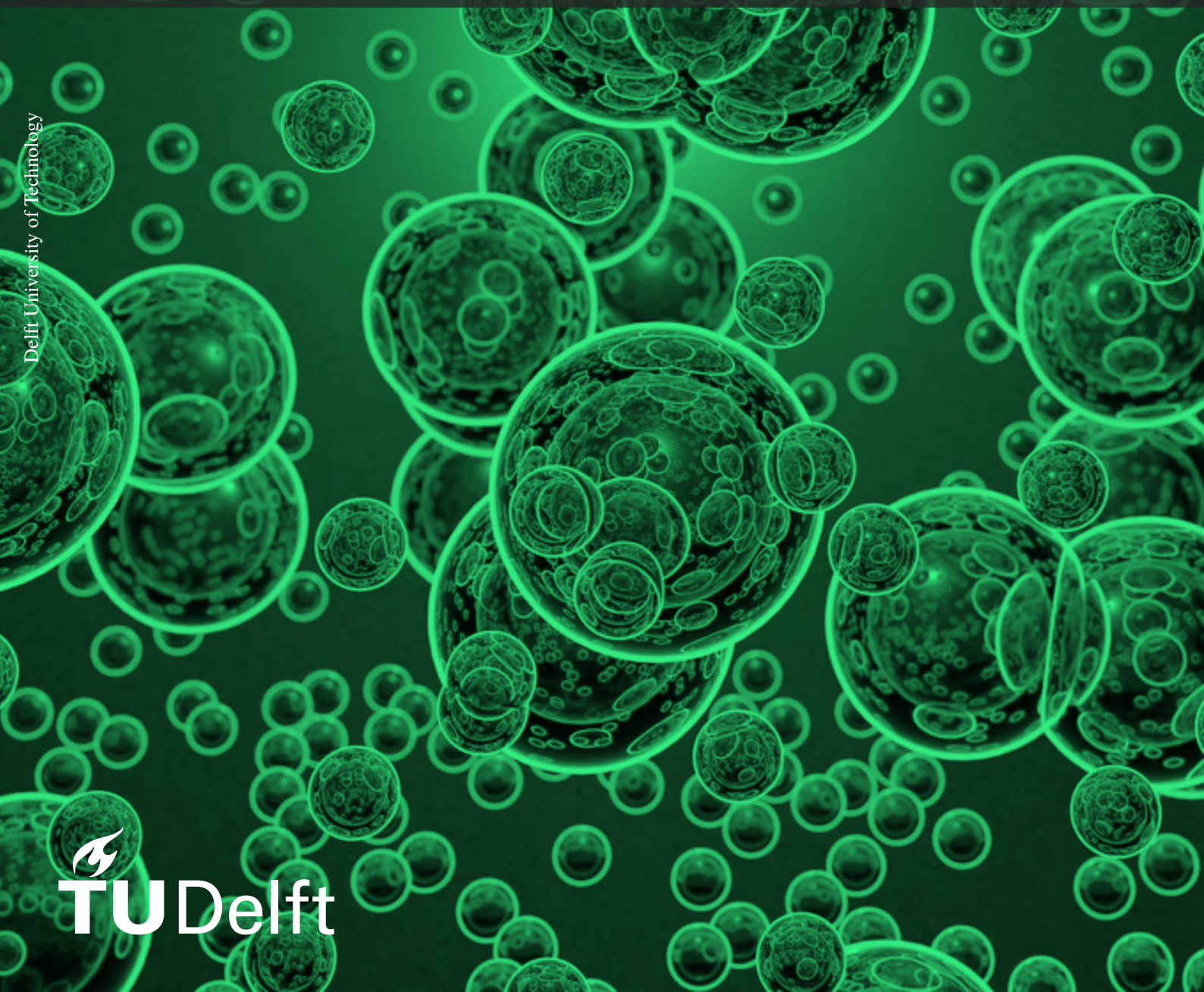

TU Delft

A Non-Dimensional Framework for Colloidal Aggregation Based on DLVO-Theory: A Coarse-Grained Simulation Study

Application to Molten Salt Reactors

by

P.A. Jager

to obtain the degree of Master of Science at the Delft University of Technology,
to be defended publicly on Friday November 14, 2025 at 14:00.

Student number:	4729161	
Project duration:	March 1, 2025 – November 3, 2025	
Thesis committee:	Prof. dr. ir. M. Rhode,	Supervisor
	PhD candidate N. Mischenko	Daily Supervisor
	Dr. ir. R. Hartkamp	
	Dr. W. Bouwman	

Cover: Cover from Journal of Colloid And Interface Science

An electronic version of this thesis is available at `http://repository.tudelft.nl/`.

TU Delft

Abstract

Nanoparticle (NP) aggregation plays a crucial role in NP synthesis, which is increasingly relevant due to the favourable surface-to-volume properties of NPs. In molten salt reactors (MSRs), insoluble solid fission products (SFPs) form metallic nanoparticles that can aggregate and deposit on internal reactor components, reducing heat-transfer performance and complicating maintenance. Although the classical DLVO theory describes the aggregation kinetics, its predictive use is limited by the large number of system-specific parameters involved. Moreover, literature indicates that aggregation behaviour is typically examined qualitatively and on a case-by-case basis, lacking a general theory to relate different systems.

This thesis presents the development of a novel general non-dimensional framework that is based on DLVO theory. The framework reduces the DLVO potential parameters to two key coefficients, representing the relative strength and relative interaction of the electric double layer (EDL). Their combination uniquely defines the shape of the potential and enables classification of aggregation regimes: rapid aggregation, barrier-limited aggregation, or stable dispersion. The framework is applied to both sphere–sphere and sphere–plate geometries to capture bulk aggregation and sedimentation.

The framework is implemented and used in coarse grained (CG) molecular dynamics (MD) simulations to establish a first quantitative relation between the two key coefficients and aggregation kinetics. NPs are represented as spherical particles interacting through the dimensionless DLVO potential and the molten salt medium modelled using neutral beads interacting through a Lennard-Jones (LJ) potential. A parameter sweep across the non-dimensional coefficients quantifies the aggregation time and final cluster size with statistical certainty. The results demonstrate that the dimensionless coefficients are able to predict the aggregation behaviour. For MSR conditions, the coefficients place the system deep into the primary-minimum aggregation regime, indicating that metallic NPs will aggregate regardless of surface charge.

The developed framework allows for a first prediction on aggregation behaviour. Future research should focus on refining the CG simulation model, extending it to three dimensions and validating the results with experimental measurements. Additional insight is acquired by exploring concentration-dependent aggregation and extending the sphere-sphere framework beyond the near-field approximation.

Contents

Nomenclature

Abbreviations

Abbreviation	Definition
AI	Artificial Intelligence
CCA	Constant Charge Approximation
CG	Coarse-Grained
CPA	Constant Potential Approximation
CFD	Computational Fluid Dynamics
CV	Coefficient of Variation
DLVO	Derjaguin–Landau–Verwey–Overbeek (theory of colloidal stability)
EDL	Electric Double Layer
ENDURANCE	EU kNowleDge hUb foR enAbling MolteN Salt ReaCtor safety development and deployment
EOS	Equation of State
LAMMPS	Large-scale Atomic/Molecular Massively Parallel Simulator
LJ	Lennard-Jones
LSA	Linear Superposition Approximation
MD	Molecular Dynamics
MIMOSA	MultI-scale MOdeling for SAfety evaluation of MSR fuel systems
MSR	Molten Salt Reactor
MSRE	Molten Salt Reactor Experiment
NF	Near Field
NP	NanoParticle
NPT	Isothermal–isobaric ensemble
NVE	Microcanonical ensemble
NVT	Canonical ensemble
ORNL	Oak Ridge National Laboratory
PBC	Periodic Boundary Conditions
RID	Reactor Institute Delft
SFP	Solid Fission Product
SP	Sphere-Plate
SS	Sphere-Sphere
VdW	van der Waals

Symbols

Symbol	Definition	Unit
Background Theory		
$U(h)$	DLVO interaction potential as function of separation h	J
$U_{\text{Tot}}(h)$	Total interaction potential (sum of contributions)	J
$U_{ss}(h)$	DLVO potential for sphere–sphere interaction	J
$U_{sp}(h)$	DLVO potential for sphere–plate interaction	J
h	Surface-to-surface separation distance	m
$\rho(r)$	Charge density	$\mathrm{C\,m^{-3}}$
$\Phi(r)$	Dimensionless electrostatic potential	–
ϕ	Electric potential (dimensional)	V
ϕ_0	Electric potential at the surface	V
a_1, a_2	Radii of interacting spheres (sphere–sphere geometry)	m
a	Sphere radius (sphere–plate geometry)	m
A	Hamaker constant (van der Waals attraction strength)	J
σ_c	Collision/ionic diameter	m
Γ, Δ	Auxiliary geometric functions in DLVO expressions	–
I	Ionic strength	$\mathrm{mol\,m^{-3}}$
c_i	Concentration of ionic species i	$\mathrm{mol\,m^{-3}}$
z_i	Valence of ionic species i	–
E	Electric field strength	$\mathrm{V\,m^{-1}}$
G	Gibbs free energy	J
κ	Inverse Debye length (screening parameter)	$\mathrm{m^{-1}}$
λ_D	Debye length	m
ε	Permittivity of medium ($\varepsilon = \varepsilon_0\varepsilon_r$)	$\mathrm{F\,m^{-1}}$
ε_0	Permittivity of vacuum	$\mathrm{F\,m^{-1}}$
ε_r	Relative permittivity	–
γ_1, γ_2	Surface potential factors (symmetric electrolyte)	–
n	Born exponent (typically $n = 12$)	–
Interaction Potentials		
U_{Tot}	Total interaction potential (sum of contributions)	J
$U_{ss}(h)$	DLVO potential for sphere–sphere interaction	J
$U_{sp}(h)$	DLVO potential for sphere–plate interaction	J
$U^{ss,nf}(h)$	Near–field sphere–sphere DLVO potential	J
$U_{VdW}(h)$	Van der Waals interaction potential	J
$U_B(h)$	Born interaction potential	J
$U_{LSA}(h)$	Electric repulsion potential with LSA approximation	J
h	Surface-to-surface separation distance	m
$f(a,h'), g(a,h')$	Auxiliary geometric functions (sphere–plate)	–
k_BT	Thermal energy scale	J
Non-dimensional parameters		
$U'(h')$	Dimensionless DLVO interaction potential	–
h'	Dimensionless separation distance	–
B	Born repulsion prefactor	$\mathrm{J\,m^{-7}}$
C	Electrostatic repulsion prefactor	J
D	Van der Waals attraction prefactor	$\mathrm{J\,m^{-1}}$
B', C', D'	Dimensionless DLVO prefactors (sphere–sphere)	–
B'_{sp},C'_{sp},D'_{sp}	Dimensionless DLVO prefactors (sphere–plate)	–
B'/D'	Dimensionless coefficient from DLVO (relative length EDL)	–
C'/D'	Dimensionless coefficient from DLVO (relative length EDL)	–

Symbol	Definition	Unit
B'_{sp}/D'_{sp}	Dimensionless coefficient from DLVO (sphere-plate)	–
C'_{sp}/D'_{sp}	Dimensionless coefficient from DLVO (sphere-plate)	–
Post-Processing		
$R(t)$	Time dependent average cluster radius	–
R_∞	Steady state average cluster radius at end of simulation	–
R_{init}	Initial average cluster	–
k	Growth constant, difference between initial and end cluster radii	m
t_{agg}	Characteristic aggregation time	s
$\mu(x)$	Mean	–
$\sigma_{std}(x)$	Standard deviation	–
$CV(x)$	Coefficient of variation	–
Simulation parameters		
Δt	MD integration timestep	s
k	Number of integration steps per aggregation block (merge interval)	–
n	Sampling stride for loggers (record every nth step)	–
N_{types}	Number of particle types in the coarse-grained model	–
σ_{cg}	Coarse-grained LJ size parameter (bead diameter)	m
ϵ_{cg}	Coarse-grained LJ energy parameter	J
n_{cg}	Number of atoms represented per coarse-grained bead	–
Subscripts		
ss	Sphere–sphere interaction geometry	
nf	Near field approximation regime	
sp	Sphere–plate interaction geometry	

Symbol	Name	Value (SI units)
k_B	Boltzmann constant	$1.380\,649 \cdot 10^{-23}$ J K^{-1}
N_A	Avogadro constant	$6.022\,140\,76 \cdot 10^{23}$ mol^{-1}

1

Introduction

The Dutch electricity grid is currently under significant strain, with over 14 000 companies waiting for a new or upgraded connection due to network congestion and limited capacity [27]. At the same time, peak-hour loads are increasing sharply as solar and wind power generation fluctuate and industries adopt energy-intensive technologies such as artificial intelligence and large-scale data centres [60]. In this context, nuclear reactors could provide a solution: they supply continuous, high-capacity energy and can deliver process heat for industry and hydrogen production. The benefits will stabilise the grid, meet increasing demand, and enable decarbonisation of sectors that cannot rely solely on renewables. These hard to electrify sectors include heavy industry and long-distance transport, because they have high energy demands and rely on fuels with high energy densities. Advanced nuclear reactors can also deliver high-temperature process heat and enable efficient hydrogen production, helping to decarbonize industrial processes [52, 32].

Molten salt reactors (MSRs) are one of the nuclear reactor types that are to be considered and growing in popularity [28]. MSRs offer additional advantages over conventional nuclear designs. They operate at lower pressures and higher temperatures, improving thermodynamic efficiency. They also support flexible fuel cycles while reducing long-lived waste and enhancing resource utilisation [1]. International assessments indicate that advanced fuel cycles compatible with MSR technology can substantially reduce the volume and long-lived radiotoxicity of nuclear waste by keeping radioactive waste in circulation for further fission [33]. Furthermore, their liquid-fuel configuration maintains strong negative temperature coefficients for inherent safety [79]. Lastly, high-temperature operation allows direct coupling to industrial heat applications, enabling efficient manufacturing and hydrogen-production processes that traditional reactors struggle to support [35].

However, molten salt reactors also face several challenges. The materials used in the primary loop must withstand corrosive salt chemistry, elevated temperatures and radiation over extended periods of time. Additionally, the liquid state of the fuel introduces complexity in the behaviour of fission products [87]. Soluble fission products remain dissolved in the molten salt, altering the chemical composition and the redox potential of the fuel. Lastly, insoluble fission products remain suspended in the salt and eventually deposit on internal components such as pumps, heat exchangers or piping surfaces, which reduces heat transfer performance and can lead to localised hot spots [69, 14]. Understanding the transport, aggregation and removal of these species is therefore essential for the safe and reliable operation of molten salt reactors. To address these challenges, the Reactor Institute Delft of TU Delft participates in the European research programmes funded under EURATOM: the ENDURANCE project.

The ENDURANCE project (EU Knowledge Hub for enabling Molten Salt Reactor safety development and deployment) focuses on improving the technological readiness of molten salt reactor systems [9]. Its goal is to identify and develop critical technology elements required for safe industrial deployment. The project connects reactor designers, industry, research institutes and regulatory bodies, and provides a coordinated European roadmap for molten salt reactor development. TU Delft, through the Reactor Institute Delft, contributes experimental capability and modelling expertise.

The objective of this work is to support the ENDURANCE programme by developing a framework for predicting aggregation behaviour in systems where DLVO-theory could be applied. The interaction potential is expressed in a dimensionless form to identify dominant physical effects independently of specific material properties. Ana-

lytical stability maps are constructed to classify regions of rapid aggregation, barrier limited aggregation, stable dispersion, and intermediate semi-stable regimes. Complementary, this framework is applied in coarse-grained molecular dynamics simulations of MSRs. The results are used to investigate how these dimensionless parameters translate into aggregation kinetics, including cluster growth rates and final aggregate size. Together, the theoretical and numerical components establish a predictive methodology for assessing aggregation kinetics of colloidal systems.

Thesis Outline

Outline of this thesis is as follows: Chapter 2 contains the project background, scope definition and research objectives. The thesis is then divided into two main parts. The first part focuses on the theoretical development of a generalized, non-dimensional framework derived from DLVO theory and encompasses Chapters 3 to 5. The second part applies this framework to coarse-grained simulations of noble metals in a molten salt, covered in Chapters 6 to 8.

In Part I, Chapter 3 introduces the theoretical background of the electric double layer and the individual interaction potentials that constitute DLVO theory, complemented. Chapter 4 presents the non-dimensionalisation of the total interaction potential, in which the physical parameters are reduced to two governing dimensionless quantities. Chapter 5 visualizes the outcomes of this analysis, that define the different aggregation regimes as a function of these dimensionless parameters.

In Part II, Chapter 6 begins with introducing the principles of molecular dynamics and highlighting the key differences between atomistic and coarse-grained simulations. Chapter 7 describes the methods used to perform the coarse-grained simulations, including system setup, parameter selection, and data processing. Finally, Chapter 8 presents and analyses the simulation results, focusing on the relationship between the non-dimensional parameters and the observed aggregation rates.

Chapter 9 discusses the implications of these findings and addresses future recommendations of the current model. Finally, Chapter 10 summarizes the main conclusions.

REACTOR INSTITUTE DELFT

ENDURANCE

2

Project Background

This chapter introduces the background required for the remainder of this research. It first provides a brief overview of colloidal systems, after which the relevance of Molten Salt Reactors (MSRs) is discussed. An introduction to colloidal systems is given in Section 2.1. Subsequently, Section 2.2 introduces the context for MSRs. Section 2.3 refines the scope and specifies the boundaries relevant to this study. Section 2.4 presents a review on present literature on the subjects: insoluble fission products, nanoparticle aggregation and coarse-grained molecular simulations of ionic liquids. Finally, Section 2.5 presents the motivation and research objectives of this thesis.

2.1. Colloidal Systems

Colloidal systems consist of dispersed particles with sizes typically ranging from 1 to 1000 nm, suspended in a medium. A key characteristic of colloids is the Tyndall effect [40]. The Tyndall effect refers to the scattering of light by particles, which makes a light beam visible when it passes through the dispersed system. True solutions do not show this effect, because ions or molecular solutes are too small to scatter light.

Colloids are commonly classified based on the phase of the dispersed particles relative to the phase of the medium. The most frequently encountered types include sols (solid in liquid), emulsions (liquid in liquid), foams (gas in liquid), and aerosols (solid in gas). Representative examples of each type are listed in Table 2.1.

Table 2.1: Types of colloidal dispersions [55].

Type name	Dispersed phase	Dispersion medium	Examples
Solid sol	Solid	Solid	Ruby glass, alloys
Sol	Solid	Liquid	Paint, ink
Smoke	Solid	Gas	Dust
Solid emulsion (gel)	Liquid	Solid	Butter, cheese
Emulsion	Liquid	Liquid	Milk, hair cream
Aerosol	Liquid	Gas	Fog, mist, clouds
Solid foam	Gas	Solid	Froth cork, pumice stone, foam rubber
Foam	Gas	Liquid	Whipped cream, shaving cream, soda-water

This research focuses on sols, where solid particles are dispersed in a liquid medium. These solid particles are also referred to as NanoParticles (NPs). A key feature of sols is the electrostatic interaction between NPs. They typically carry either a positive or negative surface charge. This charge originates from the adsorption of ions or from the presence of free electrons at the particle surface [55]. The resulting electrostatic repulsion between particles of equal charge helps to prevent aggregation and sedimentation. In addition, charged particles are surrounded by a layer of counter-ions that forms the Electric Double Layer (EDL)[55]. The interplay between attractive forces and electrostatic repulsion determines whether particles aggregate or remain dispersed. The clas-

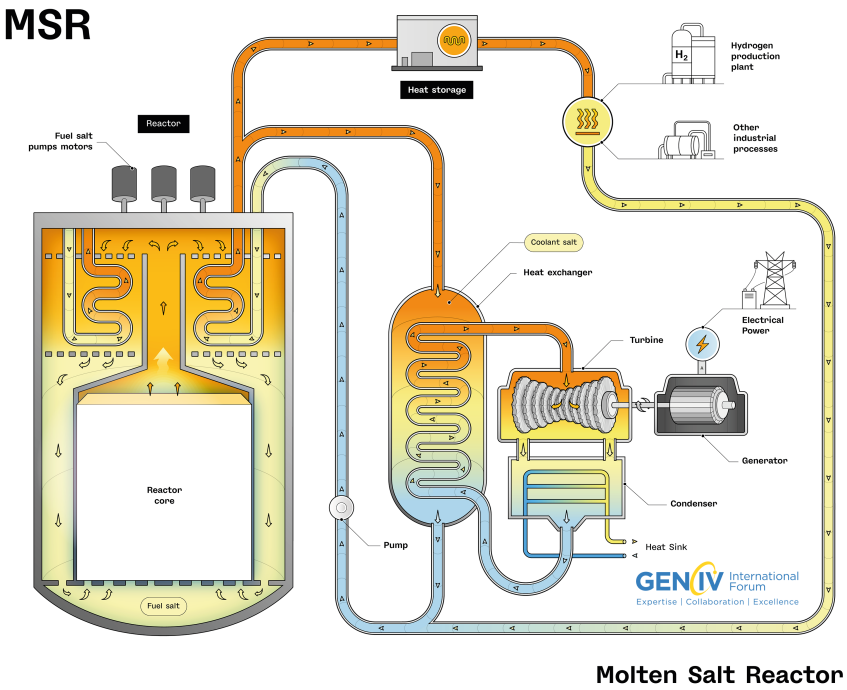

Figure 2.1: Schematic representation of a molten salt reactor (MSR). The fuel salt circulates through the reactor core where fission heat is generated, after which thermal energy is transferred to a secondary coolant salt loop through a heat exchanger. The secondary loop drives a power conversion system or supplies heat to external industrial processes [18].

sical Derjaguin–Landau–Verwey–Overbeek (DLVO) theory describes these interactions and predicts the stability of colloidal systems. A more detailed theoretical background is provided in Chapter 3.

Recent years have shown an increase in research on metal NPs, which is driven by their wide applicability in industrial sectors [3]. In particular, metallic NPs are frequently used as catalysts in chemical processes, such as the reverse water–gas shift reaction [38]. Beyond catalysis, NPs are applied across multiple fields including biology, medicine, and pharmaceutical sciences. Their applicability has resulted in a significant need for better production of such NPs [77].

Another relevant example of a colloidal system is the presence of solid fission products (SFPs) suspended in the molten salt of a MSR. The SFPs eventually deposit on internal components such as pumps, heat exchangers or piping surfaces, which reduces heat transfer performance and can lead to localised hot spots [69, 14]. Understanding the transport, aggregation and removal of these species is therefore essential for the safe and reliable operation of molten salt reactors.

From this point, the focus shifts to the aggregation of SFPs in the MSR, which has been the primary motivation for this research. Although the MSR serves as the central case study, the objective remains to develop a general framework that can be applied to other colloidal systems. The MSR context is used to validate and quantify the aggregation behaviour in the simulations. Therefore, all simulations are performed using physical properties representative of MSR operating conditions. The next section introduces the context needed for SFP aggregation in MSRs.

2.2. Case Study Introduction: Molten Salt Reactor

Figure 2.1 illustrates the workflow of a molten salt reactor. The fuel salt, which contains dissolved fissile material, circulates through the reactor core where fission heat is generated. The molten salt acts both as fuel and as primary coolant, absorbing the released heat while simultaneously transporting the fuel through the system.

The heated salt exits the core and transfers its thermal energy to a secondary salt loop through a heat exchanger. The secondary loop drives a turbine cycle, where the heat is converted into mechanical work and subsequently into electrical power. After heat extraction, the cooled secondary salt returns to the heat exchanger, completing the

circulation loop. A portion of the thermal energy can be directed to alternative applications, including hydrogen production, water desalination and industrial process heat [18].

The molten salt provides an inherent negative temperature coefficient of reactivity. As the temperature increases, the salt expands and the density of fissile material decreases. This reduction in fissile density lowers the probability of neutron absorption and fission events, which stabilises the power output. The effect is purely thermophysical and does not rely on mechanical control systems, which contributes to the intrinsic safety characteristics of molten salt reactors [16].

At the same time, the liquid fuel introduces complexity. Fission products formed during reactor operation dissolve, remain suspended or appear in gaseous form, each with different implications. These fission products can be classified into three groups. Gaseous fission products migrate to the free surface of the salt and are removed through the off-gas system. Soluble fission products form ionic species with the carrier salt and alter thermophysical properties such as density, viscosity and heat capacity. Solid fission products remain as particles within the salt and aggregate to NPs and deposit on internal surfaces. Understanding the kinetics and deposition interaction of these SFPs is necessary for predicting long-term reactor performance and defining appropriate operational and safety limits.

2.2.1. Solid Fission Products

During the Molten Salt Reactor Experiment (MSRE) at Oak Ridge National Laboratory (ORNL), the first operational demonstration of molten salt reactor technology, it was observed that a fraction of the fission products formed metallic nanoparticles. These particles were found either suspended in the circulating salt or deposited on internal surfaces of the reactor loop. The distribution of deposited material was shown to depend on the fissile isotope used, either ^{235}U or ^{233}U, due to differences in the fission product inventory and operating conditions. Post-operation analysis identified several noble metal isotopes formed through decay chains, including ^{99}Mo, ^{103}Ru, ^{106}Ru, $^{129\mathrm{m}}$Te, ^{132}Te and ^{95}Nb. Table 2.2 summarises the relevant fission product parameters for ^{235}U operation, as reported in the MSRE documentation [37].

Table 2.2: Noble metal fission product parameters for ^{235}U runs, based on MSRE data.

Noble Metal	Cumulative Yield of Precursor (%)	Half-Life of Precursor	Half-Life of Noble Metal
^{99}Mo	6.06	2.4 min	66.5 h
^{103}Ru	3.00	1.2 min	39.7 days
^{106}Ru	0.39	$<$1 min	1.01 yr
^{129m}Te	0.71	4.6 h	37 days
^{132}Te	4.71	2.1 min	77 h
^{95}Nb	6.22	65 days	35 days

Among these, molybdenum (Mo) and niobium (Nb) were identified as the dominant noble metals deposited on the reactor walls.

2.2.2. SFP Life Cycle

The life cycle of SFPs in a MSR begins with their formation during the fission of nuclear fuel. These fission products are generated either directly from the fission event or indirectly through the decay of precursor isotopes. Initially, sole fission products (single atoms) are dispersed in the molten salt, gradually increasing their concentration within the liquid phase.

Nucleation marks the onset of a new phase formation. In the context of an MSR, SFPs transition from individual atoms dissolved in the molten salt to NPs that are no longer soluble. The individual atoms are called ”dissolved” but they do not make bonds with the solvent. The atoms can only be called a solid after enough have clustered together to reach a size where the bulk properties become apparent. According to Classical Nucleation Theory (CNT), this process, termed homogeneous nucleation, requires an energy barrier to be overcome before a stable nucleus can form [7]. As atoms are beginning to cluster, an interface between the liquid and solid phases develops and requires energy. This energy requirement often causes small clusters to fall back into single dissolved atoms. As the solute concentration increases, the probability of clusters encountering and attaching to other atoms rises, promoting growth beyond the critical radius. Once this critical radius is surpassed, the NP becomes thermodynamically stable and continues to grow spontaneously [53].

When NPs are present in the molten salt, their behavior is governed by a balance of interatomic and electrostatic forces. Larger NPs develop an electrostatic potential at their surface due to repulsion among free electrons [5]. The interaction between attractive van der Waals forces and repulsive electrostatic interactions determines their aggregation behavior and is described by DLVO theory [11, 76]. The NP life cycle is illustrated in Figure 2.2. Primary particles nucleate into small clusters, which subsequently aggregate into larger NPs and eventually deposit onto surfaces.

As NPs continue to grow, their motion becomes increasingly influenced by hydrodynamic and thermophoretic effects. Fluid turbulence can transport the particles toward the reactor walls, where they may adhere if the wall–particle interaction is sufficiently strong. At larger sizes, gravitational forces dominate, leading to gradual sedimentation of the NPs onto the reactor floor.

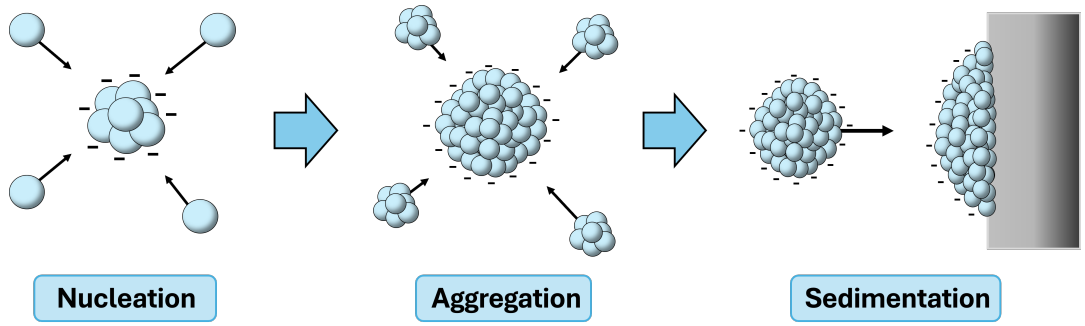

Figure 2.2: Schematic overview of nanoparticle evolution: nucleation of primary particles, aggregation into larger clusters, and sedimentation onto a surface. The "–" symbols indicate the negative surface charge

Summarising, deposition of SFPs presents a significant challenge in MSR operation. These deposits can contaminate equipment and the surrounding environment, will have corrosion effects on structural materials such as fuel cladding, and pose severe health risks due to their radioactivity [80]. As shown in Table 2.2, the relevant SFPs exhibit measurable half-lives, confirming their radioactive nature. During maintenance and repair activities, these deposits increase both the complexity and the hazard of the work, as personnel are exposed to elevated radiation levels [1]. These reasons stresses the fact that the MSR is a relevant case study for this research.

2.3. Scope Definition

Preliminary research led to a refinement of the project scope. Although the aggregation of solid fission products (SFPs) in a Molten Salt Reactor (MSR) was initially the primary objective, further investigation into the life cycle of SFPs and parameter variations of the DLVO potential revealed a more suitable scope. The scope has therefore been altered to the development of a general framework that captures aggregation kinetics using coarse-grained simulations, with an application to a MSR environment. The following sections justify the exclusion of nucleation and explain the motivation for developing a non-dimensional framework.

Exclusion of Nucleation

Nucleation represents the initial stage of NP formation and is driven by the minimization of the Gibbs free energy. It can be viewed as a chemical reaction in which individual atoms combine to form clusters. For example, when two atoms merge into a dimer. The Gibbs free energy barrier associated with the process of nucleation depends on the chemical potential of the liquid phase and must be overcome for a stable cluster to form. According to Classical Nucleation Theory (CNT), a cluster must reach a critical radius before it becomes thermodynamically stable and can continue to grow spontaneously. The Gibbs free energy barrier and the evolution of the free energy with particle radius are shown in Figure 2.3. The formation of stable clusters needs at least the same energy as the Gibbs free energy barrier ΔG^*. Cai and Kangasluoma [7] demonstrated that partial pressures of small clusters can also lower the Gibbs free energy barrier, allowing nucleation once the concentration of solute atoms becomes sufficiently high. Additionally, the process in which multiple species participate (heterogeneous nucleation) reduces this energy barrier as well and it will facilitate cluster formation. Both processes could make spontaneous nucleation of SFP's in MSRs possible.

Nucleation is inherently governed by chemical reactions and thermodynamic driving forces. Simulating this process realistically requires molecular-level models capable of tracking Gibbs free energy and enthalpy to ensure

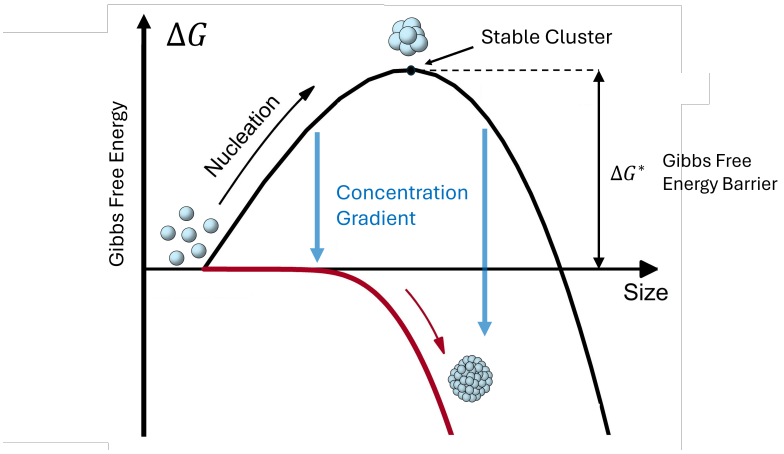

Figure 2.3: Gibbs free-energy profile of nucleation. Formation of a stable cluster requires overcoming the critical Gibbs free-energy barrier ΔG^*. As the concentration of primary particles increases, the reaction free energy decreases, promoting aggregation and stable nanoparticle growth.

that energy minimization is achieved at every timestep. In the case of MSRs, this becomes particularly complex because nuclear fission produces a wide range of isotopes and elements, making it difficult to predict which species will act as nucleation centers and under what conditions they will stabilize.

Additionally, the timescales on which nucleation occurs are typically on the order of picoseconds to nanoseconds [68], whereas this thesis focuses on the subsequent aggregation and sedimentation behavior that occurs on much larger temporal and spatial scales. For these reasons, the nucleation stage is omitted from the simulations. Nayak et al. [53] have performed a nucleation study on the formation of Nickel clusters. The study revealed that clusters up to 23 atoms slowly converged to bulk structures and properties with high alternating stability. Highlighting the difficulty of predicting and simulating small cluster stability. In conclusion, due to increased complexity and difference in spatial and time scales, nucleation is not included in the scope of this research.

Appendix B further elaborates the nucleation process, the critical radius based on surface-to-volume minimalisation and the reduction of the Gibbs free energy barrier by taking partial pressures into account.

Preliminary Study on Aggregation Behaviour

To identify which physical interactions promote colloidal aggregation, a parameter study was performed in which key parameters, such as temperature, particle radius, Hamaker constant and ionic strength, were systematically varied. The results, together with the parameter ranges and resulting interaction potentials, are presented in Appendix C.

The study successfully revealed how individual parameters influence both the shape of the DLVO potential. Clear trends were observed: certain parameters directly modified the attractive or repulsive contributions of the potential, while others primarily affected its overall magnitude. However, combining the effects of multiple parameters proved challenging. It was observed that different combinations of physical parameters could yield nearly identical potential profiles, suggesting the presence of underlying scaling relationships. Additionally, the analysis highlighted that several input quantities, particularly the Hamaker constant and the surface potential, remain uncertain or difficult to determine experimentally.

The combination of parameter uncertainty and the emerging evidence of scaling behaviour provided strong motivation to develop a non-dimensional framework that captures colloidal aggregation behaviour in a more general and physically interpretable form. Previous studies have investigated how individual parameters affect colloidal interactions [17], yet a comprehensive dimensionless formulation that summarise these effects has not been established.

This thesis therefore introduces the first development of such a non-dimensional DLVO-based framework. The framework enables comparison across different systems by expressing the relevant physics (Van der Waals attraction and electrostatic repulsion) through dimensionless ratios rather than system-specific quantities, thereby improving both generality and predictive capability.

2.4. Existing Literature

Relevant prior research is summarised below and is used as a foundation of this report.

Metal NPs in Ionic liquids

- This work demonstrates how the introduction of specific ligands stabilises gold nanoparticles (Au NPs) dispersed in ionic liquids, thereby suppressing the tendency to aggregate. Siqueira and Ribeiro [65] show that ligand-coated Au NPs in ionic liquids maintain dispersion stability, highlighting the key role of surface functionalisation in controlling aggregation thermodynamics.
- In their work, He and Alexandridis [26] examine AU NPs dispersions in ionic liquids with added ligands, showing that specific surface functionalisation can successfully stabilise the nanoparticles and markedly suppress aggregation. They report that classic DLVO theory fails to capture the observed stabilisation behaviour.
- Ravichandran and al. [59] uses a hybrid approach combining all-atom (AA) and coarse-grained (CG) molecular dynamics to investigate the dispersion of silver (Ag) nanoparticles in an imidazolium-based ionic liquid. The authors find that cation rings and specific anion headgroups preferentially adsorb onto the NP surface, forming solvation layers that influence stability.

Non-DLVO Forces

- In their study of silica NP dispersions, Liu et al. [48] demonstrate that divalent cations Ca^{2+}, Mg^{2+} have different critical aggregation concentrations while having the same valency. These results can not be fully explained by the classical DLVO model and instead suggest additional ion-bridging and hydration-force contributions to aggregation kinetics.
- In their study, Merk et al. [51] investigate ligand-free AU NPs in dilute electrolyte solutions and demonstrate that anion identity following the Hofmeister sequence strongly influences colloidal stability, even at low ionic strength. They show that traditional DLVO theory cannot account for these ion-specific stabilization trends and provide experimental evidence that more polarizable, chaotropic anions reduce aggregation rates by adsorbing at the gold surface.

Coarse-Grained Molecular Dynamics

- Petretto, Campomanes, and Vanni (2023) developed a coarse-grained molecular dynamics model compatible with the SPICA/SDK force field to simulate the aggregation of surface-functionalized AuNPs in aqueous solution. The model introduces a new "core-decoy" bead to better capture gold–ligand and gold–solvent interactions, enabling accurate reproduction of dimerization energies and aggregation kinetics across hydrophobic and charged NP systems. This approach bridges atomistic and coarse-grained modeling, offering improved computational efficiency without sacrificing essential molecular accuracy.[58]
- This study proposes an application of Nosé–Hoover (NH) dynamics as a coarse-graining (CG) method for molecular simulations, offering an alternative to traditional Langevin-based approaches. The NH dynamics, known for its deterministic temperature control without stochastic forces, is adapted here to model a monoatomic Lennard-Jones system at different coarse-grained levels. The CG particle's equation of motion is derived from atomic-level dynamics, linking NH thermostat terms with system properties obtained from molecular dynamics (MD) simulations. [83]
- Siqueira and Ribeiro [64] examines two Au NPs immersed in a variety of imidazolium-based ionic liquids, computing potentials of mean force (PMF) and examining ion layering between NPs. It finds that longer alkyl-chain cations lead to a thicker apolar spacer between particles, increasing stability (i.e., resisting aggregation).

2.5. Motivation and Research Objectives

The background study shows that the aggregation of NPs in ionic liquids has been widely studied in literature, particularly for systems involving noble metals such as gold. These studies have provided valuable insight into the mechanisms governing NP aggregation and the influence of various physical parameters. However, a clear, unified framework that relates these mechanisms across different systems remains lacking. Most existing studies investigate single-parameter variations and qualitatively compare the results to DLVO theory, often concluding that DLVO either underestimates or overestimates experimental aggregation behaviour.

This thesis forms part of a broader PhD project by N. Mischenko, which aims to describe the complete lifecycle of solid fission products (SFPs) in molten salt reactors (MSRs). Within that context, this work serves as an essential stepping stone toward a quantitative framework capable of describing NP growth within MSR environments. The ultimate goal is to extend this understanding to particle–wall interactions and to predict the sedimentation behaviour of NPs on reactor walls.

Research Questions

This thesis focuses on the development of a non-dimensional framework that captures the aggregation behaviour of colloidal systems through dimensionless parameters derived from DLVO theory. This framework aims to reduce the number of parameters to a minimal set that effectively represents the behaviour of these systems. Additionally, it is applied to coarse-grained simulations to quantify aggregation kinetics under varying physical conditions. Molten salt reactors serve as a relevant case study due to the presence of SFP NPs.

Accordingly, the following research questions are formulated:

- To what extent can a DLVO-based, non-dimensional framework describe and classify nanoparticle aggregation behaviour of a system?
- How do the dimensionless parameters of this DLVO framework relate to aggregation kinetics, specifically the aggregation rate and the equilibrium cluster size, with coarse-grained molecular dynamics?
- How can this non-dimensional DLVO framework be applied to predict the aggregation of solid fission products in molten salt reactor conditions?

The following chapters address these research questions in detail.

Part I

Theoretical Framework Development

3

Interaction Potentials and Colloidal Theory

This chapter introduces the theoretical background of DLVO theory. The interaction potentials that constitute the total potential are presented, together with the underlying physical assumptions, so that the resulting applications and limitations are well understood. In addition, specific considerations related to the Molten Salt Reactor (MSR) case are discussed. Section 3.1 introduces the concept of the electric double layer, which arises in ionic systems due to charge separation near surfaces. This phenomenon forms the basis for the electrostatic repulsion term in the total potential. Section 3.2 discusses DLVO theory in deeper detail, and describes the fundamental components that constitute the potential, namely electrostatic repulsion, van der Waals attraction, and short-range Born repulsion. These potentials are subsequently formulated for both sphere-sphere and sphere-plate geometries. Finally, Section 3.3 presents the complete DLVO potential that combines the different contributions and will later be implemented in the molecular dynamics simulations.

3.1. Electric Double Layer

The Electric Double Layer (EDL) is a phenomenon that appears on the surface of a conductive object when it is exposed to a fluid. The EDL refers to the two parallel layers of charge surrounding the object. The first layer, the surface charge (either positive or negative), consists of ions adsorbed onto the object through chemical interactions or free electrons that are on the surface. The second layer is composed of ions attracted to the surface charge via the Coulomb force, electrically screening the first layer. The second layer consists of free ions that are less strongly bound to the particle surface. These ions remain in the surrounding fluid and move due to electrostatic attraction and thermal motion. This region is commonly referred to as the diffuse layer. Figure 3.1 shows the structure of the electric double layer surrounding a negatively charged colloidal particle. A compact Stern layer of adsorbed counter-ions forms directly at the particle surface. Followed by the diffuse layer, which extends into the solution, where ion concentrations follow the Boltzmann distribution until the bulk concentration is reached.

In MSRs, conductive surfaces in contact with the molten salt develop a surface potential and carry a net surface charge. This originates from the mobility of conduction electrons, which repel each other electrostatically and migrate toward the material boundary. In addition, electron spill-out occurs, depending on the surrounding medium, the electronic charge density extends partially beyond the solid surface [42]. This creates a local charge imbalance and an electrostatic potential difference. The resulting negative potential attracts cations (positively charged ions) from the salt, which accumulate near the surface, forming the first layer of the EDL, the *Stern layer*.

When the surface potential is sufficiently large (typically > 25 mV), these cations become strongly bound to the surface, forming a relatively immobile *Stern layer* [81]. Beyond this, the potential decays gradually into the molten salt, and ions rearrange according to the residual potential, creating the second layer of the EDL: the *Diffuse layer*. In this region, the concentration of counter-ions (in the case of a MSR: cations) remains higher than that of anions until the potential decays to zero, effectively screening the potential. This screening effect continues until the concentrations of the cations and anions reach the bulk value.

The next section will explain the effect of screening in more detail.

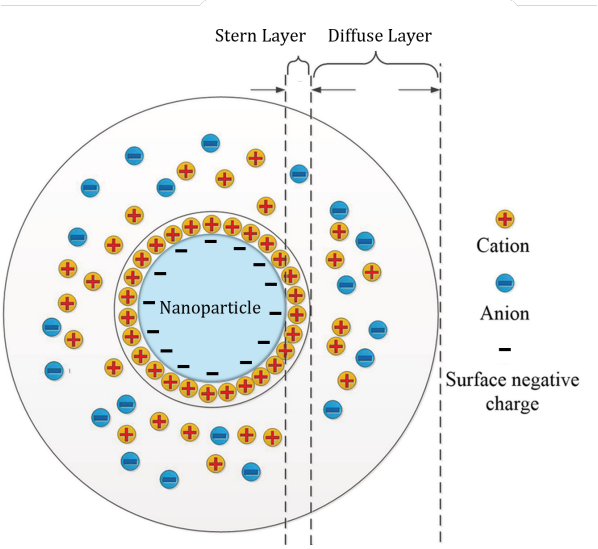

Figure 3.1: A schematic representation of the EDL around a charged NP. The EDL consists of the compact Stern layer, where counter-ions are adsorbed directly onto the surface, and the diffuse layer, where the remaining ions are distributed according to the electrostatic potential.

Screening Effect

The EDL gives rise to a screening effect that effectively reduces the electrostatic potential near a charged surface. This occurs because counter-ions are attracted toward negatively charged particles, where they partially neutralize the surface charge. Each cation generates an electric potential of opposite sign relative to that of the surface, and the superposition of these potentials results in a net reduction of the overall potential. The stronger the screening effect, the shorter the double-layer thickness.

Figure 3.2a and Figure 3.2b illustrate how ionic strength affects the thickness of the electric double layer surrounding a negatively charged surface. In a high ionic strength environment (Figure 3.2a), counter-ion availability is high, lowering the electric potential φ and reducing the Debye length. In contrast, at low ionic strength (Figure 3.2b), fewer ions are available to screen the surface charge, resulting in a more gradual potential decay and a larger Debye length. The Debye lengths shown are indicative and not drawn to scale, and are intended solely to highlight the trend in screening behavior.

In summary, the electrical double layer near a conductive interface consists of a surface layer of excess electrons, possibly a layer of specifically adsorbed counter-ions, and a diffuse region in which one type of ion is present in excess while the other is depleted. Together, these regions screen the interfacial charge and determine the local electrostatic potential profile. In the next section, the Poisson-Boltzmann equation will be shown as well as the derivation of the inverse Debye length κ. The Poisson–Boltzmann equation is essential for describing how the electrostatic potential decays from the charged surface into the bulk. The Poisson-Boltzmann and its simplified form (Debye-Hückel approximation) form the basis of formulating the electric repulsion between colloidal particles.

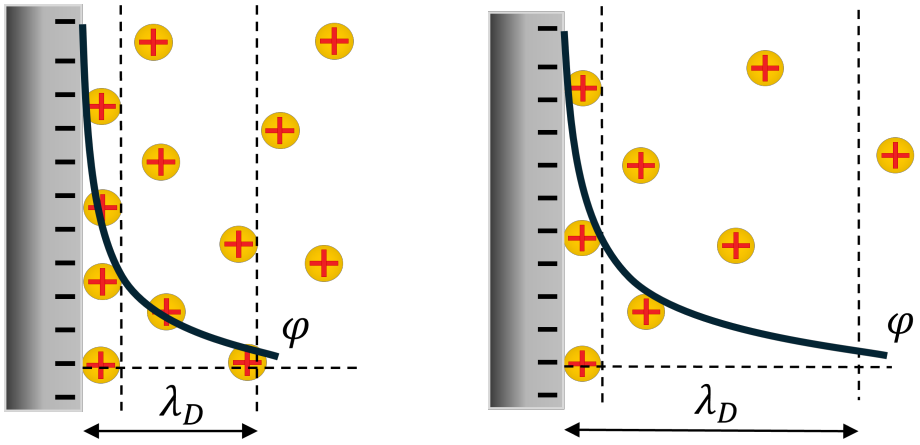

(a) High ionic strength (short Debye length).

(b) Low ionic strength (long Debye length).

Figure 3.2: Effect of ionic strength on the electric double layer surrounding a negatively charged surface. (a) At high ionic strength, counter-ions efficiently screen the surface charge, reducing the electric potential φ and shortening the Debye length. (b) At low ionic strength, fewer counter-ions are available, resulting in a larger Debye length and a more gradual decay of φ.

Poisson-Boltzmann Equation

This section outlines the key steps involved in deriving the (linearized) Poisson–Boltzmann equation. The complete derivation is provided in Appendix A.

The Poisson–Boltzmann equation was formulated independently by Gouy and Chapman [22, 8], who combined Poisson's equation from electrostatics with the Boltzmann distribution for ionic charge densities. If the surface potential φ_0 is known, the electric potential and ion distribution in the electrolyte can be described as a function of distance from the surface.

In deriving their model, Gouy and Chapman made the following key assumptions:

1. The surface is planar, infinitely large, and of infinite thickness.
2. The anions and cations in the medium are treated as point charges that can approach the surface arbitrarily closely.
3. The surface charge density and potential are uniform over the entire surface.
4. The solvent acts as a continuous medium with constant dielectric properties, independent of the distance from the surface.

Using the electrostatic relation that the electric field is the gradient of the scalar potential, $\mathbf{E} = -\nabla\varphi$, the electric field can be expressed in terms of the potential. Combining this with one of Maxwell's equations, $\nabla \cdot \mathbf{E} = \rho/\varepsilon_0$, results in Poisson's equation. Poisson's equation directly relates the charge density to the electrostatic potential [24].

$$\nabla^2\varphi(\mathbf{r}) = -\frac{\rho(\mathbf{r})}{\varepsilon}, \tag{3.1}$$

where ε is the permittivity of the medium, defined as $\varepsilon = \varepsilon_0\varepsilon_r$. Here, ε_0 denotes the vacuum permittivity, ε_r the relative dielectric constant of the medium, and $\rho(\mathbf{r})$ the local charge density.

In the case of an ionic liquid, the ions redistribute themselves according to the local electrostatic potential. Since they are treated as point charges, their spatial arrangement is not restricted by their finite size and they can fully respond to the potential field. By considering the total free energy, which includes both chemical and electrostatic contributions, the ionic concentration profiles can be derived to follow a Boltzmann distribution. From these distributions of cations and anions, the charge density can be expressed and substituted into Eq. 3.1, resulting in the Poisson–Boltzmann equation [15]:

$$\nabla^2\Phi(\mathbf{r}) = \kappa^2 \sinh\big[\Phi(\mathbf{r})\big] + \frac{\rho_{\text{ext}}(\mathbf{r})}{\varepsilon}. \tag{3.2}$$

Here, the dimensionless potential $\Phi = \dfrac{ze\varphi}{k_B T}$ is introduced, where z is the ionic valence, e the elementary charge, κ is the inverse Debye length, k_B the Boltzmann constant, and T the absolute temperature. The system can be solved using the following boundary conditions:

$$\Phi = \Phi_0 \left(= \frac{ze\varphi_0}{k_B T} \right) \quad \text{for } r = 0, \qquad \Phi = 0 \text{ and } \frac{d\Phi}{dr} = 0 \text{ for } r \to \infty, \tag{3.3}$$

which impose that at the surface, the potential equals the surface potential φ_0, and that it decays to zero far from the charged interface. Moreover, the inverse Debye length κ is defined as

$$\kappa^2 = \frac{2e^2 N_A I}{\varepsilon k_B T}, \tag{3.4}$$

with N_A is Avogadro's constant and I the ionic strength of the solution, expressed as [66]:

$$I = \frac{1}{2} \sum_i z_i^2 c_i, \tag{3.5}$$

where z_i is the ionic valence and c_i the molar concentration [mol L^{-1}] of ion species i. There exists ambiguity around the ionic strength, as sources have defined it with concentration in units of molality [mol kg^{-1}]. These two definitions yield different results. For this reason, it is explicitly mentioned here. The ionic strength I strongly influences the value of κ and thus the extent of electrostatic screening. Systems containing multivalent ions exhibit particularly high ionic strengths, resulting in significantly shorter screening lengths and stronger double-layer compression.

Linearized Poisson-Boltzmann equation

A useful approximation can be made for low surface potentials $\Phi_o < 1$ or when $\varphi_o < 25$ mV. Assuming $\sinh(\Phi) \approx \Phi$ transforms the equation in the Debye-Hückel approximation:

$$\nabla^2 \Phi(\mathbf{r}) = \kappa^2 \Phi(\mathbf{r}) + \frac{\rho_{\mathrm{ext}}(\mathbf{r})}{\varepsilon}. \tag{3.6}$$

Solving equation 3.6 for a point charge: $Q\delta^3(r)$ in spherical coordinates and under the boundary conditions given in equation (3.3) recovers the Yukawa potential [88]:

$$\Phi(r) = \frac{Q}{4\pi\varepsilon r}\, e^{-\kappa r}, \quad r = |\mathbf{r}|, \tag{3.7}$$

The Debye-Hückel approximation is the basis of the Linear Superposition Approximation (LSA). This approximation will capture the electric interaction of charged spheres in ionic liquids.

Electric Double Layer Behavior in Molten Salts

In molten salts, the behaviour of the EDL differs fundamentally from that in dilute aqueous electrolytes. Due to the extremely high ionic concentration, electrostatic screening is very strong and the double layer becomes exceedingly thin, typically smaller than the ionic diameter. Consequently, the potential decays within a very short distance from the metallic surface, and the classical concept of a continuous diffuse layer becomes less meaningful. Instead, ion–ion correlations and specific adsorption effects dominate the interfacial structure, leading to partial ordering or layering of the first ionic layers near the surface.

Because of the high ionic strength and finite ion size, assumption 2 of Gouy and Chapman becomes questionable. Charged species cannot follow the ideal Boltzmann distribution without overlap or crowding. In other words, steric effects and strong screening limit the applicability of the continuum diffuse-layer concept. The Gouy–Chapman theory therefore breaks down under such extreme conditions, particularly when screening is strong and the dielectric constant is low. At sufficiently high surface charge densities, alternating layers of cations and anions may form near the interface [82]. Additionally, the assumption of a 'smeared-out' surface charge may seem

especially suspect in view of the small sized NPs where structural properties are still relevant [53]. However, the rate of exchange of protons and other ions between surface sites and the adjacent solution is usually very rapid, compared to the time of approach of colloidal particles. For this reason, many surfaces may be regarded as having an effectively uniform surface charge density [15]. The last assumption is valid for the bulk of the liquid where temperature is constant. However, near reactor walls or at heat exchangers, there exists a temperature gradient and the effect on the dielectric properties may becomes significant.

Nevertheless, both experimental observations and molecular simulations suggest that the general EDL framework remains a useful approximation to describe interfacial electrostatics, provided that the surface potential is sufficiently low [39]. Even when the assumptions of dilute-electrolyte theory are not strictly valid, the linearized form of the Gouy–Chapman model can still capture the essential screening behavior.

The assumption of low surface potentials is appropriate for the conditions encountered in a MSR. Inside the reactor, no external potential is applied to the metallic walls or to suspended particles, so the resulting surface potentials are expected to be small enough for the linearized Gouy–Chapman approximation to hold [39].

The EDL thus governs one of the key interaction potentials forming the basis of DLVO theory. The DLVO theory and the corresponding potentials are discussed in the following section.

3.2. DLVO Theory and Interatomic Forces

The theory developed by Derjaguin, Landau, Verwey and Overbeek (DLVO), describes the balance between attractive and repulsive forces in colloidal systems [11, 76]. This section introduces and explains each of the interaction potentials that together constitute the DLVO theory. These are discussed in the following order: electric repulsion, van der Waals attraction and Born repulsion potential.

3.2.1. Electrostatic Repulsion

According to DLVO theory, and as predicted by the Gouy–Chapman model, the electrostatic repulsion originates from the overlap of the electric double layers surrounding adjacent charged particles. When these diffuse layers overlap, the local ion concentration between the surfaces increases, leading to a repulsive force. This phenomenon is represented in Figure 3.3. The strength of this electrostatic repulsion depends on both the surface potential and the characteristic thickness of the double layer. A higher surface potential enhances the repulsive force, while a lower ionic concentration increases the double-layer thickness, extending the range of the interaction.

Boundary Conditions

Extensive research has been conducted on the interaction between charged planar surfaces and between charged spheres [42, 15]. The analytical solution of the linearized Poisson–Boltzmann equation strongly depends on the applied boundary conditions. Two limiting cases are commonly distinguished: the *Constant-Potential Approximation (CPA)* and the *Constant-Charge Approximation (CCA)*. These boundary conditions will be briefly discussed in this section. They are summarized in Table 3.1.

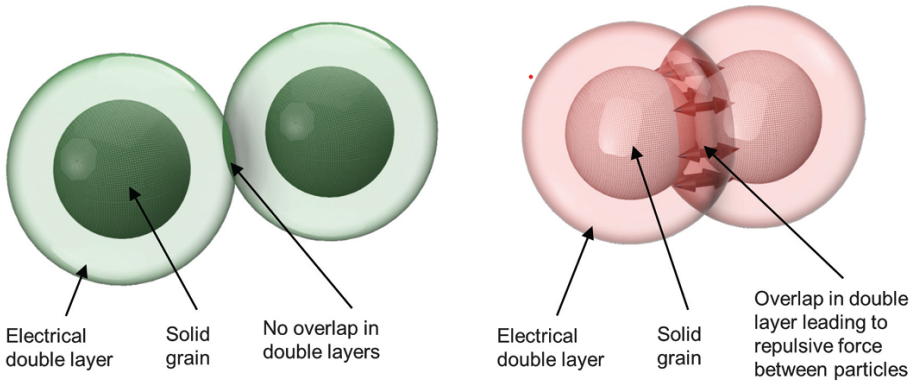

Figure 3.3: Schematic representation of electrical double layers surrounding charged particles. When the double layers do not overlap (left), no electrostatic interaction occurs. When the layers overlap (right), repulsive forces arise between the particles due to increased ion concentration in the overlapping region [50].

Table 3.1: Boundary conditions for CPA and CCA.

Constant-Potential Approximation (CPA)	**Constant-Charge Approximation (CCA)**
$\varphi_{\text{surface}} = \text{constant}$	$\sigma_{\text{surface}} = \text{constant}$
$\varphi(h=0) = \varphi_1$	$-\varepsilon \left.\dfrac{d\varphi}{dh}\right\vert_{h=0} = \sigma_1$
$\varphi(h=D) = \varphi_2$	$+\varepsilon \left.\dfrac{d\varphi}{dh}\right\vert_{h=D} = \sigma_2$

There, the sign difference in the CCA condition arises because the outward normal vector at $h = D$ points in the opposite direction of that at $h = 0$.

The *Constant-Potential Approximation (CPA)* applies to systems where charge exchange between the surface and the surrounding medium is rapid, such as metallic or highly conductive interfaces. Under this condition, the surface potential remains constant even when the double layers overlap, since the surface charge can be instantly adjust to maintain electrochemical equilibrium. Interestingly, this condition can lead to weakly *attractive* interactions between like-charged surfaces at small separations, as the potential gradient decreases locally due to charge redistribution.

In contrast, the *Constant-Charge Approximation (CCA)* describes systems where surface charge originates from fixed ionized groups that cannot quickly re-equilibrate, such as oxide or polymer surfaces. In this case, the total surface charge remains constant while the potential varies with separation. As two surfaces approach, their double layers are compressed, resulting in a steep, exponentially increasing repulsive force that diverges at short distances.

Linear Superposition Approximation

In the context of metallic cluster aggregation in MSRs, the CPA is generally not applicable. The brief duration of interactions between colloidal particles does not allow sufficient time for the electrochemical potential to re-equilibrate [20]. Experimental and theoretical studies indicate that the interaction behavior typically lies between the two extremes of CPA and CCA [13]. This intermediate regime is well described by the Linear Superposition Approximation (LSA), which assumes that the potentials of interacting particles are sufficiently small and can be linearly superimposed without significant mutual distortion. Despite its simplicity, the LSA provides an accurate description of electrostatic interactions in systems with moderate surface potentials.

$$\varphi_t = \varphi_1 + \varphi_2, \tag{3.8}$$

where the total potential φ_t is the sum of the potential of one particle φ_1 and of the other φ_2.

LSA Sphere-sphere potential

The LSA potential is first derived for the case of two parallel plates approaching each other. To extend this to spherical geometries, the Derjaguin approximation is applied, relating the interaction between curved surfaces to that between planar ones. The detailed derivations are omitted here, and only the final expression for the LSA potential between two spheres is presented in this thesis [54, 23].

$$U^{ss}_{\text{LSA}}(h) = 128\pi \frac{a_1 a_2}{(a_1 + a_2)} \frac{N_A I k_B T}{\kappa^2} \, \gamma_1 \gamma_2 \, e^{-\kappa h} \qquad h \ll a \tag{3.9}$$

where γ_1, γ_2 represent the dimensionless surface potentials of particle 1 and 2:

$$\gamma = \frac{\exp(\Phi_0/2) - 1}{\exp(\Phi_0/2) + 1} = \tanh\left(\frac{\Phi_0}{4}\right) \tag{3.10}$$

Research has shown that the LSA has very good agreement if the separation of the particles is much larger than the debye length $\kappa h \gg 1$ [56, 71].

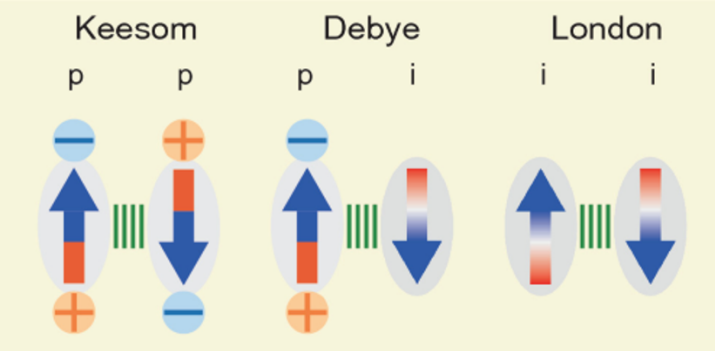

Figure 3.4: Overview of the three dipole-dipole interactions. p denotes a permanent dipole moment and i an induced dipole moment. The interactions are arranged from strongest (left) to weakest (right) [84].

LSA Sphere-plate potential

The sphere plate potential can be obtained by allowing one of the radii to approach infinity. Taking the limit $a_2 \to \infty$ and generalizing a_1 to any radius a gives the sphere-plate potential:

$$U_{\mathrm{LSA}}^{sp}(h) = 128\pi \frac{N_A I k_B T}{\kappa^2}\, a\, \gamma_1 \gamma_2\, e^{-\kappa h} \qquad h \ll a \tag{3.11}$$

3.2.2. Van der Waals Attraction

This section covers the van der Waals attraction potential, which is one of the three potentials of DLVO theory. At the end of the section, the sphere-sphere and the sphere-plate van der Waals attraction potentials are given.

It has long been recognized that a natural attractive force exists between neutral molecules. These intermolecular attractions, collectively known as *van der Waals forces*, arise from interactions between electric dipoles, both permanent and induced. Even in systems without a net charge, transient or asymmetric charge distributions within atoms and molecules produce weak but significant electrostatic attractions that determine colloidal stability.

Three types of dipole-dipole interactions are generally distinguished, all of which are wrapped under the van der Waals force. From strongest to weakest, these are the *Keesom*, *Debye*, and *London interactions*, the interaction are shown in Figure 3.4.

- The *Keesom interaction* describes the electrostatic attraction between molecules possessing permanent dipole moments. As the strongest of the three dipole-dipole interactions, these dipoles orient themselves so that opposite charges align, thereby minimizing the total electrostatic energy. The strength of this interaction decays with the sixth power of the separation distance, r^{-6}, indicating a relatively short range compared to ionic interactions [2].
- The *Debye interaction* occurs between a polar molecule and a non-polar molecule. The electric field of the permanent dipole induces a transient dipole moment in the otherwise neutral species, creating an attractive force between them. This interaction also decays proportionally to r^{-6}.
- Finally, the *London dispersion interaction* acts even between entirely non-polar molecules. Fluctuations in the electron density create instantaneous dipoles that induce complementary dipoles in neighboring atoms or molecules. The resulting attraction, though individually weak, is universal and becomes significant at short separations. Like the Keesom and Debye interactions, it decays proportional to r^{-6}.

Together, these three mechanisms give rise to the van der Waals potential, which for a pair of molecules can be expressed as

$$U_{\mathrm{vdW}}(h) = -\frac{C}{r^6}, \tag{3.12}$$

where C is a material-specific constant representing the strength of the interaction and capturing the Keesom, Debye and London interactions.

When dealing with macroscopic systems, such as colloidal particles or solid surfaces, the total van der Waals interaction results from the cumulative effect of many individual atom-atom interactions. Integrating these interactions over the volume of the respective bodies yields analytical expressions that depend on the geometry. For

instance, the interaction between a molecule and an infinitely extended planar surface can be derived as follows. The separation between a molecule and a surface element is given by $h = \sqrt{x^2 + y^2 + z^2}$, while the differential volume element is $dV = dx\,dy\,dz$. The total potential energy is obtained by integrating the pairwise interaction over the entire half-space:

$$U_{\mathrm{vdW}}(r) = -\rho \int_{-\infty}^{\infty}\int_{-\infty}^{\infty}\int_{-\infty}^{\infty} \frac{C}{\left(x^2+y^2+z^2\right)^3}\,dx\,dy\,dz = -\frac{\pi\rho C}{6r^3}, \tag{3.13}$$

where ρ is the molecular number density. The interaction between a particle and a wall thus decays as r^{-3}, showing that it is longer-ranged than the interatomic dependence r^{-6}.

Extending this approach to two planar surfaces yields an interaction per unit area that scales as r^{-2}:

$$U_{\mathrm{vdW}}(r) = -\frac{A_{12}}{12\pi r^2}, \tag{3.14}$$

where $A_{12} = \pi^2\rho_1\rho_2 C$ is the Hamaker constant, capturing the strength of interaction between two media (1 and 2) across a vacuum [25]. Typical values of A range between 10^{-21} and 10^{-17} J, depending on the materials involved. The Hamaker constant effectively separates the material-dependent and geometric contributions, simplifying the analysis of macroscopic van der Waals interactions.

Sphere-Sphere Attraction Potential

Hamaker also derived the van der Waals interaction between two spheres, which is particularly relevant when describing colloidal particles [25]:

$$U^{ss}_{\mathrm{vdW}} = -\frac{A}{6}\left[\frac{2a_1a_2}{h^2+2a_1h+2a_2h} + \frac{2a_1a_2}{h^2+2a_1h+2a_2h+4a_1a_2} + \ln\left(\frac{h^2+2a_1h+2a_2h}{h^2+2a_1h+2a_2h+4a_1a_2}\right)\right], \tag{3.15}$$

where h is the interatomic distance between the clusters. In the near-field limit, where $h \ll a_1, a_2$, equation (3.15) simplifies to

$$U^{ss}_{\mathrm{vdW}} = -\frac{Aa_1a_2}{6h(a_1+a_2)}, \qquad h \ll a_1, a_2. \tag{3.16}$$

These expressions are most accurate at short separations (up to about 10% of the particle radius), where van der Waals interactions dominate [15].

Sphere-Plate Attraction Potential

Finally, the sphere-plate interaction can be derived as a limiting case of the sphere-sphere interaction by allowing one of the radii to approach infinity ($a_2 \to \infty$) [25]:

$$U^{sp}_{\mathrm{vdW}} = -\frac{A}{6}\left[\frac{a}{h} + \frac{a}{h+2a} + \ln\left(\frac{h}{h+2a}\right)\right], \tag{3.17}$$

where there is only one particle radius in the equation, so the subscript is removed $a_1 \to a$, This configuration is of particular relevance for describing particle deposition on surfaces and represents the attractive contribution to the DLVO potential.

3.2.3. Born Repulsion Potential

Lastly, the third potential of the DLVO theory is discussed, the Born potential. At the end of the section, both the sphere-sphere and the sphere-plate potentials are given used in this research.

At very short separations, all particles experience a repulsive force that prohibits the nuclei from coming in closer contact with each other. This repulsive force originates from the Pauli exclusion principle when there is overlap of electron clouds from both atoms. These forces are important in determining the atomic spacing in solids, liquids, and gasses and can dominate when molecules are separated by distances of a few Ångström, which can occur at high pressures.

Intermolecular forces are essential in molecular dynamics. In order to simulate atomic motion and predict system behavior, the model must include a realistic repulsive force that prevents nuclei from collapsing into one another. This short-range repulsion is typically represented using an exponential potential,

$$U_{\mathrm{Born}}(h) = A\, e^{-Bh}, \tag{3.18}$$

known as the Born-Mayer potential [6], or alternatively approximated by a power-law form,

$$U_{\mathrm{LJ,rep}}(h) = \frac{A}{h^{12}}, \tag{3.19}$$

as used in the Lennard-Jones potential [44]. Both expressions are empirical representations of the short-range Pauli repulsion. Feke *et al.* (1984) derived the Born potential from the classical Lennard-Jones m-n potential

$$U_{LJ}(r) = \varepsilon \frac{n}{n-m} \left(\frac{n}{m}\right)^{\frac{m}{n-m}} \left[\left(\frac{\sigma}{r}\right)^{m} - \left(\frac{\sigma}{r}\right)^{n}\right] \tag{3.20}$$

with parameters m, n that tune the repulsive part and attractive part of the potential respectively. Setting $m = 12$ and $n = 6$ the classical Lennard-Jones potential is retrieved.

$$U_{LJ}(r) = 4\varepsilon \left[\left(\frac{\sigma}{r}\right)^{12} - \left(\frac{\sigma}{r}\right)^{6}\right] \tag{3.21}$$

Researches have shown to be in good congruence about the attractive part being $n = 6$. However, many researches have been in disagreement about the parameter m that controls the repulsive part of the potential. The Lennard-Jones potential is a rigid potential and sphere-symmetric. Resulting in simulating the atoms as hard-spheres that are isotropic. While in reality, electron-clouds deform when atoms come closer together. Making the real potential several times softer, decreasing the exponential $m < 12$, than is captured in setting classical Lennard-Jones potential $m = 12$

Sphere-Sphere Born Repulsion Potential
A more realistic, and softer, potential for two colloidal particles can be obtained by integrating the repulsive part of the Lennard-Jones potential over the volume of the two clusters. All the individual contributions of the atoms are captured, not regarding the specific internal structure and atom positions of the cluster. Feke *et al.* (1984) evaluated the integral for two clusters that resulted in [17, 12].

$$\begin{aligned} U_B^{ss}(r) = {} & 4A\,\sigma^{n-6} \frac{(n-8)!}{(n-2)!}\, \frac{1}{r} \\ & \left[\frac{r^2 - 7r(a_1+a_2) + 6(a_1^2 + 7a_1a_2 + a_2^2)}{(r-a_1-a_2)^7}\right. \\ & + \frac{r^2 + 7r(a_1+a_2) + 6(a_1^2 + 7a_1a_2 + a_2^2)}{(r+a_1+a_2)^7} \\ & - \frac{r^2 + 7r(a_1-a_2) + 6(a_1^2 - 7a_1a_2 + a_2^2)}{(r+a_1-a_2)^7} \\ & \left. - \frac{r^2 - 7r(a_1-a_2) + 6(a_1^2 - 7a_1a_2 + a_2^2)}{(r-a_1+a_2)^7}\right] \end{aligned} \tag{3.22}$$

where r is the distance between the two centers of the particle. Equation (3.22) is valid for $n \geq 8$ [17]. In addition, σ is the collision diameter and is atom specific. The collision diameter controls the lateral position of the potential and is in most cases a few Angstrom $\dot{A}$. So the collision diameters of Mo and Nb are respectively $\sigma_{Mo} = 0.31$ nm and $\sigma_{Nb} = 0.28$ nm. [49].

Feke et al. [17] has conducted a near field approximation for equation (3.22) as well.

$$U_B^{ss,nf}(h) = 4A\sigma^{n-6} \frac{(n-6)!}{(n-2)!} \frac{a_1 a_2}{a_1 + a_2} \frac{1}{h^{n-5}}, \qquad h \ll a_1, a_2. \tag{3.23}$$

where the distance parameter has changed from the centers of the two colloidal particles r to the distance between the surfaces h. Moreover, it should be noticed that the near-field potential is five powers lower than the original exponent of the Lennard-Jones potential $m = 12$, displayed in Equation (3.21). The reduced repulsive power more accurately represents the deformation of electron cloud densities as two clusters approach each other.

Sphere-Plate Born Repulsion Potential
A sphere-plate potential can be derived by taking the limit of one particle radius that goes to infinity $a_2 \to \infty$ from equation (3.22) by Ruckenstein and Prieve [61]

$$U_B^{sp} = \frac{A\sigma^6}{7560}\left[\frac{8a+h}{(2a+h)^7} + \frac{6a-h}{h^7}\right]. \tag{3.24}$$

Equations (3.22) and (3.23) are a more realistic short-range repulsion potential for macroscopic bodies than the simple Lennard-Jones form. In combination with an attractive potential for the van der Waals Force and a repulsive electrostatic potential, the DLVO potential is completed.

3.2.4. Non-DLVO Forces

DLVO theory has long served as a cornerstone for describing the aggregation behavior of colloidal systems. However, numerous experimental studies have shown that the DLVO framework systematically under- or overestimates aggregation rates in certain systems. These deviations arise from additional interactions not accounted for by the classical theory, collectively referred to as *non-DLVO forces*. The most relevant categories of these forces are:

1. Hydration forces,
2. Hydrophobic forces,
3. Ion polarizability and Hofmeister effect,
4. Steric stabilization.

This section briefly discusses the general effect of each of these forces and highlights their relevance in the context of molten salt systems [15].

Hydration Forces
When two particles possessing hydrated surfaces approach one another, their interaction is subject to an additional short-range *hydration repulsion*, distinct from the electrostatic double-layer repulsion [57]. This repulsive force originates from the energetic cost associated with removing the bound or structured water molecules from the surface if direct contact is to occur.

Water molecules, possessing a finite dipole moment, tend to align with the local electric field near charged surfaces, forming one or more structured hydration layers. These ordered layers lower the free energy of the system and provide mechanical stability to the interface. As two hydrated surfaces approach, their hydration shells begin to overlap, similar to the overlap of electric double layers. To achieve closer separation, the structured water must be displaced, which requires additional work and therefore increases the free energy of the system. This process manifests macroscopically as a short-range repulsive force that typically acts over distances of 1–3 nm.

Hydrophobic Interactions
In contrast to hydration repulsion, hydrophobic surfaces experience an additional attractive interaction that promotes aggregation [34, 10]. Water possesses a highly structured hydrogen-bonding network. The presence of a hydrophobic surface disrupts this structure, as it prevents hydrogen bonds from forming in its immediate vicinity. When two hydrophobic surfaces approach, the confined water between them becomes increasingly disordered and energetically unfavorable.

To minimize free energy, water molecules are expelled from the confined region into the bulk, where they can form unrestricted hydrogen bonds. The resulting gain in entropy and reduction in interfacial energy give rise to an attractive hydrophobic force. This interaction can significantly exceed the strength of van der Waals attraction, particularly for strongly hydrophobic surfaces or in systems containing dissolved gases, where nanobubble bridging may further enhance the attraction.

The hydrophobic tendency of a surface is commonly characterized by the contact angle (θ) of a liquid droplet on the surface. It provides a macroscopic measure of surface wettability:

- $\theta < 90°$: hydrophilic surface, high wettability, water spreads easily.
- $\theta > 90°$: hydrophobic surface, low wettability, water beads up.

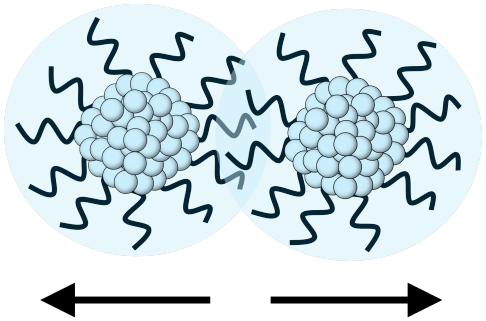

Figure 3.5: A schematic representation of steric stabilization, showing two particles coated with polymers or ligands (black lines). The overlap of these layers during close approach generates a repulsive force that prevents aggregation.

Thus, the contact angle serves as a practical indicator of the surface's interaction with water and correlates directly with the magnitude of hydrophobic forces observed experimentally.

Ion polarizability and Hofmeister effect

In addition to the general electrostatic description provided by the Gouy-Chapman-Stern framework, the stability of charged interfaces in ionic systems also depends on specific ion effects. These effects arise from the intrinsic polarizability of ions, defined as the ease with which their electron cloud can be distorted by an electric field. Highly polarizable ions have loosely bound electrons and interact more strongly with surfaces, whereas low-polarizability ions remain tightly hydrated and less responsive to local potentials.

Ions are often categorized according to the Hofmeister series into chaotropes and kosmotropes. Chaotropic ions are large, weakly hydrated, and highly polarizable; they tend to disrupt the surrounding ionic or solvent structure and adsorb readily onto surfaces. Their presence generally enhances colloidal stability by increasing surface charge or altering interfacial energy. In contrast, kosmotropic ions are small, strongly hydrated, and exhibit low polarizability. They reinforce the local ionic structure, remain in the bulk phase, and effectively screen surface charge, which promotes aggregation.

Research have shown that in the case of Au NPs the effect of different ions on colloidal stability is significant [51]. This ion-specific behaviour explains why colloidal stability changes with different ionic liquids or electrolytes, even when the ionic strength is constant.

Steric Stabilization

Steric stabilization is an additional, non-DLVO mechanism that contributes to colloidal stability. Here, the particle surfaces are coated with polymers, surfactants, or organic ligands [81]. In such systems, adsorbed molecular layers form a physical barrier around each particle, preventing close contact and thereby reducing the likelihood of aggregation.

When two coated particles approach one another, steric repulsion arises once the surface–surface distance becomes smaller than twice the thickness of the adsorbed layer. At this point, the polymer chains begin to overlap, increasing the local polymer concentration and compressing the chains, as illustrated in Figure 3.5. Both effects lead to an increase in free energy, resulting in a repulsive force that drives the particles apart. The magnitude and spatial range of this repulsion depend on the characteristics of the surface-bound polymer, such as molecular weight and solubility in the surrounding medium.

3.3. Combined Potential

This section combines the electrostatic repulsion, the van der Waals attraction, and the Born potential into the total DLVO potential.

Throughout this thesis two types of DLVO-based interaction potentials are used. The first corresponds to the sphere–sphere geometry, valid under the near-field approximation, $h \ll a_1, a_2$. The second corresponds to the sphere–plate geometry. An overview of the interaction potentials used in the non-dimensional framework and in the coarse-grained simulations is given in Table 3.2. In all cases, a hard-sphere repulsion with exponent $n = 12$ is included.

Table 3.2: Total DLVO interaction potential for sphere–sphere and sphere–plate geometries.

Geometry	DLVO Potential	
Sphere–sphere (near-field) $(h \ll a_1, a_2)$	$U_{\text{Tot}}^{ss,nf}(h) = \frac{A\sigma^6}{1260}\frac{a_1 a_2}{a_1+a_2}\frac{1}{h^7} + 128\pi\frac{a_1 a_2}{a_1+a_2}\frac{N_A I k_B T}{\kappa^2}\gamma_1\gamma_2\, e^{-\kappa h} - \frac{A}{6}\frac{a_1 a_2}{a_1+a_2}\frac{1}{h}$	(3.25)
Sphere–plate	$U_{\text{Tot}}^{sp}(h) = \frac{A\sigma^6}{7560}\left[\frac{8a+h}{(2a+h)^7} + \frac{6a-h}{h^7}\right] + 128\pi a\,\frac{N_A I k_B T}{\kappa^2}\gamma_1\gamma_2\, e^{-\kappa h} - \frac{A}{6}\left[\frac{a}{h} + \frac{a}{h+2a} + \ln\left(\frac{h}{h+2a}\right)\right]$	(3.26)

The equations presented in Table 3.2 illustrate the large number of parameters that can be adjusted to modify the resulting potential and, consequently, the system behaviour. One of the main objectives of this thesis is to develop a non-dimensional framework that consolidates these parameters into a minimal set of variables that fully characterise the potential. This chapter has verified the consistency of the applied potentials and examined the limitations associated with their dimensional form. The formulation of the non-dimensional framework is presented in the following section.

4

Generalised DLVO Representation

DLVO theory provides a robust foundation for describing colloidal stability. Research has applied this theory to a wide range of systems, each characterised by distinct parameters. However, no general framework has been developed that unifies these cases and enables direct comparison.

The objective of this chapter is to derive a non-dimensional representation of the DLVO potential. This is achieved by grouping dimensional parameters to a minimal set that can still capture aggregation behaviour. This approach reduces the number of free variables. The framework is developed for both the sphere–sphere and sphere–plate geometries.

DLVO Potential Characteristics

As discussed in Chapter 3, the total DLVO potential depends on a large number of parameters. Small parameter variations strongly affect the potential and reveal their relative contributions. A parameter variation study, presented in Appendix C, strengthens the motivation to formulate the problem in terms of dimensionless parameters.

The qualitative behaviour of the potential can be derived from the amount and position of its extrema. In general, three characteristic forms of the potential can be distinguished: a single primary minimum, a primary and secondary minimum separated by an energy barrier, or a secondary minimum only. These configurations are schematically represented in Figure 4.1. Each configuration reflects a distinct regime of colloidal stability and interaction dynamics.

Primary Minimum Only

This regime occurs when the Electric Double Layer (EDL) is short-ranged and weak. A low surface potential or a high ionic concentration can lead to a compressed EDL. As a result, the potential profile exhibits a deep primary minimum at short interparticle distances, indicating strong attraction. In this case, the electrostatic repulsion is insufficient to form an energy barrier.

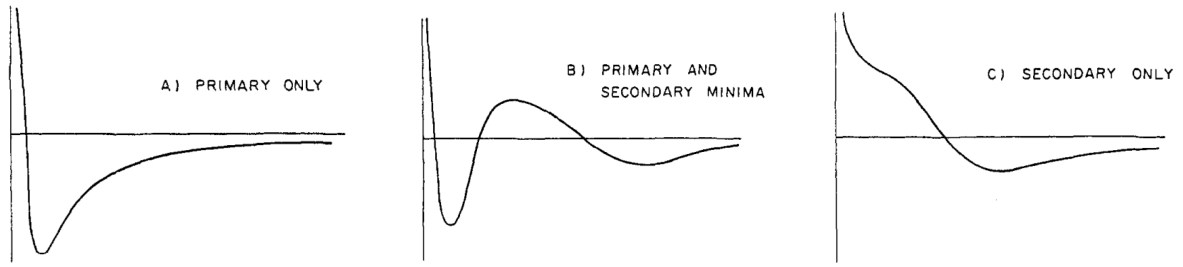

Figure 4.1: Schematic representation of the three possible types of interaction potentials that arise when van der Waals, electrostatic, and mean field Born forces are combined. The left potential corresponds to the weakest degree of electrostatic repulsion, and right potential to the greatest electrostatic repulsion. The middle potential shows a energy barrier in between the two minima [17].

The dominant attractive force causes irreversible aggregation, indicating poor colloidal stability. Therefore, systems described by this potential type often have rapid aggregation.

Primary and Secondary Minima
Moderate electrostatic repulsion results in a more complex potential. It contains both a deep primary minimum at close range and a shallower secondary minimum at larger separation. These minima are separated by an energy barrier generated by the repulsive contribution of the EDL.

The presence of both minima introduces the possibility of reversible aggregation (agglomeration). Thermal fluctuations allow particles to escape the secondary minimum. Systems exhibiting such a potential landscape are generally kinetically stable: particles may become loosely associated in the secondary minimum or form stronger, but potentially irreversible, bonds in the primary minimum. This regime is most relevant to practical colloidal systems with intermediate surface charge and electrolyte concentration.

Secondary Minimum Only
If the EDL is strong and extends far from the particle surface, the primary minimum disappears entirely. The only attractive feature that remains is a shallow secondary minimum located at larger separation distances. High surface charge combined with low ionic strength enhances the electrostatic repulsion and increases the double-layer thickness.

The absence of a primary minimum ensures that colloidal particles remain well dispersed. Interactions in this regime are weak and reversible, typically resulting in stable colloidal suspensions.

Identification of Regions from Extrema

The different potential regimes can be identified by examining the number of extrema and their positions. Potentials that contain both a primary and a secondary minimum show three extrema: two minima separated by a maximum, which represents the energy barrier.

Potentials with only a primary minimum or only a secondary minimum contain a single extremum. The location of this extremum determines the regime. A primary minimum occurs at small separations from the surface. A secondary minimum appears at larger separations, typically several Debye lengths away from the particle surface. By evaluating both the number of extrema and the distance of the extrema from the surface, the three DLVO regimes can be distinguished.

4.1. Dimensionless Formulation of the Potential

First, the DLVO potential for sphere-sphere geometry with the near-field approximation, given in Equation (3.25), is non-dimensionalised. Later, the same derivation is conducted for sphere-plate geometry.

The coefficients of the Born, electrostatic, and van der Waals contributions are denoted by B, C, and D, respectively. The potential is simplified to

$$U(h) = \frac{B}{h^7} + C\, e^{-\kappa h} - \frac{D}{h}. \tag{4.1}$$

To non-dimensionalise the potential, its magnitude is expressed relative to a characteristic energy scale. The thermal energy, represented by $k_B T$, provides a suitable reference, as it reflects the average kinetic energy of the system and thus the characteristic energy scale of interparticle interactions. The potential energy is therefore normalised as $U' = U/k_B T$.

In addition, the separation distance is made dimensionless by introducing the Debye length $\lambda = 1/\kappa$ as the characteristic length scale, which defines the range of electrostatic screening. The dimensionless distance is then given by $h' = \kappa h$. Implementing both scaling relations yields:

$$\begin{aligned} U'(h') =& \frac{B\kappa^7}{k_B T}\frac{1}{h'^7} + \frac{C}{k_B T}e^{-h'} - \frac{D\kappa}{k_B T}\frac{1}{h'} \\ =& \frac{B'}{h'^7} + C' e^{-h'} - \frac{D'}{h'}. \end{aligned} \tag{4.2}$$

The scaling terms are grouped with the coefficients B, C, and D. This results in the dimensionless coefficients B', C', and D'.

4.2. Finding Extrema and Coefficient Definition

The extrema of the dimensionless potential are found by taking the derivative of Equation (4.2) with respect to h' and setting it equal to zero:

$$\frac{\partial U'}{\partial h'} = -\frac{7B'}{h'^8} - C'e^{-h'} + \frac{D'}{h'^2} = 0. \tag{4.3}$$

To further reduce the free parameters of the equation, both B' and C' are normalised by the dimensionless parameter D'. Rearranging terms yields,

$$7\frac{B'}{D'}\frac{1}{(h')^6} + \frac{C'}{D'}(h')^2 e^{-h'} - 1 = 0. \tag{4.4}$$

This relation highlights how the potential's form is governed by two independent dimensionless ratios, B'/D' and C'/D', which together capture the behaviour of the system. Finally, the full analytical forms of the coefficients are given in Table 4.1, together with the compact relative coefficient expressions used in the non-dimensional framework.

Examining the expressions for the coefficient ratios shows a clear simplification. Several physical parameters cancel out or are eliminated entirely. The ratios no longer depend on the particle radii a_1 and a_2. This follows from the near-field approximation ($h \ll a_1,\, a_2$), where the separation distance is much smaller than the particle size. In this limit, the curved surfaces behave as if they were flat, and the radius no longer affects the interaction. The absence of the radius term confirms that the approximation is valid and consistent. The dimensionless ratios B'/D' and C'/D' directly indicate how the system parameters influence the shape and strength of the DLVO potential.

The current coefficients still contain implicit dependencies. For example, κ depends on the ionic strength I, which introduces an unwanted coupling between coefficients. To isolate the effect of each physical parameter, the coefficients are reformulated so that no mutual dependencies remain:

$$\begin{aligned} \frac{C'}{D'} &= 192\sqrt{2}\,\pi\,\gamma_1\gamma_2\frac{\epsilon(k_BT)^2}{Aq^3}\sqrt{\frac{\epsilon k_BT}{N_AI}}, \\ \frac{B'}{D'} &= \frac{4}{105}(\sigma q)^6\Big(\frac{N_AI}{\epsilon k_BT}\Big)^3. \end{aligned} \tag{4.5}$$

Although the expressions in Equation 4.5 are less compact, they reveal the temperature dependence of both coefficients. The relations scale as $B'/D' \sim T^{2.5}$ and $C'/D' \sim T^{-3}$, indicating that temperature has a pronounced influence on the potential.

Table 4.1: Overview of the dimensionless DLVO coefficients and their relative ratios for the sphere-sphere interaction.

Potential Term	Coefficient Definition	Relative Coefficients
Born Repulsion	$B' = \frac{(\sigma\kappa)^6}{1260}\frac{A}{k_BT}\frac{a_1a_2}{a_1+a_2}$	$\frac{B'}{D'} = \frac{1}{210}(\sigma\kappa)^6$
Electrostatic Repulsion	$C' = 128\pi\frac{N_AI}{\kappa^2}\gamma_1\gamma_2\frac{a_1a_2}{a_1+a_2}$	$\frac{C'}{D'} = 768\pi\gamma_1\gamma_2\frac{k_BT}{A}\,\frac{N_AI}{\kappa^3}$
Van der Waals Attraction	$D' = \frac{1}{6}\kappa\frac{A}{k_BT}\frac{a_1a_2}{a_1+a_2}$	

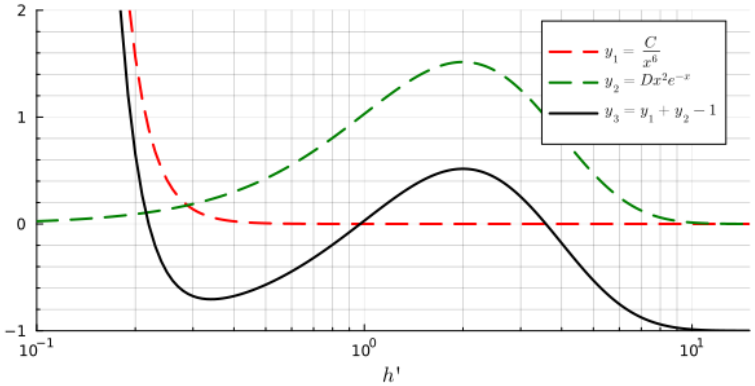

Figure 4.2: Schematic graph of the individual component of Equation (4.4) as functions of the dimensionless separation h'. The red dashed curve represents $y_1 = C/x^6$, the green dashed curve $y_2 = Dx^2e^{-x}$. The solid black curve ($y_3 = y_1 + y_2 - 1$). In the graph: $B'/D' = 10^{-5}$ and $C'/D' = 2.9$.

Analytical Derivations

It would be desirable if Equation (4.4) could be solved analytically. An analytical solution would allow for exact identification of critical regions and thresholds in the behaviour of the system. It would also increase the generality and applicability of the model across different physical systems.

At first inspection, however, Equation (4.4) does not have a straightforward analytical solution. Due to the non-linear coupling between the polynomial and exponential terms. Yet, the first term rapidly approaches zero for $h' > 1$, since the corresponding coefficient lies in the range $B'/D' \in [10^{-9}, 10^{-1}]$ in the most system. The first term can therefore be neglected, yielding the simplified form

$$\cancel{\frac{B'}{D'}\frac{1}{(h')^6}}^{\,0} + \frac{C'}{D'}(h')^2 e^{-h'} - 1 = 0 \tag{4.6}$$

Evaluating the second term of Equation (4.6) shows that it reaches its maximum at $h' = 2$. This observation is supported by Figure 4.2 where the components of Equation (4.4) are shown. Figure 4.2 shows that the first term decays rapidly for $h' > 1$ and the second term exhibits a clear maximum at $h' = 2$.

Accordingly, the condition for the potential to exhibit three extrema rather than a single attractive minimum can be expressed as:

$$\frac{C'}{D'}(h')^2 e^{-h'} - 1 > 0. \tag{4.7}$$

Substituting $h' = 2$ into the expression and rearranging yields the condition $C'/D' > e^2/4 \approx 1.85$. In conclusion, three extrema are present whenever this inequality is satisfied.

Limitations

Several limitations deserve consideration. First, the van der Waals contribution is expressed using a near-field approximation, which becomes inaccurate at larger separations. This approximation tends to overestimate the long-range attraction, effectively shifting the transition between repulsive and attractive behaviour toward smaller distances.

In addition, the electrostatic interaction is described exclusively through the Linear Superposition Approximation (LSA). Although the LSA provides reliable trends at moderate surface potentials and low ionic strength, it does not span the complete range between the constant-charge and constant-potential boundary conditions observed in practice. Real systems typically operate within this intermediate regime, where deviations from the LSA will modify the interaction profile and consequently alter the dimensionless coefficient values.

4.3. Sphere-Plate Analysis

The objective of this section is the same as in the sphere–sphere case: to obtain a general description of the three regimes of the DLVO potential for a sphere–plate interaction. By applying a non-dimensionalisation procedure, the number of independent control parameters is reduced. The derivation follows the same procedure, except that the function used to find the extrema is more complex. After completing the derivation, a separate subsection will outline the main differences between the sphere–sphere and sphere–plate interactions.

DLVO Potential

The total potential for the sphere-plate interaction is given as

$$\begin{aligned} U(h) = \frac{A\,\sigma^6}{7560}\left[\frac{8a+h}{(2a+h)^7} + \frac{6a-h}{h^7}\right] \\ + 128\pi\frac{nk_BT}{\kappa^2}\; a\,\gamma_1\gamma_2\; e^{-\kappa h} \\ - \frac{A}{6}\left[\frac{a}{h} + \frac{a}{h+2a} + \ln\left(\frac{h}{h+2a}\right)\right]. \end{aligned} \tag{4.8}$$

All parameters are the same as in the sphere–sphere case. The only difference is that a now denotes the radius of a single sphere. Since only one sphere is involved, no subscripts are needed. First, the near-field approximation is considered, valid for $h \ll a$. Under this assumption, the interaction potential simplifies to

$$U'(h') = \frac{B'}{h'^7} + C'e^{-h'} - \frac{D'}{h'} \tag{4.9}$$

This expression is identical to the sphere–sphere case."Physically, this equivalence arises because, at very small separations, the local geometry of the sphere-plate case is also indistinguishable from that of two flat plates approaching one another. Consequently, the DLVO region plot in the near-field limit is the same for both sphere-sphere and sphere-plate geometries.

To extend the analysis beyond the near-field limit, the full potential over all separations is taken. For readability, the terms inside the square brackets of Eq. (4.8) are replaced by auxiliary functions that depend on the particle radius and the wall separation, (a, h'). Writing the non-dimensional potential in terms of these functions gives

$$U'_{sp}(h') = B'_{sp}f(a,h') + C'_{sp}e^{-h'} - D'_{sp}g(a,h'). \tag{4.10}$$

We define the auxiliary functions with their derivatives with respect to h',

$$\begin{aligned} f(a,h') &= \kappa^6\left(\frac{8\kappa a+h'}{(2\kappa a+h')^7} + \frac{6\kappa a-h'}{h'^7}\right) & g(a,h') &= \kappa a\left[\frac{1}{h'} + \frac{1}{h'+2\kappa a} + \frac{1}{\kappa a}\ln\left(\frac{h'}{h'+2\kappa a}\right)\right] \\ \frac{\partial f(a,h')}{\partial h'} &= 6\kappa^6\left(\frac{h'-7\kappa a}{h'^8} - \frac{9\kappa a+h'}{(2\kappa a+h')^8}\right) & \frac{\partial g(a,h')}{\partial h'} &= \kappa a\left[-\frac{1}{h'^2} - \frac{1}{(h'+2\kappa a)^2} + \frac{2}{h'(h'+2\kappa a)}\right] \end{aligned}$$

Since we no longer invoke the near-field approximation, some geometric factors are captured explicitly by f and g. This is seen because the function still depends on the particle radius a. For comparison purposes, the following factors will be transferred from the function to the dimensionless coefficients, κ^6 and κa in front of their respective functions $f(a,h')$ and $g(a,h')$ and their derivatives. Futhermore, in all the auxiliary functions it can be seen that the particle radius is coupled with κ. We expect to see the same function as long as the factor κa is constant. The final expression of the auxiliary functions will be given as

$$\begin{aligned} f(a,h') &= \frac{8\kappa a+h'}{(2\kappa a+h')^7} + \frac{6\kappa a-h'}{h'^7} & g(a,h') &= \frac{1}{h'} + \frac{1}{h'+2\kappa a} + \frac{1}{\kappa a}\ln\left(\frac{h'}{h'+2\kappa a}\right) \\ \frac{\partial f(a,h')}{\partial h'} &= 6\left(\frac{h'-7\kappa a}{h'^8} - \frac{9\kappa a+h'}{(2\kappa a+h')^8}\right) & \frac{\partial g(a,h')}{\partial h'} &= -\frac{1}{h'^2} - \frac{1}{(h'+2\kappa a)^2} + \frac{2}{h'(h'+2\kappa a)} \end{aligned} \tag{4.11}$$

Table 4.2: Overview of the dimensionless DLVO coefficients and their relative ratios for the sphere-plater interaction.

Potential Term	Coefficient Definition	Relative Coefficients
Born Repulsion	$B'_{sp} = \frac{1}{7560}(\sigma\kappa)^6 \frac{A}{k_B T}$	$\frac{B'_{sp}}{D'_{sp}} = \frac{1}{210}(\sigma\kappa)^6 \frac{1}{\kappa a}$
Electrostatic Repulsion	$C'_{sp} = 128\pi a \frac{N_A I}{\kappa^2} \gamma_1 \gamma_2$	$\frac{C'_{sp}}{D'_{sp}} = 768\pi \cdot \gamma_1 \gamma_2 \frac{k_B T}{A} \frac{N_A I}{\kappa^3}$
Van der Waals Attraction	$D'_{sp} = \frac{1}{6} \frac{A}{k_B T} \kappa a.$	

To avoid confusion, we distinguish the coefficients for the sphere-plate geometry from those of the sphere-sphere case by the subscript (sp). With the auxiliary functions and the sphere–plate coefficients defined, the three DLVO regions can be determined. As before, the derivative of the potential with respect to h' is taken and set equal to zero. Dividing the resulting equation by $D'_{\mathrm{sp}}\, g'(a, h')$ gives:

$$\frac{B'_{sp}}{D'_{sp}} \frac{f'(a,h)}{g'(a,h)} - \frac{C'_{sp}}{D'_{sp}} \frac{e^{-h'}}{g'(a,h)} - 1 = 0 \tag{4.12}$$

This equation will be used to find the extrema and determine the transitions between the DLVO regimes. The corresponding dimensionless prefactors and the relative dimensionless coefficients are given in Table 4.2.

The geometric prefactors are arranged such that the coefficient ratios can be compared directly to the sphere–sphere formulation. The ratio C'_{sp}/D'_{sp} is identical to C'/D', meaning that the relative strength of the electrostatic repulsion is unaffected by the change in interaction geometry. The ratio B'_{sp}/D'_{sp}, however, includes an additional factor of $1/(\kappa a)$ that originates from the geometry of the sphere–plate configuration. Consequently, the ratio between the Debye length and the particle size is an additional prefactor for the aggregation behaviour.

4.4. Physical Interpretation of Dimensionless Coefficients

This chapter reduced the DLVO parameter space to two dimensionless coefficients, B'/D' and C'/D', for both the sphere–sphere interaction (near–field approximation) and the sphere–plate interaction. The purpose of this section is to interpret these dimensionless groups and relate them to their physical meaning, providing intuition for how they govern aggregation behaviour. The sphere–sphere case is discussed first, followed by the sphere–plate interaction.

The coefficient C'/D' represents the relative strength of the EDL repulsion compared with the van der Waals attraction. As shown in Table 4.1, C'/D' increases with the surface potentials γ_1 and γ_2, and decreases with the Hamaker constant A. Small C'/D' values correspond to a regime where van der Waals attraction dominates. Particles then fall directly into the primary minimum. Increasing C'/D' introduces a repulsive contribution, allowing an energy barrier and a secondary minimum to form. At sufficiently large C'/D', the repulsion exceeds the attraction. Only a shallow secondary minimum remains, which promotes colloidal stability.

The coefficient B'/D' reflects the relative length of the EDL. It is proportional to the ratio of the Debye length to the collision parameter. Small B'/D' values indicate a long Debye length. In that case, electrostatic repulsion acts over larger separations, and even moderate C'/D' values are sufficient to establish an energy barrier. As B'/D' increases, the Debye layer becomes shorter. Repulsion then acts only at small separations, and larger values of C'/D' are required to counteract the attractive forces.

Sphere–Plate Interaction

For the sphere–plate interaction, the coefficients are similar to the sphere–sphere case, and therefore their physical interpretation remains the same. The main difference lies in the additional factor (κa) appearing in B'_{sp}/D'_{sp}. Introducing an explicit dependence on the ratio between the particle radius a and the Debye length. However,

the dominant contribution still arises from the ratio between the length of the EDL and the collision parameter $(\sigma\kappa)^6$.

Another advantage of using the dimensionless coefficients is that they are independent of the chosen energy normalisation. While the dimensional coefficients B, C, and D depend on the specific energy normalization used, the ratios B'/D' and C'/D' remove this dependence through division. As a result, the interaction behaviour can be compared across different systems without being affected by the absolute energy scale. This energy independence highlights the generality of the framework and its applicability to a wide range of physical systems.

In the next section, results of the non-dimensionalisation will be presented and explained.

5

Classification of DLVO Regimes

This chapter presents results derived from the dimensionless formulation of the DLVO potential. Based on the dimensionless coefficients, the three characteristic regions are identified. In addition, semi-stable regions are introduced to further refine the classification of interaction regimes. Section 5.1 presents this approach for the sphere–sphere geometry. Section 5.2 applies the same approach to the sphere–plate geometry.

5.1. Sphere–Sphere Interaction

To determine the ranges of the dimensionless coefficients, values reported in literature are used. Liu et al. [47] reports surface potentials of approximately 70 mV for silica nanoparticles in dilute electrolyte solutions. The combination of these measurements results in a Debye length that is much larger than the collision parameter. This corresponds to $B'/D' = 10^{-8}$ and $C'/D' = 30$, which define the lower and upper bounds for B'/D' and C'/D', respectively. The lower limit of C'/D' is set to zero, representing the absence of a surface potential. In molten salts, the Debye length is typically shorter than the ionic diameter ($\kappa < \sigma$), corresponding to $B'/D' > 10^{6}$. To improve visual clarity, the parameter space is restricted to the ranges listed in Table 5.1 without losing the relevant interaction regimes.

The results of the sphere-sphere regime classification are shown in this section. This interaction is with the near-field approximation $h \ll a_1, a_2$. Combinations of $(B'/D', C'/D')$ that yield three solutions to the extrema equation, and therefore three extrema in the potential, are classified as the *Energy Barrier* regime. To distinguish between the regimes *Only primary minimum* and *Only secondary minimum*, an additional criterion is used. The boundary between these regimes is defined as $x_{\text{min}} = \sigma$, meaning that the minimum must lie within the collision length to be classified as aggregation.

Figure 5.1 shows the regions of the DLVO interaction potential in the $(B'/D', C'/D')$ parameter space. The colored regions indicate distinct interaction regimes. In the pink region (*Only primary minimum*), attractive van der Waals forces dominate and particles aggregate irreversibly. In the blue region (*Energy Barrier*), the potential contains both a primary and a secondary minimum, separated by an energy barrier that slows aggregation. In the yellow region (*Only secondary minimum*), the repulsive double–layer interaction outweighs the attraction, resulting in a shallow secondary minimum and stable colloidal dispersion. The boundaries mark where the number and type of extrema in the DLVO potential change. Figure 5.4 also shows the predicted boundary between the primary minimum and the energy barrier regime for $C'/D' = e^2/4 \approx 1.85$, Equation (4.7).

Table 5.1: Parameter space explored for the non-dimensional interaction parameters B'/D' and C'/D'. Where the minimum value of B'/D' and the maximum value of C'/D' are from research performed by Liu et al. [47]. The maximum value for B'/D' is determined by the MSR case.

Parameter	Minimum	Maximum
B'/D'	10^{-9}	10^{3}
C'/D'	0	10

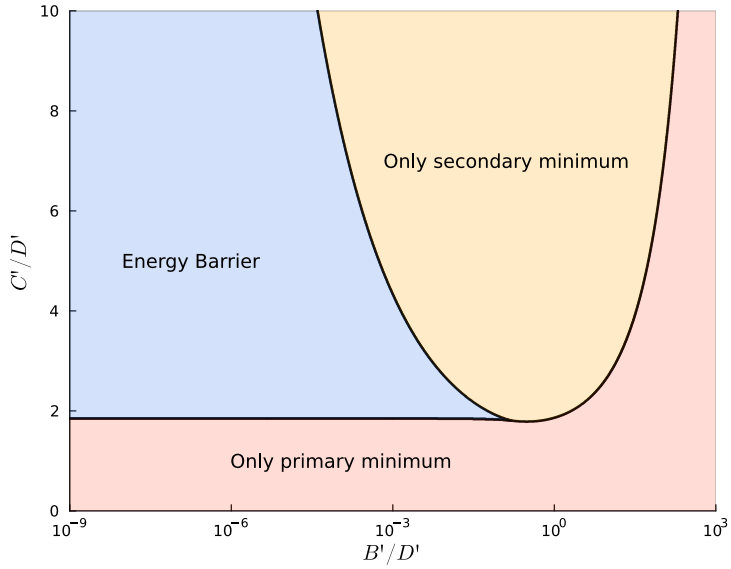

Figure 5.1: Non-dimensional DLVO region plot in the $(B'/D', C'/D')$ plane. The boundaries separate the regimes where only a primary minimum, only a secondary minimum, or both minima are present.

Extension of The Identified Regions

Describing the DLVO potential using only three distinct regions may not be sufficient. In certain cases, the potential exhibits three extrema, yet the observed behaviour clearly indicates either rapid aggregation or a stable suspension. These intermediate cases can be classified as *semi-stable*, where the number of extrema alone does not fully capture the system dynamics.

Two characteristic scenarios can be distinguished. The first occurs when a primary minimum exists but remains above the energy axis. In this case, aggregation into the primary minimum may still occur; however, because the well is shallow, particles can escape when sufficient thermal energy is available. The system then relaxes into the deeper and more favourable secondary minimum, corresponding to a stable configuration. Although the potential formally contains two minima and an energy barrier, the effective behaviour is that of a stable dispersion with only transient aggregation. For evaluating the depth and heigth of the primary well and the energy barrier, the value of D' is set to unity ($D' = 1$).

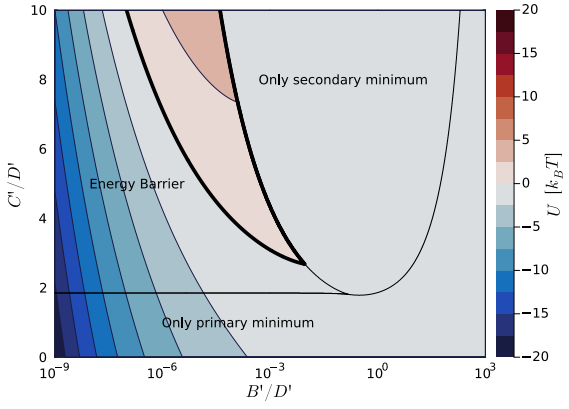

Figure 5.2: DLVO interaction map showing the height of the primary minimum for varying (C′/D′) and (B′/D′). The bold lines mark the area where the primary minimum has a positive value. Indicating a semi-stable area for clusters in favor of a stable solution.

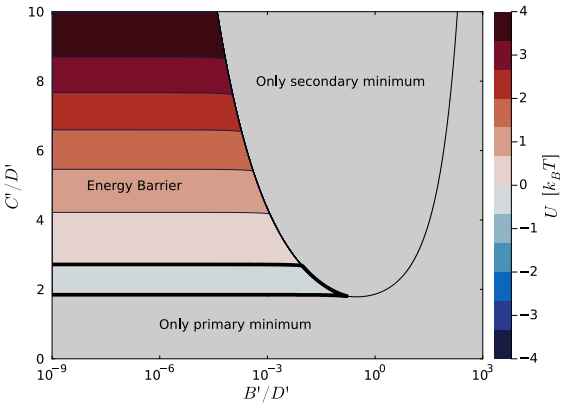

Figure 5.3: DLVO interaction map showing the height of the energy barrier for varying (C′/D′) and (B′/D′). The bold lines mark the area where the energy barrier has a negative value. Indicating a semi-stable area for clusters in favor of aggregation.

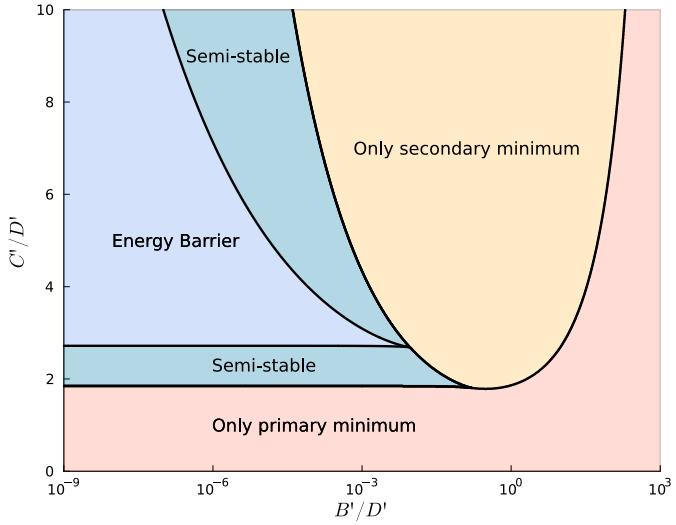

Figure 5.4: Non-dimensional DLVO region plot in the $(B'/D', C'/D')$ plane. The boundaries separate the regimes where only a primary minimum, only a secondary minimum, or both minima are present.

The second scenario arises when the potential again contains three extrema, but the energy barrier between the two minima lies below the energy axis. The barrier slows the aggregation minimally. Thus, the system behaves as if only a single attractive minimum were present, leading to rapid aggregation. In this case, the formal structure of the potential suggests multiple extrema, but its shape dictates unstable behaviour.

Figure 5.2 shows the DLVO regions in the $(B'/D', C'/D')$ plane together with the height of the primary minimum in units of k_BT. The shallow black lines mark transitions in DLVO regimes, separating the three regimes identified earlier. The highlighted area enveloped in the thicker black lines, represent the combination for which the primary minimum lies above the energy axis. Therefore, this regime can be labeled as semi-stable.

Figure 5.3 shows the DLVO regions in the $(B'/D', C'/D')$ plane, together with the height of the energy barrier. The colour scale is given in units of k_BT. The solid black lines again mark the transitions in the number of extrema, while the dashed contour indicates the zero-barrier level that separates stable from semi-stable regimes.

Including the semi-stable regimes refines the DLVO classification. Figure 5.1 shows the traditional region map, while Figure 5.4 includes the semi-stable regimes in addition to the classical DLVO regions. This extended map provides a clearer representation of the interaction regimes for the sphere-sphere case.

The agglomeration regime can be interpreted from Figure 5.4. In the transition region between the “Only primary minimum” and “Only secondary minimum” domains, a minimum is present at a separation distance larger than the collision parameter, $x_{\min} > \sigma$. In this condition, particles experience a stable minimum slightly beyond one particle spacing, leading to clusters of particles located close to one another without irreversible aggregation. The area of the diagram near this boundary may therefore be classified as an agglomeration regime, although further analysis is required to establish a precise quantitative condition.

It must be noted that the region map is obtained under the near-field approximation. This simplifies the derivation and renders the region boundaries independent of particle size. The approximation is well justified at short separations, but its accuracy decreases at larger particle distances.

5.2. Sphere-Plate Interaction

The sphere–plate regime identification follows the same procedure as the sphere–sphere case. The difference lies in the expression used to determine the extrema of the non-dimensional potential, which is given in Equation (4.12). This section focuses on the resulting DLVO region maps and their comparison with the sphere–sphere case.

For this geometry, additional care is required. In contrast to the sphere–sphere formulation, the extremum condition contains a dependence on both the inverse Debye length κ and the particle radius a. At first inspection, Equation (4.12) appears to contain three independent variables: B'/D', κ, and a. However, Table 4.2 shows that B'/D' is interdependent on κ and a as well. Fixing the particle radius a and collision parameter σ reduces the system to two free variables B'/D' and κ. Rearranging the definition of B'/D' yields the relation:

$$\kappa = \frac{1}{\sigma} \sqrt[5]{210 \frac{a}{\sigma} \frac{B'}{D'}}. \tag{5.1}$$

This allows the computation of κ for each value of B′/D′ This value is then substituted into Equation (4.12) to determine the number and type of extrema and thus classify the interaction regime.

Figures 5.5a–5.5d show the resulting DLVO region maps for particle radii $a \in \{1, 10, 100, 1000\}$ nm. However, a different criterion distinguishes the ”Only primary minimum” and the ”Only secondary minimum” regimes ($x_{\text{min}} = 1.3\sigma$). The boundary used for the sphere-sphere geometry resulted in misalignment of the regimes. The shift of the boundary is likely related to the change in geometry. Further research is required to determine the origin of this effect.

For large particle radii (Figure 5.5d), the structure of the regime map closely resembles that of the sphere–sphere case. This behaviour is expected: as a increases, the sphere approaches a flat surface locally, and the interaction converges towards a plate–plate limit. Consequently, for large radii, the sphere–plate geometry converges to the near-field approximation used in the sphere–sphere analysis.

For smaller particles, the influence of geometry becomes more pronounced. The aggregation regime decreases significantly at low values of B'/D'. Physically, the EDL becomes relatively larger in size. In this situation, even a modest electrostatic repulsion (low C'/D') can generate an energy barrier. As B'/D' increases, the EDL becomes shorter. The relative size of the particle then plays a smaller role in the interaction behaviour and the aggregation regimes slowly grows larger.

In Figures 5.5a–5.5d, the boundary between the “Only secondary minimum” and “Only primary minimum” regimes shows a slight irregularity. Increasing the resolution of the (B'/D', C'/D') grid does not remove this effect. The origin of this irregularity requires further investigation.

Finally, the region maps show a horizontal shift towards lower B'/D' values with increasing particle radius. This trend follows directly from the $1/(\kappa a)$ term in the coefficient B'/D', which causes larger particles to experience an effectively shorter Debye layer in non-dimensional space. Similar trends have also been reported by Lin and Wiesner [46].

5.3. Molten Salt Reactor

In molten salt reactors, the high concentration of ions create an extremely high ionic strength environment. A high ion concentration compresses the electric double layer, resulting in a very short Debye length and therefore large values of the ratio B'/D', typically larger than 10^6. From the DLVO regime maps for both sphere–sphere and sphere–plate interactions, such large B'/D' values place the system entirely within the “Only primary minimum” regime. Under these conditions, electrostatic repulsion becomes negligible and particles are expected to aggregate irreversibly.

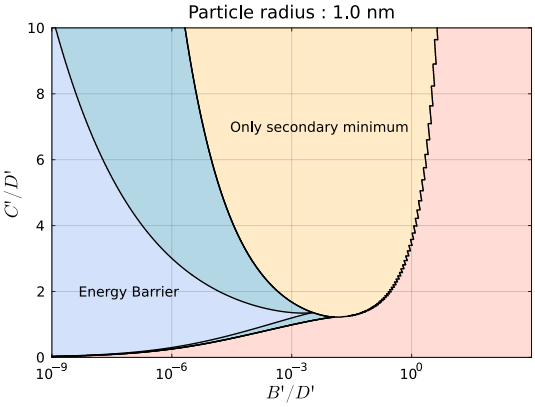

(a) Particle radius $a = 1$ nm

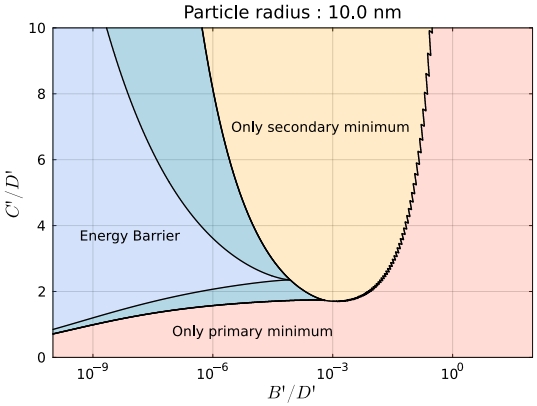

(b) Particle radius is $a = 10$ nm

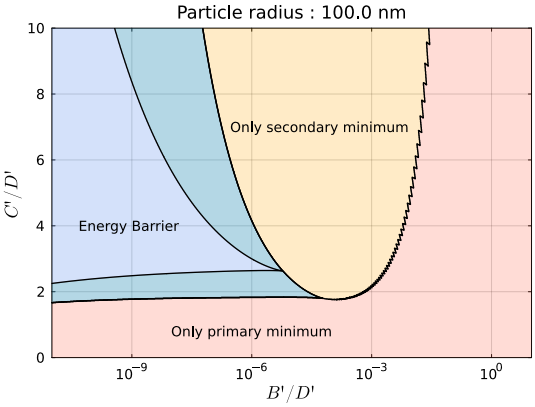

(c) Particle radius is $a = 100$ nm

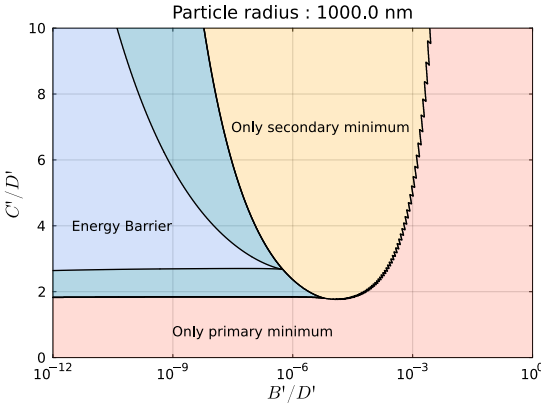

(d) Particle radius is $a = 1000$ nm

Figure 5.5: DLVO regime map for the sphere–plate interaction for different values of a. The green areas are the ”semi-stable” regimes. The boundary between aggregation and stable dispersion is set to $x_{\min} = 1.3\sigma$ for better allignment. As a decreases, the “Only primary minimum” region reduces, indicating slower aggregation behaviour. Physically the relative size of the EDL grows as the radius decreases.

Part II

Coarse-Grained Simulations

6

Principles of Molecular Dynamics

The other objective of this thesis is to link the non-dimensional DLVO framework to the aggregation dynamics observed in the simulations. Molecular Dynamics (MD) and Coarse-Grained (CG) simulations are well suited for this purpose. For meaningful results, it is essential that the simulations represent the correct particle interactions and preserve physical quantities such as kinetic energy.

This chapter provides the theoretical foundation required for the simulation framework used in Part II of this thesis. Section 6.1 introduces the principles of MD, including the force evaluation and numerical integration of particle motion. Section 6.2 outlines the statistical ensembles commonly applied in MD and their implications for conservation properties. Section 6.3 discusses the use of periodic boundary conditions to ensure physically representative behaviour in finite systems. Finally, Section 6.4 introduces the concept of CG simulations.

6.1. Force Derivation and Atomic Motion

Molecular Dynamics (MD) simulations are a computational technique used to study the time evolution of interacting particles based on classical mechanics. The fundamental idea is straightforward: given the initial positions and velocities of all atoms, the interatomic forces are computed, and Newton's equations of motion are integrated in time to obtain new positions and velocities. Repeating this procedure over many simulation steps yields a deterministic trajectory describing the microscopic motion of all particles in the system.

The dynamics of each atom are governed by Newton's second law of motion [67]:

$$m_i \frac{d^2 \mathbf{r}_i}{dt^2} = \mathbf{F}_i, \tag{6.1}$$

where m_i is the mass of particle i, $\mathbf{r}_i$ its position vector, and $\mathbf{F}_i$ the total force acting on it. The force on each particle is obtained from the negative gradient of the total potential energy U:

$$\mathbf{F}_i = -\nabla_{\mathbf{r}_i} U(\mathbf{r}_1, \mathbf{r}_2, \ldots, \mathbf{r}_N), \tag{6.2}$$

where U represents the interatomic potential that describes the interactions between particles. The potential can include pairwise terms (such as Lennard-Jones or DLVO) and many-body corrections, depending on the level of detail in the model. Evaluating equations (6.1) and (6.2) updates the positions and velocities using the Velocity-Verlet algorithm.

Velocity-Verlet Algorithm

The time integration of Eq. 6.1 is typically performed using the Velocity-Verlet algorithm, which offers both numerical stability and good energy conservation. The update equations are given by:

$$\begin{aligned} \mathbf{r}_i(t + \Delta t) &= \mathbf{r}_i(t) + \mathbf{v}_i(t)\Delta t + \tfrac{1}{2}\mathbf{a}_i(t)\Delta t^2 + \mathcal{O}(\Delta t^3), \\ \mathbf{v}_i(t + \Delta t) &= \mathbf{v}_i(t) + \tfrac{1}{2}\left[\mathbf{a}_i(t) + \mathbf{a}_i(t + \Delta t)\right]\Delta t + \mathcal{O}(\Delta t^3), \end{aligned} \tag{6.3}$$

where $\mathbf{v}_i$ and $\mathbf{a}_i$ denote the velocity and acceleration of particle i, respectively. The acceleration follows directly from the computed force as $\mathbf{a}_i = \mathbf{F}_i/m_i$. From Eq. 6.3, it follows that the local truncation error of the Velocity-Verlet algorithm is of order $\mathcal{O}(\Delta t^3)$, while the global truncation error accumulates as $\mathcal{O}(\Delta t^2)$ [45].

The main advantages of the Velocity-Verlet algorithm are its *time reversibility* and *phase-space conservation* (symplecticity). Time reversibility implies that if the sign of Δt is reversed, the integrator retraces the exact same trajectory backwards in time. This property ensures that no systematic energy drift occurs due to directional integration bias. Symplecticity means that the algorithm conserves the phase-space volume, in accordance with Liouville's theorem. In practice, this ensures that the geometric structure of the Hamiltonian system is preserved, preventing artificial damping or amplification of energy during long trajectories.

Because the Velocity-Verlet algorithm is both symplectic and time-reversible, the total energy does not drift but fluctuates around a constant mean value. These fluctuations remain bounded even over very long simulations, which makes the method particularly suitable for microcanonical (NVE) simulations.

Additional benefits of the algorithm include its efficiency and compatibility with thermostats, in particular Andersen. The scheme requires only a single force evaluation per timestep and minimal memory storage for positions, velocities, and accelerations. This makes the Velocity-Verlet method computationally efficient while maintaining high accuracy for small timesteps.

6.2. Statistical Ensembles

In Molecular Dynamics (MD), the concept of statistical ensembles defines how a system exchanges energy, volume, and particles with its surroundings. Each ensemble specifies which macroscopic quantities are conserved and which are allowed to fluctuate. This section discusses the most fundamental ensemble, the *Microcanonical ensemble (NVE)*, and the most commonly used, the *Canonical ensemble (NVT)*. Finally, the ensemble most suitable for the present system is evaluated.

Microcanonical Ensemble (NVE)

The NVE ensemble keeps the number of particles (N), volume (V), and total energy (E) constant. It represents the most fundamental form of molecular dynamics and corresponds to a perfectly isolated system, where no exchange of energy (heat or work) with the environment occurs. The total energy is composed of both kinetic and potential contributions,

$$E = K + U, \tag{6.4}$$

and remains constant in an ideal simulation with perfect numerical integration.

The NVE ensemble is often used for testing and validation, as it provides a direct measure of how well energy is conserved by the chosen integration scheme. It is also valuable for studying the natural dynamics of a system without the influence of thermostats or barostats. However, because the temperature is not explicitly controlled, the kinetic energy of the system depends on the initialisation of the system. As a result, conservation of total energy may lead to a system with a different kinetic energy than the one assigned at the start. Moreover, the NVE ensemble does not represent realistic experimental conditions, where systems are typically in thermal contact with their surroundings.

Canonical Ensemble (NVT)

The NVT ensemble keeps the number of particles (N) and volume (V) constant while maintaining a fixed temperature (T) by coupling the system to a heat bath or thermostat. This setup corresponds to most experimental situations, where temperature is constant but energy can be exchanged with the environment. In this ensemble, temperature is directly linked to the average kinetic energy of the system according to the equipartition theorem:

$$K = \tfrac{1}{2} k_B T N \quad \text{per degree of freedom.} \tag{6.5}$$

For a system with purely translational motion in two dimensions, the total kinetic energy is $K = k_B T N$, while for a three-dimensional system, $K = \frac{3}{2} k_B T N$. It is important to note that this relationship assumes that the degrees of freedom are limited to translational velocities. In molecular systems, additional degrees of freedom, such as vibrational and rotational motions, contribute to the total kinetic energy.

The NVT ensemble is most commonly used in MD simulations because it provides thermodynamic control while allowing accurate sampling of equilibrium configurations. It offers a good compromise between physical realism,

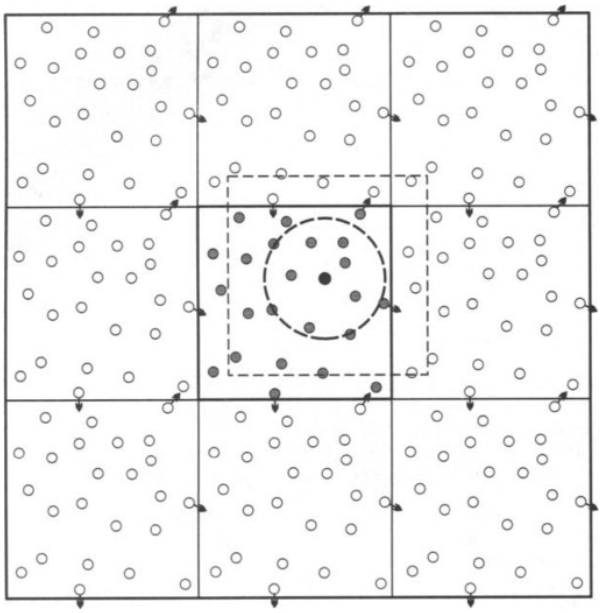

Figure 6.1: A schematic representation of a 2D simulation cell with periodic boundary conditions at all sides. The minimal image convention is represented as the dashed box around the black particle [62].

numerical stability, and computational efficiency.

To maintain a constant temperature, the system is coupled to a thermostat, which regulates the exchange of energy between the system and the external heat bath. The principles and implementation of thermostats are explained in the following section.

6.3. Periodic Boundary Conditions

To approximate an infinite system, periodic boundary conditions are applied. Figure 6.1 shows a simulation cell with the periodic boundary conditions applied. In this approach, the simulation cell (cell with gray particles) is surrounded by identical copies of itself in all spatial directions (cells with white particles. When a particle crosses the boundary of the primary cell, it re-enters the domain from the opposite side with the same velocity. This ensures continuity of both position and momentum across boundaries.

The periodic boundary condition also implies that a particle in the simulation cell near the boundary interacts with both the real particles in the central cell and virtual particles in neighbor replicated cells. Hence, it may arise that a certain particle and its replicated virtual particles in the ambient cells have to be considered as interacting with the particle of interest. To prevent the particles from interacting with both the particle in the simulation cell and its replicas in the virtual cells, a minimum image convention is applied [73]. This is illustrated in figure 6.1 as the dashed line box. Basically, an imaginary box with the same dimensions as the simulation cell is drawn with the particle of interest centered inside. Then, only the particles inside this imaginary box are considered for interaction.

The use of periodic boundary conditions allows a relatively small simulation cell to reproduce the behavior of a bulk system very well. As a result, finite-size effects are minimized while computational cost remains manageable.

6.4. Coarse-Grained Molecular Dynamics

Selecting an appropriate simulation approach is not straightforward. Popular approaches are Molecular dynamics (MD) and continuum dynamics. It will be briefly discussed what these techniques are with their benefits and disadvantages.

Molecular dynamics is typically understood as modelling the motion of individual particles by solving Newton's laws of motion and, when relevant, Maxwell's equations of electrodynamics. This approach has proven effective for studying processes such as atomic diffusion, protein folding , and solid–liquid interface formation [30, 72].

While MD provides detailed, physically consistent results, its computational cost increases rapidly with the number of particles in the system. Since the computational effort scales approximately with $\mathcal{O}(N^2)$ for systems with N interacting particles, atomistic simulations become impractical for systems exceeding a few thousand particles.

Continuum dynamics, in contrast, describes the motion of matter as a continuous medium rather than as a collection of discrete particles. Instead of resolving individual atomic motions, continuum models treat physical quantities such as velocity, temperature, and concentration as smoothly varying fields, governed by conservation equations for mass, momentum, and energy. This approach is well suited for studying macroscopic transport processes, including heat conduction, viscous flow, and diffusion, where microscopic fluctuations average out. However, continuum simulations lose validity as the system size decreases. When the characteristic length scale approaches the nanometer or even micrometer range, the atomic interactions start to dominate the system behavior. In this work, the objective is to simulate the aggregation of nanoparticles, a process governed by interparticle potentials and discrete collisions. It is therefore essential to employ a particle-based approach that explicitly resolves these interactions rather than a continuum description.

Coarse-grained (CG) simulations have therefore emerged as an alternative to model large and complex systems efficiently. In this approach, groups of atoms are represented by single interaction sites, reducing the total number of degrees of freedom. This allows for larger time steps and longer simulation times while preserving the essential physical interactions. The resulting lower resolution makes CG simulations well suited for studying mesoscale processes such as aggregation, diffusion, and sedimentation [36]. Still, the system computation power scales with the amount of particles by $\mathcal{O}(N^2)$ [31].

The system studied in this work lies between classical molecular dynamics and continuum dynamics. As introduced in Chapter 1, the focus of this thesis is on the aggregation of SFPs clusters. These clusters are too large to be treated effectively with fully atomistic simulations, yet too small for a continuum description. Coarse-grained molecular dynamics provides the appropriate framework to bridge this intermediate regime and capture the essential dynamics of NP aggregation.

Coarse-Grained Methodology

Coarse-grained (CG) simulations represent groups of atoms as single interaction sites, commonly referred to as beads. Each bead acts as a point mass from which all interparticle forces originate and to which all interactions are applied. Since a bead represents multiple atoms, its interactions cannot be obtained by simply multiplying atomistic potentials by the number of atoms within the bead. The collective behaviour of atoms introduces nonlinear effects that modify the effective potential between coarse-grained sites.

To account for these effects, coarse-grained simulations rely on *force-field optimization* techniques. In this process, the parameters, such as interaction strengths and equilibrium distances, are systematically adjusted to reproduce properties obtained from simulations to match experimental data. Depending on the desired level of accuracy, this optimization may involve fitting to structural quantities (e.g. radial distribution functions) or thermodynamic observables (e.g. density or surface tension). The resulting coarse-grained potential provides an effective description at a reduced level of resolution.

Parameter Optimization

Another advantage of coarse-grained simulations (CGS) of ionic liquids is the ability to define bead groupings such that each bead is electrically neutral. In our case, the eutectic IL LiCl-KCL is modelled. Here, an example of a constructed bead is the combination of one potassium ion (K^+), one lithium ion (Li^+) and two chloride ions ($2Cl^-$). Almost mimicking the partial concentration of the eutectic liquid. As the bead represents more particles, the true concentration can be approached. The resulting bead inherits the combined mass and interaction characteristics of both ions, while their opposite charges cancel out.

The primary benefit of defining electrically neutral beads is that the Coulomb potential does not need to be evaluated. The Coulomb interaction is long-ranged and computationally expensive, since it decays slowly with distance and typically requires additional summation techniques. However, this simplification also removes ion–ion electrostatic interactions, which may reduce the physical accuracy of the simulation. In conclusion, representing the ionic liquid with charge-neutral coarse-grained beads increases efficiency without sacrificing the essential structural and dynamical properties of the system.

The eutectic IL LiCl-KCL is modelled using a Lennard–Jones (LJ) potential. The potential describes the pairwise

interaction between two coarse-grained beads as

$$V_{\mathrm{LJ}}(r) = 4\epsilon_{cg}\left[\left(\frac{\sigma_{cg}}{r}\right)^{12} - \left(\frac{\sigma_{cg}}{r}\right)^{6}\right], \tag{6.6}$$

where r is the center-to-center distance between two beads, and the parameters σ_i and ϵ_i represent the effective distance and energy scales of interaction for bead type i. These parameters are optimized to reproduce relevant experimental data, such as density, viscosity, and radial distribution functions, ensuring that the coarse-grained model accurately captures the structural and thermodynamic properties of the ionic liquid.

7

Methodology

Chapter 7 describes the methodology for the coarse-grained molecular dynamics simulations. The aim is to outline all steps and assumptions such that the simulations can be reproduced in future work. Section 7.1 introduces the computational framework. The procedure used to determine bead size and the mapping from atomistic to coarse-grained representations is shown in Section 7.2, followed by an overview of the interaction potentials that govern the particle dynamics in Section 7.3. Section 7.4 describes the simulation setup, covering system initialisation and thermostat configuration. Section 7.5 covers the simulation model. The chapter concludes with the post-processing tools used to analyse and visualise aggregation behaviour in Section 7.6.

7.1. Simulation Framework

All simulations in this study are performed using Julia v1.10 in combination with the Molly.jl molecular dynamics (MD) library. Julia is a high-level programming language designed for numerical and scientific computing. It employs a just-in-time (JIT) compiler and a type inference system, providing computational efficiency comparable to statically compiled languages such as C. Krishna et al. [41] even showed that Julia outperforms C and python on matrix multiplications and solving the heat equation. Julia also supports GPU computing, enabling computational acceleration. In addition, Julia supports parallel execution across multiple CPU cores and nodes, allowing scaling for large MD systems.

The choice for Julia is motivated by its computational speed and its use within the Reactor Physics and Nuclear Materials group. As mentioned earlier, this research is part of a broader PhD project aimed at simulating the life cycle of SFP NP in molten salt systems. The larger research framework couples these microscopic simulations to continuum scale CFD models in a Julia environment.

Alternative frameworks, such as the Large-scale Atomic/Molecular Massively Parallel Simulator (LAMMPS), were also considered. LAMMPS is a well-established and validated MD package, particularly suited for large-scale atomistic simulations. However, its input-output structure and limited interoperability with Julia-based projects make it less favorable for the present objective.

7.2. Atomic Density of Molybdenum Clusters

Studies on noble metal fission product deposition in molten salt reactors have shown that the resulting NPs typically range in size between 10 nm and 200 nm [19]. Although these dimensions may appear modest, they are already considerable for molecular dynamics simulations, where computational cost increases rapidly with system size.

The atomic number density n of a material can be derived from its mass density ρ, molar mass M, and Avogadro's number N_A as follows:

$$n = \frac{\rho N_A}{M}. \tag{7.1}$$

Depending on the dimensions of the system, the corresponding cluster volume (or area in the case of two-dimensional clusters) can be used to estimate the number of atoms required to represent the NP. The calculated

values for both two-dimensional and three-dimensional molybdenum clusters are summarized in Table 7.1.

Table 7.1: Comparison of the number of atoms in molybdenum clusters for two and three dimensions.

Dimensions	**Radius** r (nm)	**Volume / Area**	**Atomic density** n	**Atoms** N
2D	1	3.14 nm^2	16 atoms/nm^2	50
	10	314.15 nm^2	16 atoms/nm^2	5 026
	100	31 415.9 nm^2	16 atoms/nm^2	502 654
3D	1	4.19 nm^3	64 atoms/nm^3	268
	10	4 188.79 nm^3	64 atoms/nm^3	268 082
	100	4 188 790 nm^3	64 atoms/nm^3	268 879 360

The number of atoms needed for a specific cluster size in two and three dimensions is directly related to the computational cost of MD simulations. The simulations in this research

7.3. Simulation Method

This section describes the numerical framework used to simulate the aggregation behaviour of NPs under DLVO-driven interactions. The methodology follows directly from the theoretical developments in Chapters 3 and 4 and is designed to operate within the same dimensionless parameter space. All simulation components are introduced, including the formulation of the interparticle potential, the numerical integration scheme, the thermostat used for temperature control to achieve a physically representative environment. The goal of this section is to provide a clear overview of the full simulation configuration.

7.3.1. Interaction Potentials

In Chapter 3, it was shown that the choice of interaction potential strongly influences the behaviour observed in MD simulations. The accuracy and validity of the results therefore depend on selecting the appropriate potentials.

A system containing N distinct particle types requires a total of $\sum_{i=1}^{N} i$ unique pairwise interactions. The system includes two particle types: molybdenum clusters and ionic-liquid beads. Accordingly, three interactions must be specified, as summarised in Table 7.2. The cluster–cluster interactions are governed by the DLVO potential presented earlier in this thesis. The ionic-liquid beads interact via a Lennard–Jones potential using coarse-grained parameters. Finally, the cluster–ion interactions are also described by a Lennard–Jones form.

Table 7.2: Overview of interaction types and corresponding potential models used in the simulation.

Interaction	**Type**	**Physical Meaning**	**Potential Model**
Mo–Mo	Solid–solid	Cluster interaction	DLVO
Bead–Bead	Liquid–liquid	Solvent structure	Coarse-grained LJ (neutral bead)
Mo–Bead	Solid–liquid	Wetting	Cross LJ or fitted potential

Metallic clusters

In the previous chapters, it was shown that the strong electrostatic screening in molten salt reactors results in extremely short Debye lengths, often comparable to or smaller than the ionic diameter. Combined with the relatively low surface potentials expected for solid fission products, the DLVO interaction in MSR conditions reduces effectively to a Lennard–Jones–type potential. For the purpose of this study, the molten salt and NP interactions are explored across the full DLVO parameter space. This allows the qualitative relation between the non-dimensional stability framework and the resulting aggregation kinetics to be established. Subsequently, the outcomes are interpreted in the context of MSR-relevant conditions. This section describes how the potential is implemented within the framework developed in the preceding part.

In Chapter 4, the dimensionless form of the DLVO potential is derived and shown in Equation (4.2). To remain consistent with that framework, the equation is reformulated such that coefficients B'/D' and C'/D' appear explicitly. This representation allows for a direct comparison between regimes and the simulation results.

The DLVO potential used in the simulations is expressed as:

$$\begin{aligned} U'(h') =& D'\Big(\frac{B'}{D'}\frac{1}{h'^7} + \frac{C'}{D'}e^{-h'} - \frac{1}{h'}\Big), \qquad \text{with} \\ D' =& \frac{1}{6}\kappa\frac{A}{k_{\mathrm{B}}T}\frac{a_1 a_2}{a_1 + a_2}. \end{aligned} \tag{7.2}$$

From the dimensionless DLVO potential plots, the expected interaction behaviour can be directly inferred by substituting the coefficients B'/D' and C'/D'. The prefactor D' acts solely as an amplitude scaling factor and does not alter the shape of the potential.

Ionic liquid beads
At present, no specific coarse-grained force field has been established for the chosen ionic liquid system, and the corresponding potential parameters are not yet available from literature. Therefore, the simulation framework is initialized using the LJ parameters of Equation (6.6).

Interaction Potential Between Metallic Clusters and Neutral Beads
When defining interactions between different particles, combination rules are required to determine the cross-interaction parameters. The most commonly used are the Lorentz–Berthelot combining rules:

$$\sigma_{ij} = \frac{\sigma_{ii} + \sigma_{jj}}{2}, \qquad \varepsilon_{ij} = \sqrt{\varepsilon_{ii}\varepsilon_{jj}}. \tag{7.3}$$

where the effective interaction distance σ_{ij} is taken as the arithmetic mean and the interaction strength ε_{ij} as the geometric mean of the corresponding single components [78]. Subscripts i and j are used to indicate the different interaction atoms. The DLVO potential used for metal–metal interactions does not readily provide direct analogues of σ_{DLVO} and $\varepsilon_{\mathrm{DLVO}}$. This absence complicates the application of Lorentz–Berthelot mixing rules for the cross interaction. Therefore, in this work we adopt the same Lennard–Jones form used for the neutral ionic beads to model the metal–bead interaction.

7.3.2. Reproducibility

Reliable reproducibility of simulation results requires strict control over the system initialization. To ensure that identical simulations can be recreated, each stochastic component of the model is initialized using a predefined random number seed. The random seed determines the sequence of random numbers used to generate the initial velocities and to evaluate collision events in the thermostat. By fixing this value, all subsequent random operations become fully deterministic, allowing the simulation to be repeated exactly.

Initialization
Since the DLVO-potential blows up for small distances, it is important not to initialize the particles on top of each other. The particles are initialized a minimum distance away from each other to prevent the energies from blowing up. The velocities are initialized according to the Maxwell-Boltzmann distribution. The reason is that at thermal equilibrium, the velocities of the particles are distributed accordingly. The one-dimensional Maxwell-Boltzmann distribution is given by:

$$f(v) = \sqrt{\frac{m}{2\pi k_B T}}\,\exp\left(-\frac{mv^2}{2k_B T}\right). \tag{7.4}$$

This function represents the form of a Gaussian. The factor in front of the Gaussian makes sure the area under the equation is equal to one, representation a true probability distribution. The velocity vectors for higher dimensions are constructed by taking the velocity from the one-dimensional distribution for each axis.

Andersen Thermostat
The Andersen thermostat is a stochastic method for sampling the canonical (NVT) ensemble in molecular dynamics simulations. At each time step of duration Δt, every particle undergoes a virtual collision with an external heat bath with probability

$$P = \frac{\Delta t}{\tau}, \tag{7.5}$$

where τ is the characteristic collision time. When a collision is triggered, the particle velocity is reassigned from a Maxwell–Boltzmann distribution at the target temperature T. Through these re-sampling events, the Andersen thermostat enforces the correct kinetic energy distribution and ensures proper NVT ensemble statistics.

The choice of τ strongly affects the simulation dynamics. Small values of τ (frequent collisions) yield rapid thermalization but may disrupt dynamical correlations. Whereas larger τ values conserve trajectories better but require longer equilibrium times.

The Andersen thermostat is a widely used choice for molecular dynamics simulations due to its straightforward implementation and accurate sampling of the canonical ensemble [43]. However, its stochastic velocity reassignment can disrupt dynamical correlations. Transport properties may be suppressed because velocities are reset randomly. This limitation could be particularly inconvenient for aggregation kinetics, where particles approach each other gradually before forming larger clusters. In such cases, a sudden velocity reassignment may redirect a particle away from the interaction partner, thereby interrupting the natural aggregation process and modifying the underlying dynamics.

7.4. Simulation Model

In the model, particles are represented as clusters with a predefined fixed radius. Aggregation occurs when the centre-to-centre interaction potential between two clusters reaches the primary minimum of the DLVO curve. The total interaction potential of a cluster is obtained by superimposing the DLVO potentials of the individual particles that form the cluster. This modelling choice requires minimal bookkeeping during aggregation and is straightforward to implement.

However, this representation introduces two deviations from physical behaviour. First, the superposition of multiple pairwise potentials amplifies both attractive and repulsive interactions. As a result, the energy barrier and the depths of the primary and secondary minima no longer correspond to theoretical DLVO predictions, and the aggregation behaviour becomes artificially strengthened. Second, the predefined cluster radius does not reflect the actual size of a growing aggregate. If realistic radii are used, particles located near the surface of a composite cluster may lie outside the repulsive barrier, preventing further aggregation. To prevent premature termination of aggregation, clusters in the model are assigned smaller radii. This ensures that the primary minimum remains dominant over the repulsive barrier, but it also means that the final aggregate size is not physically meaningful.

The model therefore enables efficient simulation of aggregation trends but does not preserve a physical correspondence between cluster size, interaction potential and geometric configuration.

The simulation is performed in non-dimensional units. Using reduced units minimises rounding errors during integration. The non-dimensionalisation applied in this research is summarised in Table 7.3.

Table 7.3: Reduced unit system for MD simulations.

Physical quantity	Symbol	Scaling constant	Reduced form
Length	r	σ	$r^* = \frac{r}{\sigma}$
Energy	U	$k_B T_0$	$U^* = \frac{U}{k_B T_0}$
Mass	m	m_0	$m^* = \frac{m}{m_0}$
Temperature	T	T_0	$T^* = \frac{T}{T_0}$
Time	t	$\sqrt{m_0 \sigma^2 / k_B T_0}$	$t^* = \frac{t}{\sqrt{m_0 \sigma^2 / k_B T_0}}$
Density	ρ	σ^{-3}	$\rho^* = \rho \sigma^3$

Model Flow Chart

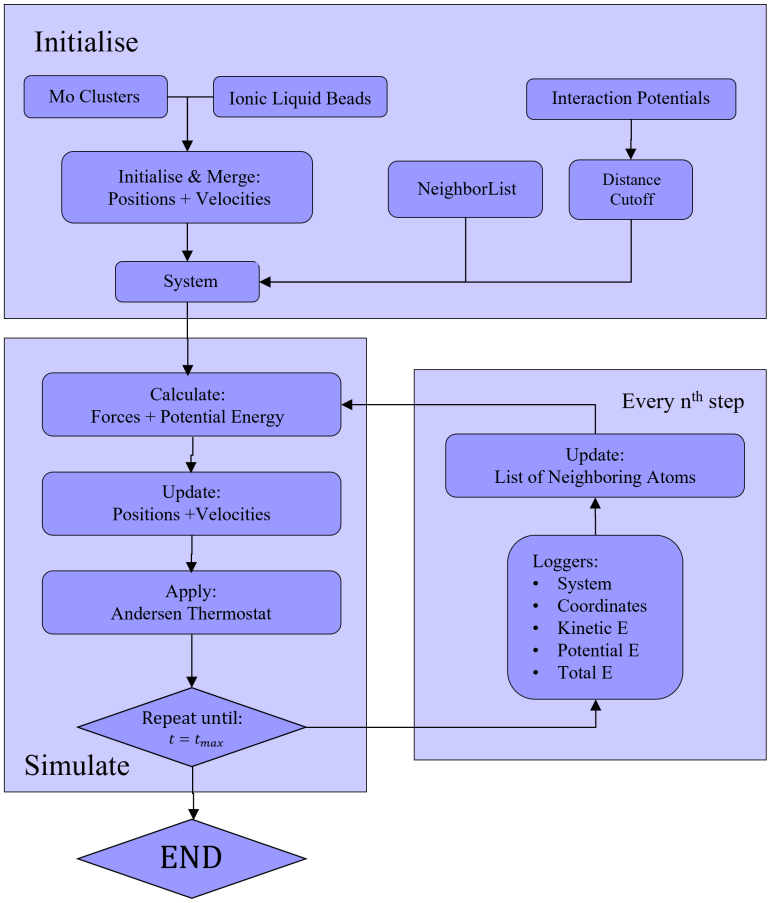

Figure 7.1: Flowchart of the molecular dynamics aggregation simulation, showing initialization, force evaluation, integration, thermostat coupling, neighbor list update, and logging.

7.5. Post-Processing Analysis

To effectively post-process the data and obtain insight into the dynamics of the simulation, it is essential that the relevant quantities are stored during runtime. This is achieved through a set of predefined loggers that record specific properties of the system at selected time intervals. These loggers, listed in Table 7.4, provide the foundation for subsequent analyses, such as energy conservation and cluster growth evaluation.

Table 7.4: Overview of the predefined loggers used during the simulations and the corresponding recorded quantities.

Logger	Recorded Quantity
System	Static properties of all atoms, including identifiers, types, and attributes
Coordinates	Position vectors of all particles at each sampled step
Kinetic energy	Instantaneous kinetic energy of the system
Potential energy	Interaction energy derived from the DLVO potential
Total energy	Sum of kinetic and potential energy at each sampled step

Each simulation typically consists of several thousand integration steps. Storing the full dataset for every step would be computationally expensive and, in most cases, unnecessary. Therefore, a sampling scale n is introduced, which determines that the predefined quantities are recorded every n^{th} simulation step. This approach significantly reduces storage requirements while retaining sufficient temporal resolution to analyze the relevant physical processes.

Average Cluster Size

To quantify the aggregation dynamics, the average nanoparticle size was evaluated as a function of time. A nanoparticle is defined as a set of molybdenum clusters that are within a cutoff distance and are connected through at least one neighboring atom. It can occur the two clusters are in the same nanoparticle while the distance between the cluster is larger than the cutoff distance. These clusters are connected by at least one cluster.

For each recorded frame t, the size of every cluster $n_i(t)$ was determined, and the average cluster size is computed as

$$\langle N(t) \rangle = \frac{1}{N_c(t)} \sum_{i=1}^{N_c(t)} n_i(t), \tag{7.6}$$

where $N_c(t)$ denotes the total number of clusters at time t. $\langle N(t) \rangle$ denotes the average amount of atoms in a cluster. The resulting time-dependent average $\langle N(t) \rangle$ provides a direct measure of the aggregation rate.

Cluster Growth Function

To provide a more intuitive representation of cluster growth, the number of atoms in a cluster is converted to an equivalent cluster radius. This radius is obtained by dividing the total atoms by to the two-dimensional area density of molybdenum. The equation is taken from Table 7.1 ($R = \sqrt{N/\pi n_{2D}}$). Due to the finite dimensions of the system, the clusters grow until they reach a steady-state configuration, or alternatively, merge into a single large aggregate. In both cases, the cluster size will reach an equilibrium for long simulation times. Therefore, the time evolution of the average cluster size is expected to follow an exponential trend approaching an asymptote. The rate at which this curve rises provides insight into the aggregation kinetics of the system.

To describe this behavior, the following expression is fitted to the simulation data:

$$R_{\text{avg}}(t) = R_\infty - k\, e^{-\frac{t}{t_{agg}}}, \tag{7.7}$$

where the parameters R_∞, k, and t_{agg} are determined by a least-squares fit. The parameter t_{agg} represents the characteristic time for the system to reach its equilibrium. r_∞ denotes the steady-state average cluster radius reached for $t \to \infty$. The amplitude k defines the difference between the initial and final cluster radii. At $t = 0$, the average cluster radius is therefore given by

$$R_{\text{avg}}(t = 0) = R_\infty - k = R_{\text{init}}, \tag{7.8}$$

where R_{init} corresponds to the initialisation radius of the clusters. Figure 7.2 gives a schematic representation for different characteristic times t_{agg}.

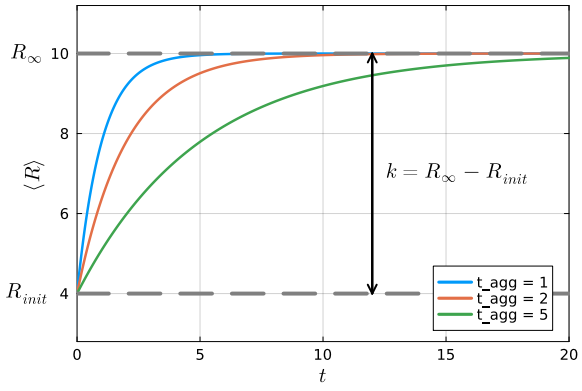

Figure 7.2: Illustration of the exponential cluster growth model showing the evolution of the average cluster radius $\langle R \rangle$ toward its steady-state value R_∞ for different aggregation rates t_{agg}. The amplitude $k = R_\infty - R_{\text{init}}$ represents the total growth in average cluster size.

Overfitting

Having three adjustable parameters in the fitting model increases the risk of overfitting. To minimize this effect, the value of R_∞ was fixed to the average cluster size at the end of the simulation, while the initial cluster size

R_{init} was directly obtained from the first simulation frame. The prefactor k was consequently defined as $k = R_\infty - R_{init}$, leaving the aggregation rate t_{agg} as the only free fitting parameter. Appendix C.1 compares two fits: one using all three parameters as adjustable variables and one where only t_{agg} is fitted. Although the simplified model provides a slightly less accurate fit, it avoids overfitting and ensures that the extracted parameters remain physically meaningful.

Statistical Analysis

To quantify the variability in aggregation behaviour, each unique combination of B'/D' and C'/D' was simulated n times under identical conditions but different position and velocity initialisations. For every simulation, the time evolution of the average radius was fitted to the exponential model described in Section 7.5, yielding independent estimates for the characteristic aggregation time t_{agg} and the steady-state cluster radius R_∞. To gain insight in the mean and the spread of these values, the mean, standard deviation and the coefficient of variation are introduced. For each parameter pair, the mean value $\mu(x)$ and the standard deviation $\sigma_{std}(x)$ of a stochastic variable (x) were determined across the n repetitions:

$$\mu(x) = \frac{1}{n}\sum_{i=1}^{n} x_i, \qquad \sigma_{std}(x) = \sqrt{\frac{1}{n-1}\sum_{i=1}^{n}(x_i - \bar{x})^2}, \tag{7.9}$$

where x_i denotes the fitted value (either $t_{\text{agg},i}$ or $R_{\infty,i}$) obtained from simulation i. The standard deviation is indicated by its subscript std, to avoid confusion with the similar collision parameter σ. The mean represents the expected value of the stochastic variable, while the standard deviation quantifies the variability or the spread of the variable.

The coefficient of variation is used to compare the standard deviation of multiple datasets with their own probability densities. It is defined as

$$CV(x) = \frac{\sigma_{std}(x)}{\mu(x)}. \tag{7.10}$$

The coefficient of variation non-dimensionalises the dispersion, allowing distributions with different magnitudes to be compared directly. Low values ($CV < 0.1$) indicate that the data show little variability, whereas $CV > 0.5$ reflects large fluctuations relative to the mean. The CV is able to capture the relative dispersion of datasets with different units or vastly different means.

8

Results

This chapter presents the results of the coarse-grained simulations. Section 8.1 validates the simulation setup. Section 8.2 evaluates the performed parameter sweep of dimensionless coefficients. Relating the framework to aggregation kinetics, specifically aggregation time and final cluster size. Finally, the chapter concludes with an assessment of the variability in the results to evaluate the consistency of the simulations.

8.1. Model Validation

Validation of the simulation approach starts with the `Molly.jl` package. It is benchmarked using an argon gas system to verify the numerical integration and interaction forces. The benchmark behaves as expected, and the results are presented in Appendix D.

Next, a CG simulation is performed to verify the following aspects: that the molybdenum clusters interact according to the DLVO potential, and that the thermostat correctly controls the simulation temperature. A smaller simulation domain is used to improve visual clarity.

Molybdenum clusters with a radius of 1 nm are placed in a two-dimensional domain. From Table 7.1, a cluster of this size contains approximately 50 atoms, corresponding to a total mass of $m_{\text{Mo}} = 7.97 \times 10^{-24}$ kg. This mass is assigned as the reference mass m_0. To preserve the physical density of the molten salt, each ionic liquid bead is assigned a mass of $m_{\text{bead}} = 1.14 \times 10^{-24}$ kg.

The coarse-grained Lennard–Jones parameters ε_{cg} and σ_{cg} are selected based on the radial distribution functions for different ε_{cg}. The value with the radial distribution function most corresponding of a liquid is chosen. The parameters used in this validation simulation are summarised in Table 8.1.

Table 8.1: Simulation parameters for the two-dimensional molybdenum cluster aggregation at $T_0 = 773$ K.

Variables	Description	Value	Unit
B'/D'	Size of EDL	10^{-7}	-
C'/D'	Strength of EDL	4	-
D'	DLVO scaling constant	1	-
T_0	Temperature	773	K
m_{Mo}	Mass of a single molybdenum cluster	$7.97 \cdot 10^{-24}$	kg
m_{bead}	Mass of a ionic liquid bead	$1.14 \cdot 10^{-24}$	kg
N_{Mo}	Number of Mo clusters	30	-
N_{beads}	Number of ionic beads	69	-
ε_{cg}	Interaction strength	$1.26 \cdot 10^{-20}$	J
σ_{cg}	Effective bead-bead interaction	$0.4 \cdot 10^{-9}$	m
L_x, L_y	Dimensions	$7 \cdot 10^{-9}$	m

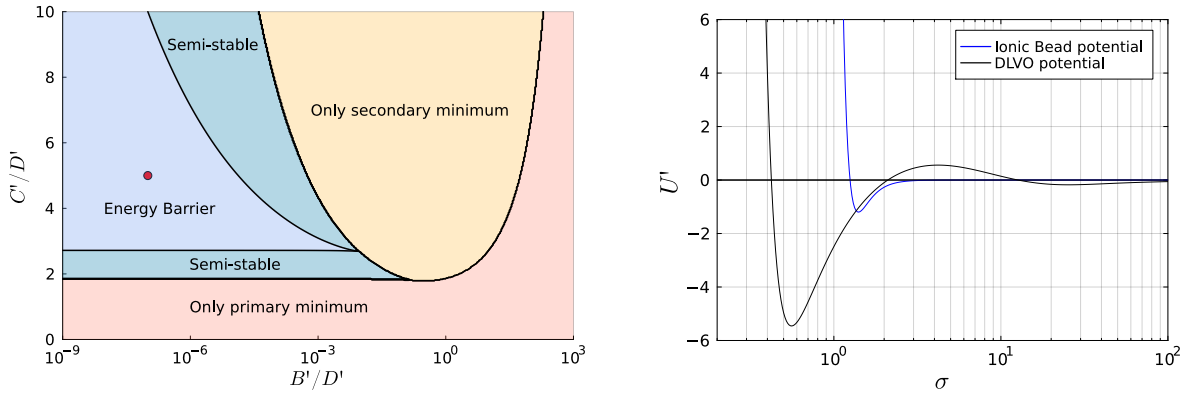

Figure 8.1: Stability map of the normalized DLVO potential. (Left) Regimes of primary and secondary minima as a function of the non-dimensional parameters B'/D' and C'/D', indicating semi-stable and unstable regions. The red marker denotes the parameter combination used in the simulation. (Right) Corresponding normalized DLVO potential U' as a function of the dimensionless separation distance σ, showing both primary and secondary minima.

Figure 8.1 shows the dimensionless coefficients used in the first simulation. The left figure highlights the selected values of B'/D' and C'/D', which correspond to the parameter set in Table 8.1. The right figure displays the resulting DLVO potential. It shows both a primary and a secondary minimum, located at approximately $r \approx 0.58\sigma$ and $r \approx 22\sigma$, respectively. Both minima are expected to be observable in the simulation.

Figure 8.2 shows a snapshot of the simulation. The molybdenum clusters are coloured purple, while the molten salt beads are coloured green. After reaching a stable configuration, most clusters have merged into larger aggregates. These aggregates are hereafter referred to as nanoparticles (NPs) to distinguish them from the initial individual clusters. The resulting structure matches the predicted DLVO interaction: within each NP, clusters are separated by approximately $r \approx 0.6\sigma$, while the spacing between NPs is much larger. Based on Figure 8.2, this spacing is roughly $r \approx 10\sigma$, which is shorter than the potential prediction. This deviation is caused by the periodic boundary conditions, where the NPs interact across the domain boundaries and are effectively pushed closer together.

Figure 8.3 shows the evolution of the kinetic, potential and total energy during the simulation. The kinetic energy converges towards the theoretical value $\langle K \rangle = Nk_BT$, consistent with statistical mechanics. The potential energy decreases as the system relaxes toward equilibrium. This confirms that the Andersen thermostat maintains the desired temperature throughout the simulation.

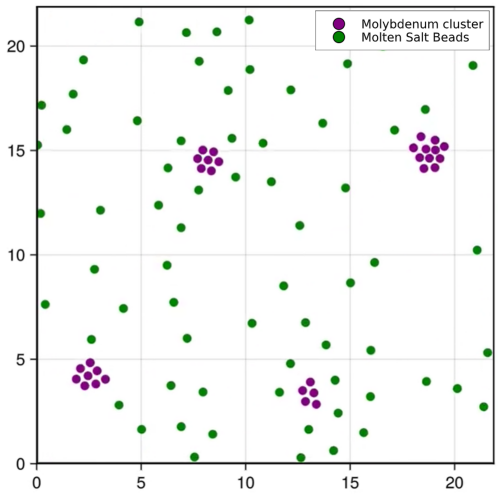

Figure 8.2: Snapshot of the simulated two-dimensional molybdenum cluster in molten salt.

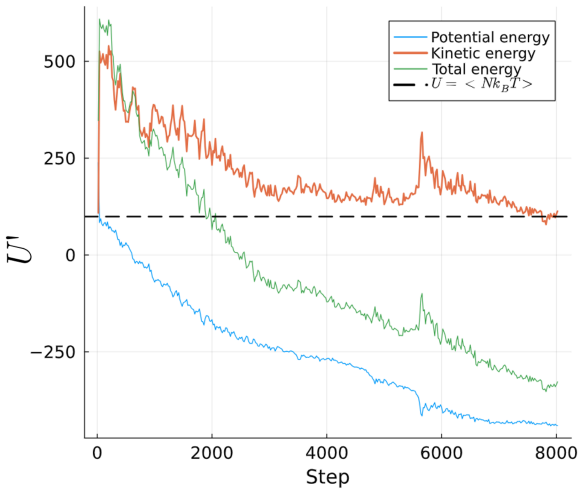

Figure 8.3: Evolution of the potential, kinetic, and total energy, confirming proper temperature control by the Andersen thermostat.

8.2. Parameter Sweep

To investigate the influence of the dimensionless coefficients B'/D' and C'/D' on aggregation behaviour and NPgrowth, coarse-grained molecular dynamics simulations are performed for different combinations of the dimensionless coefficients. The selected values are presented in Table 8.2.

Table 8.2: Simulated values of the non-dimensional DLVO coefficients.

Dimensionless coefficient	**Values used in simulations**					
B'/D'	$[10^{-9},$	$10^{-7},$	$10^{-5},$	$10^{-3},$	$10^{-1},$	$10]$
C'/D'	$[0,$	$2,$	$4,$	$6,$	$8,$	$10]$

The selected combinations of B'/D' and C'/D' span the relevant regimes identified in Chapter 4. Parameter pairs that fall inside the "Only secondary minimum" region were intentionally excluded. In this regime, particles remain trapped in the secondary minimum and no aggregation behaviour is expected. Therefor, no characteristic aggregation time can be observed. Omitting these cases also reduces the total required simulation time.

All simulations were performed in a two-dimensional system under identical thermodynamic conditions. Only the size of the system is changed. These changed vairables are listed in Table 8.3. Each parameter configuration was repeated ten times to obtain statistically reliable averages.

Table 8.3: Simulation parameters for the two-dimensional molybdenum cluster aggregation at $T_0 = 773$ K.

Variables	**Description**	**Value**	**Unit**
N_{Mo}	Number of Mo clusters	210	-
N_{beads}	Number of ionic beads	700	-
L_x, L_y	Dimensions	$20 \cdot 10^{-9}$	m

From these simulations, the influence of B'/D' and C'/D' on aggregation behaviour is quantified by tracking the time evolution of the NPradius. The resulting growth curves are analysed in post-processing and fitted using the exponential growth model introduced in Section 7.5. For each unique parameter combination, four quantities are extracted: the aggregation time and the final NP radius, together with their corresponding coefficient of variances. These quantities are visualised to reveal the dependence and robustness of aggregation time and final particle size on the dimensionless DLVO coefficients.

Part of the results of the parameter sweep are shown in Figure 8.4. Each subplot displays the time evolution of the average NP radius for one value of B'/D' and different values of C'/D'. Every coloured line corresponds to an individual simulation, whereas the black dots represents the mean over ten repetitions. An exponential growth behaviour is observed, after which the average radius reaches a steady value. In some runs, the simulation terminates prematurely. This occurs most often at the beginning of the simulation and is independent of the chosen timestep, suggesting that the initialisation is the cause for the diverging energies.

Figure 8.5 summarises the resulting steady-state cluster radius for all simulated parameter combinations. Two trends emerge clearly. First, increasing C'/D' leads to a reduction in the final cluster size. Since C'/D' expresses the relative strength of EDL, it follows that higher values suppress aggregation and limit cluster growth. Second, increasing B'/D' also decreases the final radius. This is remarkable as higher B'/D' corresponds to a shorter Debye length, reducing the range of electrostatic repulsion. So it could be expected that a shorter EDL promotes the aggregation. However, increasing the value of B'/D' also corresponds to weakening the depth of the primary minimum, as shown earlier in Figure 5.4. Consequently, aggregation becomes less favourable and smaller final clusters are obtained. The standard deviation of the final cluster size is indicated by the error-bars and shows an expected trend. The standard deviation reduces as the final cluster size is reduced as well.

In summary, the largest clusters form in the regime where the DLVO potential contains only a primary minimum (low B'/D' and low C'/D'), whereas increasing either parameter reduces the final cluster radius.

Figure 8.6 presents the aggregation time for all simulated combinations of the dimensionless coefficients. The simulation did not converge for $(B'/D',\ C'/D') = (10^{-7},\ 8)$, and the case $(10^{-5},\ 8)$ resulted in an aggregation time exceeding the plotted axis range (above 10^3), and was therefore omitted for clarity.

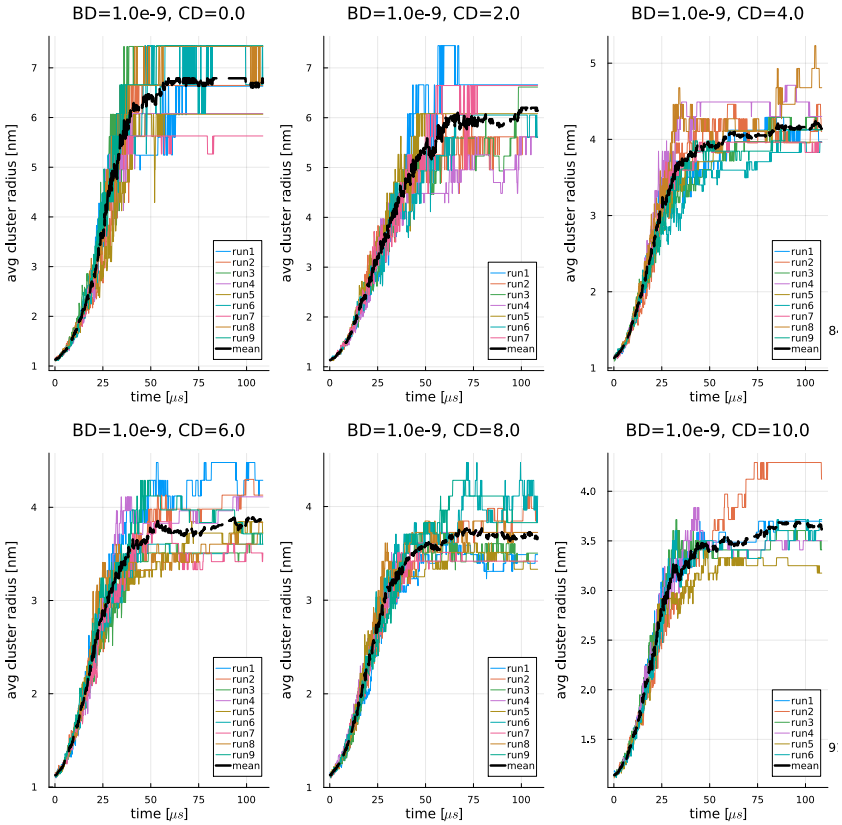

Figure 8.4: Evolution of the average NPradius over time for the coefficient set $B'/D' = 10^{-9}$ and varying values of $C'/D' \in [0, 2, 4, 6, 8, 10]$. Each coloured trace represents an independent simulation run, while the black dots indicates the mean radius across ten repetitions. Increasing C'/D' increases the electric repulsion, slowing down the aggregation.

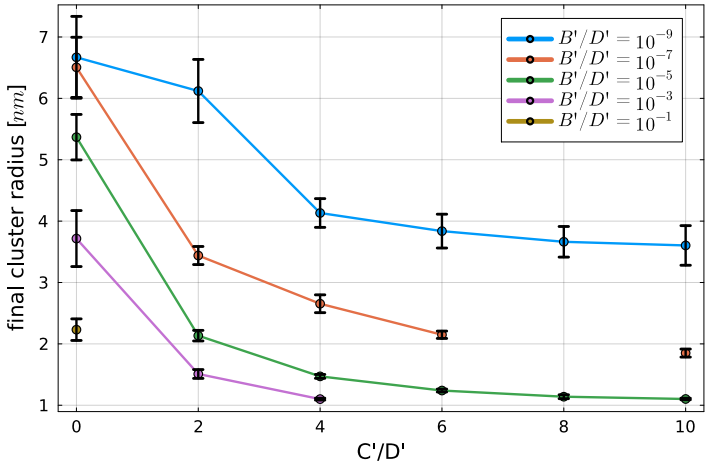

Figure 8.5: Final cluster radius as a function of C'/D' and for different values of B'/D'. Error bars represent the standard deviation. There are missing values for the combination $(B'/D', C'/D') = (10^{-7}, 8)$

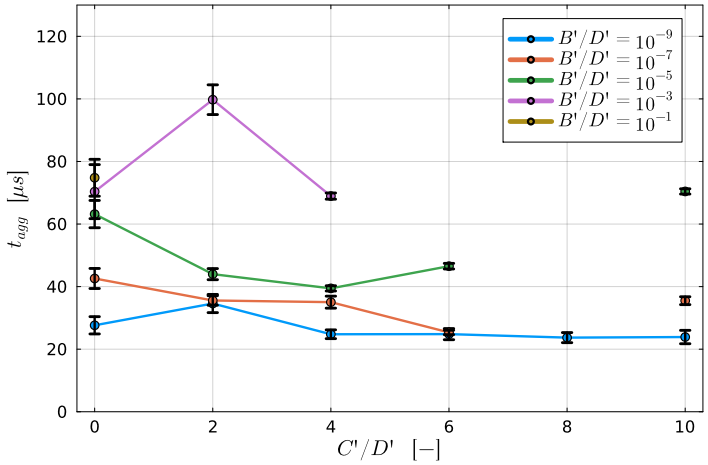

Figure 8.6: Aggregation time as a function of C'/D' and for different values of B'/D'. Error bars represent the standard deviation. There are missing values for the combinations $(B'/D', C'/D') = (10^{-7}, 8)$ & $(10^{-5}, 8)$

The results show that variations in C'/D' have only a minor influence on the aggregation time. In contrast, increasing B'/D' consistently leads to longer aggregation times. Since B'/D' reflects the relative thickness of the Debye layer (shorter Debye length at higher B'/D'), higher values also reduce the depth of the primary minimum and decrease the overall magnitude of the interaction potential between the molybdenum cluster. As a result, the driving force for aggregation is weakened, slowing down the rate at which the system reaches its equilibrium cluster size. Thus, larger B'/D' values correspond to slower aggregation kinetics and longer relaxation times.

The objective of the simulations was to quantify how the dimensionless coefficients B'/D' and C'/D' influence the aggregation kinetics. To complement the time–series results, the aggregation time (t_{agg}), final cluster radius, and their corresponding coefficients of variation (CV) are visualised as a heatmap with the same axis as the region maps from Chapter 5. These results are presented in Figures 8.7–8.10. In these figures, missing data points are shown in grey.

Figure 8.9 shows that combinations of B'/D' and C'/D' located within or near or in the *semi-stable* region (where a stable secondary minimum is expected) result in a final cluster size of approximately one particle, $R_\infty = 1$. This indicates that no aggregation occurs, consistent with the predicted behaviour of a stable suspension.

Figures 8.8 and 8.10 present the coefficient of variation (CV) for t_{agg} and the final cluster radius, respectively. The CV normalises the variance by the mean of each distribution, allowing comparison between simulations with different absolute scales. For the majority of the parameter space, the CV remains low ($\text{CV} < 0.2$), indicating that the aggregation behaviour is reproducible and even predictable. Higher values of $\text{CV}(t_{\text{agg}})$ occur only near the transition to the "Only secondary minimum" regime. In these cases, the initial cluster size is already close to the equilibrium size, producing nearly flat curves. The exponential fit used to extract t_{agg} becomes ill-defined, resulting in unstable fitted values and an high CV.

Remarks

The simulations demonstrate a quantitative relation between the non-dimensional DLVO coefficients and the aggregation kinetics in colloidal systems. However, some considerations are necessary when interpreting these results.

Each parameter combination was simulated ten times to extract general trends and quantify variability. On average, approximately 25% of the runs were not completed due to diverging energies during the first timesteps. This is likely caused by unfavourable particle placement at initialisation, generating excessively large forces. As a result, the mean and standard deviation are based on roughly 7-8 successful repetitions per parameter set, which may reduce the statistical robustness of the reported averages.

Furthermore, all simulations were performed using a fixed value of the coefficient D'. In practise, however, D' is not independent of the ratio B'/D'. Using the expressions

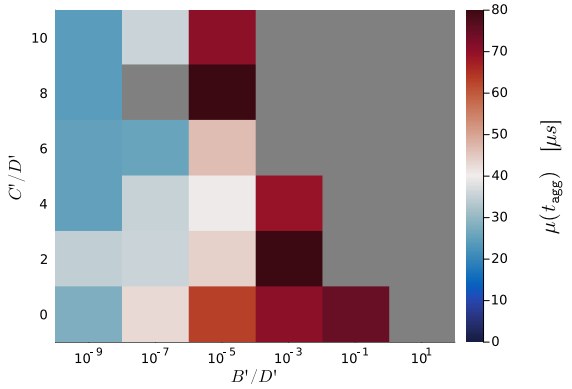

Figure 8.7: Mean aggregation time as a function of the dimensionless coefficients B'/D' and C'/D'. Each cell represents the average aggregation time over multiple independent simulations. Grey cells indicate missing or insufficient data.

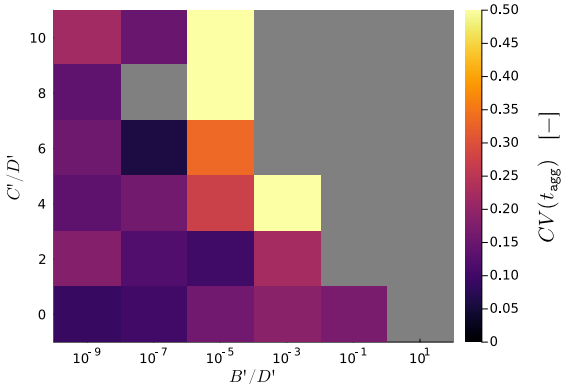

Figure 8.8: Coefficient of variation of the aggregation time, for each combination of the dimensionless coefficients B'/D' and C'/D'.

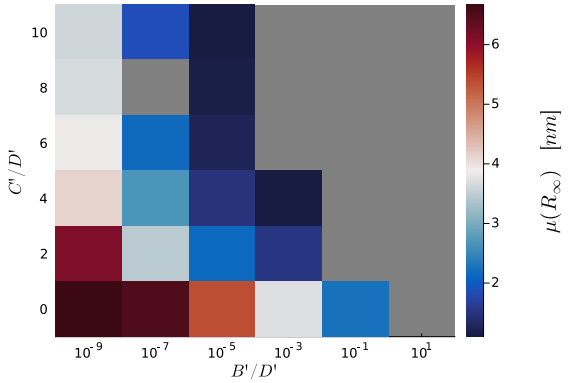

Figure 8.9: Mean final cluster radius as a function of the dimensionless coefficients B'/D' and C'/D'. Each cell represents the average aggregation time over multiple independent simulations.

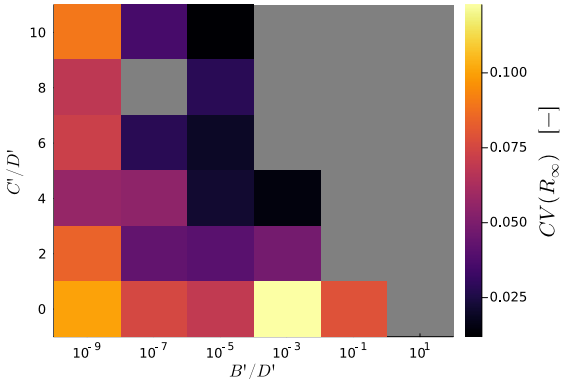

Figure 8.10: Coefficient of variation of the final cluster radius, for each combination of the dimensionless coefficients B'/D' and C'/D'.

$$D' = \frac{1}{6}\kappa\frac{A}{k_BT}\frac{a_1a_2}{a_1+a_2}, \qquad \text{and} \qquad \frac{B'}{D'} = \frac{1}{210}(\sigma\kappa)^6, \tag{8.1}$$

it follows that

$$D' = \frac{1}{6\sigma}\left(210\frac{B'}{D'}\right)^{1/6}\frac{A}{k_BT}\frac{a_1a_2}{a_1+a_2}, \tag{8.2}$$

concluding that D' increases with increasing B'/D'. In the simulations presented in this work, D' was intentionally kept constant to isolate the effect of the dimensionless coefficients. This simplification introduces an reduction in amplitude of the DLVO potential for high values of B'/D. Figure 8.11 illustrates this behaviour. For a fixed value of $C'/D' = 8$, the potentials associated with low B'/D' (black) exhibit a deeper primary minimum, whereas the potentials at high B'/D' (red) are considerably weakened. This reduction in amplitude is consistent with the longer aggregation times observed in Figure 8.7.

Figure 8.12 shows the DLVO potential when D' is recalculated for each value of B'/D' according to Equation 8.2. In this case, the potentials remain of comparable magnitude and follow the expected van der Waals attraction. For large B'/D', the resulting curve approaches a Lennard-Jones shaped potential again, consistent with systems where the Debye length is short and earlier claims. This behaviour confirms that short electrostatic screening lengths inherently promote aggregation. It is highly advised to implement Equation 8.2 in the simulations to see the effect on the characterstic aggregation time.

Additionally, the exponential function used to extract the aggregation time may not be the optimal representation for all parameter combinations. Figure 8.13 shows that for low values of B'/D' the radius growth curve follows

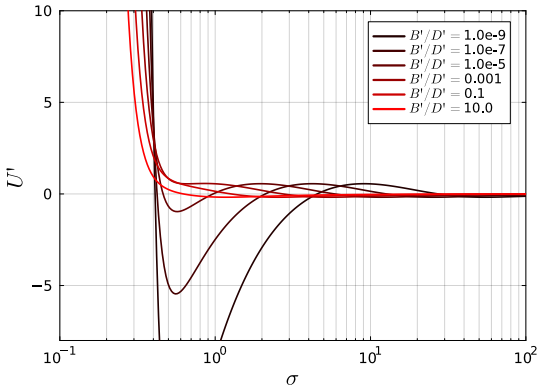

Figure 8.11: DLVO potential for different values of B'/D'. The values for $C'/D' = 8$ and $D' = 1$ are held constant. A descrease in amplitude can be seen for rising values of B'/D'.

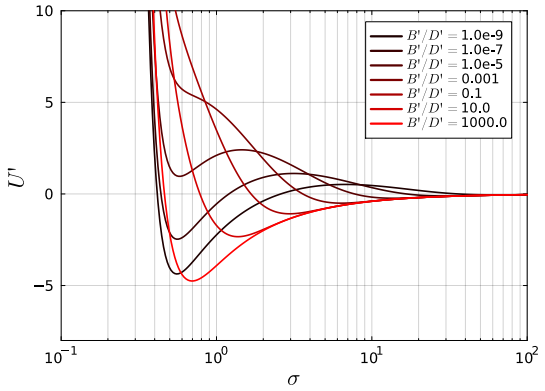

Figure 8.12: DLVO potential for different values of B'/D'. The value for $C'/D' = 8$ is held constant. κ changes with parameter B'/D' followig Equation (8.2).

an exponential trend, whereas for larger B'/D' the behaviour becomes increasingly linear. In such cases, either a stretched exponential or a linear model may provide a more accurate representation of the aggregation dynamics.

8.2.1. Application to MSRs

With several assumptions, the ratio B'/D' can be estimated for the MSR case study. The required inputs are the ionic strength, the operating temperature range, and the dielectric permittivity.

The molten salt used in this work is the eutectic LiCl–KCl mixture. Based on its composition, the ionic strength is calculated as $I = 13.29\ \text{mol}\,\text{L}^{-1}$. The full derivation is provided in Appendix A. The dielectric permittivity of molten salts is less well defined. Solid alkali chlorides typically exhibit values near $\varepsilon = 10$, while molten salts can have much lower values due to reduced ion polarizability. Reported values include $\varepsilon \approx 2$. In this work, a representative intermediate value of $\varepsilon = 5$ is used [21].

Using these material parameters and a realistic MSR operating range, from the eutectic melting point $T_{\text{melt}} = 626$ K to an upper bound of $T_{\text{upper}} = 1373$ K, the resulting dimensionless ratios fall within

$$\frac{B'}{D'} \in (2.43 \cdot 10^{9},\ 25.6 \cdot 10^{9}). \tag{8.3}$$

These values lie deep within the primary minimum regime, where irreversible aggregation occurs. In this regime, Figure 8.12 shows that the DLVO potential reduces to a shape comparable to a Lennard-Jones potential. The simulations confirm that in this regime aggregation always occurs. However, the aggregation time depends on the magnitude of the attractive potential, which is captured in the coefficient D'. This work can estimate certain aggregation times based on this coefficient. However, additional simulations should be computed mimicking the molybdenum concentration in the MSR. To make a valid prediction on aggregation rates in a MSR, first the dependency on the concentration should be explored.

However, using this research, several conclusions can also be drawn for the case of a MSR. Due to the position of the MSR deep in the primary minimum regime, it can be concluded that the surface charge present on particles is insufficient to create an energy barrier. This also implies that the specific molten salt composition has limited influence on aggregation behaviour. Changes in ion polarizability (the Hofmeister effect) affect aggregation only near the energy-barrier regime, which is not the case here. Therefore, future modelling can represent the interaction using a classical Lennard–Jones potential without loss of physical relevance.

A more promising research direction is the application of these results to sedimentation control. The sphere–plate potential could be used to estimate the required separation distance for NP deposition on reactor surfaces. Non-DLVO forces may strengthen or weaken particle attachment depending on location. For example, heat exchanger surfaces could be coated to introduce short-range repulsion to prevent deposition, while non-critical surfaces could be engineered to promote sedimentation.

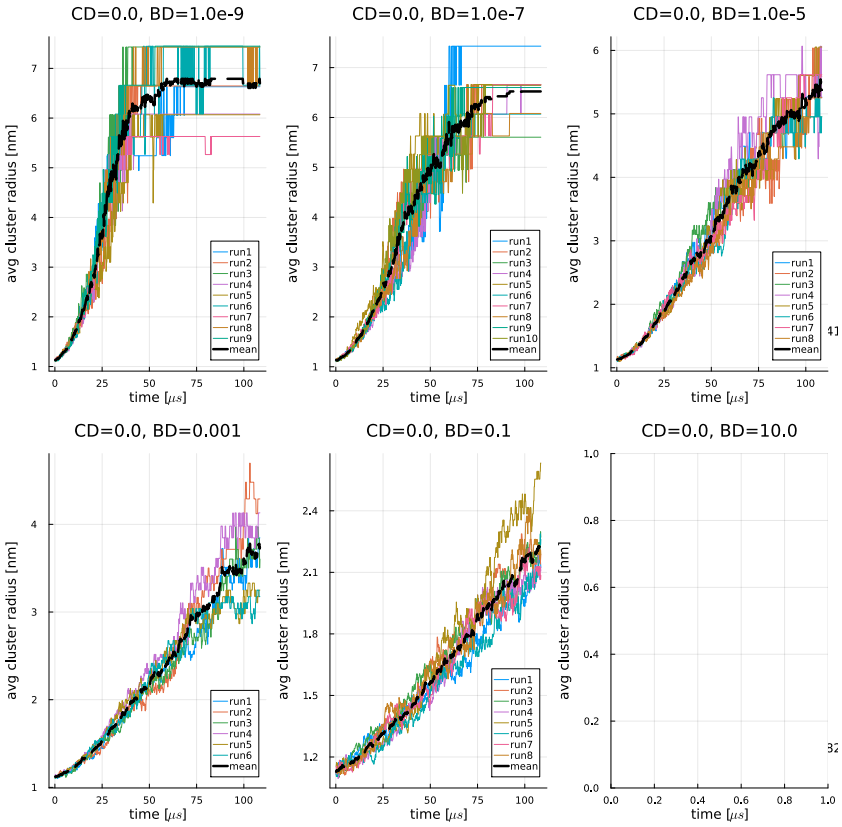

Figure 8.13: Evolution of the average NPradius over time for the coefficient set $C'/D' = 0$ and varying values of B'/D'. Each coloured trace represents an independent simulation run, while the black dots indicates the mean radius across ten repetitions. Increasing C'/D' increases the electric repulsion, slowing down the aggregation.

Another possible mitigation strategy is to increase the surface potential on critical reactor components. Higher surface potentials can induce structured ionic layers that resist NP approach, acting as an additional repulsive barrier. However, secondary effects must be considered. Enhanced surface potential may influence corrosion behaviour or alter heat transfer efficiency.

9

Discussion

This study explored the application of DLVO theory to describe colloidal aggregation through a new non-dimensional framework. The resulting formulation expresses the aggregation behaviour as a function of two parameters, B'/D' and C'/D', which represent the strength and the size of the EDL compared to the van der Waals attraction. Although this framework has not yet been developed for the full range of the sphere-sphere interaction, this has been accomplished that for the sphere-plate interaction. The simulation still contains many assumptions and simplifications and has been done in 2 dimensions. However, a first qualitative relation between aggregation speed and the dimensionless framework has been established.

For clarity, this discussion first evaluates the performance and assumptions of the non-dimensional DLVO framework, followed by an assessment of the coarse-grained simulation results. Each part interprets the results, identifies improvements and relates them to literature. The chapter concludes with an outlook on potential directions for future work.

9.1. Analytical Model and Non-Dimensionalisation

The near-field approximation applied to the sphere–sphere interaction served as an initial step to visualise the DLVO stability regions. However, this approximation fixes the regime boundaries and makes them independent of particle size, which is not physically realistic. The sphere–plate interaction, where the full interaction range is considered, shows that regime boundaries shift with particle radius: when a particle grows, the electric double layer becomes relatively thinner, causing a stronger net attraction and promoting aggregation. This behaviour is expected to occur in the full sphere–sphere formulation as well. A complete treatment of the sphere–sphere potential is therefore required to accurately describe aggregation kinetics

The current framework captures the dominant DLVO contributions, but non-DLVO interactions such as hydration forces, ion correlations, and specific adsorption may significantly modify colloidal stability [51]. The model is therefore limited to systems in which such forces are not present; which we refer to as *simple colloidal systems*.

Finally, several parameters within the DLVO formulation are difficult to determine experimentally. The Hamaker constant is often only known within an order of magnitude, and surface potentials γ_1 and γ_2 are rarely measured directly. The linear superposition approximation used to describe the double-layer repulsion introduces additional simplifications. A more detailed investigation of NP surface chemistry and charging behaviour is therefore essential to further improve accuracy and predictive capability.

9.2. Coarse-Grained Simulations

The ionic liquid was modelled as a coarse-grained Lennard-Jones fluid. This approach significantly reduces computational cost by treating the beads as electrically neutral particles, thereby omitting explicit charge interactions. This assumption might oversimplify the system by neglecting important ion-ion correlations that influence the structure and dynamics of molten salts. A more realistic coarse-grained model would assign bead types based on individual ions, preserving their electrostatic interactions while still reducing the degrees of freedom. This approach would better capture ion structuring, but introduces increased complexity in model calibration and pa-

rameter fitting.

In addition, the calibration of the coarse-grained parameters can be improved. In the current model, the parametrisation is based only on reproducing the experimental density at a single temperature and on matching radial distribution functions. Including additional thermodynamic and transport properties would increase the validity of the parameters.

A two-dimensional simulation framework was developed to apply the non-dimensional DLVO parameters directly. In this framework, the interaction potential was evaluated between the centres of mass of the clusters, and beads did not merge upon contact. Instead, atoms retained their individual pairwise interactions, resulting in a superposition of forces. The superposition most likely exaggerated the aggregation kinetics of the system. Resulting in accelerated aggregation and high energy barriers. Another limitation of this model is that the cluster cannot be simulated with a radius larger than the collision length. Beyond this point, the predicted energy barrier may occur at the cluster boundary, causing an artificially stable dispersion even when the DLVO potential suggests aggregation.

The thermostat choice also influences the aggregation kinetics. The Andersen thermostat correctly samples the canonical ensemble by randomly reassigning particle velocities from the Maxwell–Boltzmann distribution. However, these stochastic collisions break velocity autocorrelation and distort dynamic properties such as diffusion [63]. Since NP aggregation is driven by diffusion-controlled encounters, a thermostat that preserves physical dynamics (e.g., Nosé–Hoover or Langevin) would be preferable in future work.

Despite these challenges, the model provides a first quantitative relation of the aggregation behaviour. Simulations were performed across a range of parameter combinations of B'/D' and C'/D'. For each case, the average cluster size was computed over time and fitted to an exponential function with an asymptotic limit. The resulting characteristic aggregation times and steady-state cluster sizes show clear agreement with theoretical predictions: lower B'/D' values lead to faster aggregation, while higher C'/D' values result in smaller final clusters due to stronger electrostatic repulsion. However, some simulations showed a linear growth instead of an exponential growth. It should be investigated that certain regions need linear fit or just an extended exponential.

Finally, the aggregation dynamics were studied within a finite simulation domain. In such a closed system, the aggregation process eventually reaches a state where all particles coalesce into a single large NP. This represents a numerical equilibrium rather than a physical steady state, as the system no longer reflects the continuous production and removal of particles that would occur in a realistic environment. A simulation setup that more closely resembles the conditions of a molten salt reactor (MSR) would be highly valuable in this context. Such a model could incorporate a source term to introduce metal particles, representing fission products, and a sink term to account for NP removal through sedimentation at the boundaries. Developing a simulation framework that integrates both effects, however, presents significant methodological challenges. For this reason, it is particularly important to assess the influence of the system size on the observed aggregation behaviour to ensure that the finite domain does not constrain the results.

9.3. Recommendation for Future Research

This section is divided in a section for the non-dimensionalisation and for the simulations. Lastly, specific recommendation for research of aggregation in MSR will be given.

Non-Dimensionalisation

As mentioned, it is recommended to derive sphere-sphere interaction potential without relying on the near-field approximation. In that case, both particle radii are expected to appear explicitly in the dimensionless coefficients B'/D' and C'/D'. In addition, the framework should be experimentally validated. Controlled measurements of sphere-plate or plate-plate (near-field sphere-sphere) interactions could confirm whether the predicted DLVO regimes (primary minimum, energy barrier, secondary minimum) occur as expected. Such experiments require systems in which the coefficients B'/D' and C'/D' can be varied independently and with high precision, for example by adjusting ionic strength, surface charge, or particle size.

Coarse-Grained Simulations

It is advised to further develop the coarse-grained (CG) model. The current implementation uses a centre-to-centre distance, whereas the DLVO formulation is defined on a surface-to-surface separation. Introducing a surface-based distance, combined with a merging function for neighbouring clusters, would eliminate the superposition

effect of potentials. Additionally, the dependency of the coefficient D' on the ratio B'/D' should be modelled explicitly. Together, these improvements would strengthen the link between the CG simulation and the predicted aggregation kinetics.

A logical next step is to extend the simulations to three dimensions. Since all simulations in this work were performed in two dimensions, the quantitative results cannot be directly extrapolated to 3D systems. For example, Lennard–Jones fluids exhibit different melting behaviour in two and three dimensions [29]. Aggregation kinetics are therefore expected to change as well when the system is extended to 3D.

Recent CG studies suggest modelling each bead as a single ionic species while retaining its net charge. Introducing important ion-ion interactions back into the system. Making the simulation more complex but could capture the behaviour of molten salts more accurately.

Finally, the simulation results should be benchmarked against experimental data, particularly aggregation rates and final cluster sizes. The theoretical framework also suggests a potential link between aggregation and sedimentation rates, since the dimensionless coefficients for sphere–sphere and sphere–plate interactions are closely related ($B'_{sp} \approx B', C'_{sp} = C'$). If validated, measuring one behaviour experimentally may allow prediction of the other. Before such cross-comparison is possible, the CG model should first be improved in the ways described above.

Molten Salt Reactor

The operating conditions in a molten salt reactor place the system deep in the primary-minimum aggregation regime. The attraction between particles is sufficiently strong that electrostatic repulsion becomes negligible within the DLVO framework. Consequently, the behaviour of the system will likely remain unchanged by a different choice of molten salt. Future research should therefore focus on controlling sedimentation rather than preventing.

One strategy to control sedimentation is to alter the interaction between NPs and reactor surfaces. Applying a surface potential on selected components may induce ion layering, which acts as an additional short-range repulsive barrier. Alternatively, hydrophobic or hydrophilic surface coatings could be used to either promote or suppress deposition, depending on the reactor component. Such approaches require careful evaluation of possible side effects, including corrosion and changes in thermal performance.

The sphere–plate potential can be used to estimate sedimentation behaviour by determining the minimum particle–wall separation required for irreversible behaviour. In turbulent flow, the viscous sublayer has a characteristic thickness of roughly 0.1–1 mm, which is orders of magnitude larger than the interaction range of DLVO forces. Thus, transport of NPs towards the wall is facilitated by hydrodynamic and thermophoretic effects. Coupling these transport models to estimate NP concentration near the wall will serve as an input for the MD model to predict final sedimentation rates.

10

Conclusion

This thesis developed a non-dimensional framework for classifying and predicting aggregation behaviour in colloidal systems. The DLVO potential was reduced to two dimensionless coefficients that represent the relative strength and effective interaction range of the electric double layer (EDL). These coefficients enable aggregation behaviour to be categorised into four distinct regimes. The framework was applied to coarse-grained (CG) molecular dynamics simulations to establish a first quantitative relation between these coefficients and aggregation kinetics. Finally, the framework was used to evaluate nanoparticle (NP) behaviour in molten salt reactors (MSRs) and to formulate recommendations for future research.

The DLVO potential was successfully reduced to two dimensionless coefficients, B'/D' and C'/D'. Four aggregation regimes were identified. In addition to the classical regimes, rapid aggregation, barrier limited aggregation, and stable dispersion, a fourth, semi-stable regime was discovered. Potentials in this regime fall within the barrier-limited region but behave similarly to either direct aggregation or stable dispersion. This addition refines regime classification and improves insight. The sphere–sphere geometry required the near-field approximation, which produced fixed regime boundaries. While suitable as a starting point, accurate modelling should ultimately include the full DLVO expression without this approximation.

The sphere–plate regime provides the full interaction behaviour over all surface separations and reveals size-dependent regime transitions. Small particles with a relatively thick EDL show an expanded barrier-limited regime, indicating reduced aggregation tendency. As particles grow, the EDL becomes small relative to particle size and the regime boundaries converge toward the sphere–sphere near-field case, effectively capturing plate–plate interactions.

A first quantitative relation between the dimensionless coefficients and aggregation kinetics was established using CG simulations. NPs were modelled as spherical clusters of 50 atoms, and the LiCl–KCl eutectic salt was represented as electrically neutral beads. The molten salt beads interacted using a Lennard–Jones potential. Decreasing computational cost by removing electrostatic interactions, but potentially oversimplifying interactions and losing accuracy. A parameter sweep across the coefficient space revealed that longer aggregation times occur when the potential amplitude decreases. Larger values of C'/D' (stronger EDL repulsion) reduce final aggregate size. However, the current model uses center-to-center distances, limiting physical accuracy and requiring refinement.

Applying the framework to molten salt reactors showed that the relevant coefficient values lie deep within the primary-minimum regime. Aggregation is therefore unavoidable and largely insensitive to surface charge or salt composition. Consequently, NP interactions in MSRs may be modelled using a Lennard–Jones potential, and future work should focus on controlling deposition rather than preventing aggregation.

In summary, this research presents a general framework able to predict colloidal aggregation using only two dimensionless parameters. Extending the model to three dimensions, exploring NP concentration effects, and benchmarking against experimental data will further improve and validate the framework.

References

[1] International Atomic Energy Agency. *Status of Molten Salt Reactor Technology*. Tech. rep. Accessed 26 Oct 2025. IAEA, 2021. URL: https://www-pub.iaea.org/MTCD/Publications/PDF/STI-DOC-010-489_web.pdf.

[2] Víctor Agmo Hernández. "An overview of surface forces and the DLVO theory". In: *ChemTexts* 9.4 (July 2023). DOI: 10.1007/s40828-023-00182-9.

[3] Didier Astruc. "Introduction: Nanoparticles in Catalysis". In: *Chemical Reviews* 120.2 (2020), pp. 461–463. DOI: 10.1021/acs.chemrev.8b00696.

[4] Peter Atkins, Julio de Paula, and Ronald Friedman. *Physical Chemistry: Quanta, Matter, and Change*. 2nd. Oxford University Press, 2013. ISBN: 9780199609819.

[5] Elena Bichoutskaia et al. "Electrostatic analysis of the interactions between charged particles of dielectric materials". In: *The Journal of Chemical Physics* 133.2 (July 2010). DOI: 10.1063/1.3457157.

[6] M Born et al. *Z. Phys.* 1926.

[7] Runlong Cai and Juha Kangasluoma. "The proper view of cluster free energy in nucleation theories". In: *Aerosol Science and Technology* 56.8 (2022), pp. 757–766. DOI: 10.1080/02786826.2022.2075250.

[8] David Leonard Chapman. "Li. a contribution to the theory of electrocapillarity". In: *The London, Edinburgh, and Dublin Philosophical Magazine and Journal of Science* 25.148 (Apr. 1913), pp. 475–481. DOI: 10.1080/14786440408634187.

[9] ENDURANCE Consortium. *EU Knowledge Hub for enabling Molten Salt Reactor safety development and deployment (ENDURANCE)*. European Commission Research and Innovation Action, Grant Agreement No. 101165896. Accessed: 2025-10-28. 2023. URL: https://www.endurance-msr-project.eu/.

[10] V. S. J. Craig, B. W. Ninham, and R. M. Pashley. "Direct Measurement of Hydrophobic Forces: A Study of Dissolved Gas, Approach Rate, and Neutron Irradiation". In: *Langmuir* 15.5 (1999), pp. 1657–1659. DOI: 10.1021/la9805793.

[11] B. V. Derjaguin and L. D. Landau. "Theory of the Stability of Strongly Charged Lyophobic Sols and of the Adhesion of Strongly Charged Particles in Solutions of Electrolytes". In: *Acta Physicochimica URSS* 14 (1941), pp. 633–662.

[12] LAMMPS Developers. *pair_colloid — Colloidal interaction potential in LAMMPS*. https://docs.lammps.org/pair_colloid.html. Accessed: 2025-10-23. Sandia National Laboratories, 2025.

[13] S. S. Dukhin and J. Lyklema. "Dynamics of colloid particle interaction". In: *Langmuir* 3.1 (1987), pp. 94–98. DOI: 10.1021/la00073a016. eprint: https://doi.org/10.1021/la00073a016. URL: https://doi.org/10.1021/la00073a016.

[14] T. Dumaire. "Advanced in the Chemistry of Molten Salt Fuels with Emphasis on Fission Products and Corrosion Products". Dissertation. Delft University of Technology, 2024. DOI: 10.4233/uuid:0752d005-7de4-4758-818f-08b30215f4d8. URL: https://doi.org/10.4233/uuid:0752d005-7de4-4758-818f-08b30215f4d8.

[15] Menachem Elimelech. *Particle deposition and aggregation: Measurement, modelling and Simulation*. Butterworth-Heinemann, 2010.

[16] Badawy M Elsheikh. "Safety assessment of molten salt reactors in comparison with light water reactors". In: *journal of radiation research and applied sciences* 6.2 (2013), pp. 63–70.

[17] Donald L Feke et al. "A formulation of the short-range repulsion between spherical colloidal particles". In: *The Journal of Physical Chemistry* 88.23 (1984), pp. 5735–5739.

[18] Generation IV International Forum. *Schematic of a Molten Salt Reactor*. Public website, Redirection Hub. Accessed: 2025-10-28. 2024. URL: https://www.gen-4.org/welcome-new-generation-iv-international-forums-public-website-redirection-hub.

[19] if available] Frederix [Initial or Full First Name. “Colloidal Stability of Nanoparticles in Molten Salts”. Accessed: 2025-10-27. MA thesis. Cambridge, MA: Massachusetts Institute of Technology, 2022. URL: https://dspace.mit.edu/handle/1721.1/XXXXX.

[20] G Frens and J.Th.G Overbeek. “Repeptization and the theory of electrocratic colloids”. In: *Journal of Colloid and Interface Science* 38.2 (1972), pp. 376–387. ISSN: 0021-9797. DOI: https://doi.org/10.1016/0021-9797(72)90253-6. URL: https://www.sciencedirect.com/science/article/pii/0021979772902536.

[21] Amalie L Frischknecht, Deaglan O Halligan, and Michael L Parks. “Electrical double layers and differential capacitance in molten salts from density functional theory”. In: *The Journal of Chemical Physics* 141.5 (2014).

[22] M. Gouy. “Sur La Constitution de la charge électrique à la surface d’un électrolyte”. In: *Journal de Physique Théorique et Appliquée* 9.1 (1910), pp. 457–468. DOI: 10.1051/jphystap:019100090045700.

[23] John Gregory. “Interaction of unequal double layers at constant charge”. In: *Journal of colloid and interface science* 51.1 (1975), pp. 44–51.

[24] David J. Griffiths. *Introduction to Electrodynamics*. 4th. London, UK: Pearson, 2013.

[25] Hugo C Hamaker. “The London—van der Waals attraction between spherical particles”. In: *physica* 4.10 (1937), pp. 1058–1072.

[26] Zhiqi He and Paschalis Alexandridis. “Nanoparticles in Ionic Liquids: Interactions and Organization”. In: *Physical Chemistry Chemical Physics* 17 (2015), pp. 18238–18261. DOI: 10.1039/C5CP01620G.

[27] Sophie Hermans. “Over 14,000 businesses on waiting list to connect to congested power grid”. In: *NL Times* (Oct. 2025). Accessed 26 Oct 2025. URL: https://nltimes.nl/2025/10/06/14000-businesses-waiting-list-connect-congested-power-grid.

[28] An Ho et al. “Exploring the benefits of molten salt reactors: An analysis of flexibility and safety features using dynamic simulation”. In: *Digital Chemical Engineering* 7 (2023), p. 100091.

[29] J. W. P. Hopping and C. J. Kennedy. “Communication: Studies of the Lennard-Jones fluid in 2, 3, and 4 dimensions highlight the need for a liquid-state 1/d expansion”. In: *The Journal of Chemical Physics* 144.23 (2016), p. 231101. DOI: 10.1063/1.4953828. URL: https://doi.org/10.1063/1.4953828.

[30] A. Hospital et al. “Molecular dynamics simulations: advances and applications”. In: *Advances and Applications in Bioinformatics and Chemistry* 8 (2015), pp. 37–47. DOI: 10.2147/AABC.S70333.

[31] Helgi I Ingólfsson et al. “The power of coarse graining in biomolecular simulations”. In: *Wiley Interdisciplinary Reviews: Computational Molecular Science* 4.3 (2014), pp. 225–248.

[32] International Atomic Energy Agency. *Nuclear Hydrogen Production*. Accessed 26 Oct 2025. 2025. URL: https://www.iaea.org/topics/non-electric-applications/nuclear-hydrogen-production.

[33] International Atomic Energy Agency. *Waste from Innovative Types of Reactors and Fuel Cycles*. Accessed 26 Oct 2025. IAEA Nuclear Energy Series, 2018. URL: https://www-pub.iaea.org/MTCD/Publications/PDF/PUB1822_web.pdf.

[34] Jacob N. Israelachvili and Richard Pashley. “The hydrophobic interaction is long range, decaying exponentially with distance”. In: *Nature* 300 (1982), pp. 341–342. DOI: 10.1038/300341a0.

[35] A. Jenet. “Molten salt reactors: Climate goals revive opportunities for previously discounted nuclear technology”. In: *Ceramic Tech Today* (Jan. 2025). Accessed 26 Oct 2025. URL: https://www.sciencedirect.com/science/article/pii/S0029549325006727.

[36] Soumil Y. Joshi and Sanket A. Deshmukh. “A review of advancements in coarse-grained molecular dynamics simulations”. In: *Molecular Simulation* 47.10-11 (2021), pp. 786–803. DOI: 10.1080/08927022.2020.1828583. eprint: https://doi.org/10.1080/08927022.2020.1828583. URL: https://doi.org/10.1080/08927022.2020.1828583.

[37] RJ Kedl. *Migration of a class of fission products (noble metals) in the Molten-Salt Reactor Experiment*. Tech. rep. Oak Ridge National Lab.(ORNL), Oak Ridge, TN (United States), 1972.

[38] Dae Han Kim et al. “Reverse water gas shift reaction catalyzed by Fe nanoparticles with high catalytic activity and stability”. In: *Journal of Industrial and Engineering Chemistry* 23 (2015), pp. 67–71. DOI: 10.1016/j.jiec.2014.07.043.

[39] Alexei A. Kornyshev. “Double-Layer in Ionic Liquids: Paradigm Change?” In: *The Journal of Physical Chemistry B* 111.20 (2007). PMID: 17469864, pp. 5545–5557. DOI: 10.1021/jp067857o. URL: https://doi.org/10.1021/jp067857o.

[40] EO Kraemer and St T Dexter. “The light-scattering capacity (tyndall effect) and colloidal behavior of gelatine sols and gels”. In: *The Journal of Physical Chemistry* 31.5 (2002), pp. 764–782.

[41] Sabbi Vamshi Krishna et al. “Performance Comparison of Julia with C and Python for Solving Computational Problems”. In: *International Conference on Advances in Computing and Data Sciences*. Springer. 2024, pp. 35–45.

[42] N. D. Lang and W. Kohn. “Theory of Metal Surfaces: Charge Density and Surface Energy”. In: *Physical Review B* 1.12 (1970), pp. 4555–4568. DOI: 10.1103/PhysRevB.1.4555.

[43] Raudah Lazim, Donghyuk Suh, and Sun Choi. “Advances in Molecular Dynamics Simulations and Enhanced Sampling Methods for the Study of Protein Systems”. In: *International Journal of Molecular Sciences* 21.17 (2020), p. 6339. DOI: 10.3390/ijms21176339. URL: https://www.mdpi.com/1422-0067/21/17/6339.

[44] John E Lennard-Jones. “Cohesion”. In: *Proceedings of the Physical Society* 43.5 (1931), p. 461.

[45] Wei Li, Xinyu Wang, and Zhihong Zhang. “Research on Numerical Integration Algorithm in Molecular Dynamics Simulation”. In: *2017 2nd International Conference on Image, Vision and Computing (ICIVC)*. Chengdu, China: IEEE, 2017, pp. 1122–1126. DOI: 10.1109/ICIVC.2017.7984712.

[46] Shihong Lin and Mark R. Wiesner. “Exact Analytical Expressions for the Potential of Electrical Double Layer Interactions for a Sphere–Plate System”. In: *Langmuir* 26.22 (2010), pp. 16638–16641. DOI: 10.1021/la103046w.

[47] Zhen Liu et al. “Understanding the stability mechanism of silica nanoparticles: The effect of cations and EOR chemicals”. In: *Fuel* 280 (2020), p. 118650. DOI: 10.1016/j.fuel.2020.118650. URL: https://doi.org/10.1016/j.fuel.2020.118650.

[48] Zilong Liu et al. “Understanding the stability mechanism of silica nanoparticles: The effect of cations and EOR chemicals”. In: *Fuel* 280 (2020). DOI: 10.1016/j.fuel.2020.118650.

[49] Boris I. Loukhovitski and Alexander S. Sharipov. “Molecular Collision Diameters and Electronic Polarizabilities: Inherent Relationship and Fast Evaluation”. In: *The Journal of Physical Chemistry A* 125.23 (2021). PMID: 34077208, pp. 5117–5123. DOI: 10.1021/acs.jpca.1c02201. URL: https://doi.org/10.1021/acs.jpca.1c02201.

[50] Leonardo Teixeira Pinto Meireles, Einar Madsen Storebø, and Ida Lykke Fabricius. “Effect of electrostatic forces on the porosity of saturated mineral powder samples and implications for chalk strength”. In: *Geophysics* 85.1 (2020), MR37–MR50.

[51] Vivian Merk et al. “In Situ Non-DLVO Stabilization of Surfactant-Free, Plasmonic Gold Nanoparticles: Effect of Hofmeister’s Anions”. In: *Langmuir* 30.14 (2014), pp. 4213–4222. DOI: 10.1021/la404556a. URL: https://doi.org/10.1021/la404556a.

[52] T. Moran and colleagues. *Advanced Nuclear Process Heat for Industrial Decarbonization*. Accessed 26 Oct 2025. Center for Climate and Energy Solutions (C2ES), July 2024. URL: https://www.c2es.org/wp-content/uploads/2024/07/Advanced-Nuclear-Process-Heat-for-Industrial-Decarbonization.pdf.

[53] Saroj K. Nayak et al. “Physics of Nickel Clusters: Energetics and Equilibrium Geometries”. In: *The Journal of Physical Chemistry A* 101.6 (1997), pp. 1072–1080. DOI: 10.1021/jp962720r.

[54] C. O’Melia. “Chapter 18: Fundamentals of particle stability”. In: *Interface Science and Technology* 10 (Dec. 2006). DOI: 10.1016/S1573-4285(06)80087-6.

[55] Iwuozor Kingsley Ogemdi. “Properties and uses of colloids: a review”. In: *Colloid and Surface Science* 4.2 (2019), p. 24.

[56] Hiroyuki Ohshima. “Approximate analytic expressions for the electrostatic interaction energy between two colloidal particles based on the modified Poisson-Boltzmann equation”. In: *Colloid and Polymer Science* 295.2 (Dec. 2016), pp. 289–296. DOI: 10.1007/s00396-016-4005-5.

[57] R. M. Pashley. “DLVO and hydration forces between mica surfaces in Li^+, Na^+, K^+, and Cs^+ electrolyte solutions: A correlation of double-layer and hydration forces with surface cation exchange properties”. In: *Journal of Colloid and Interface Science* 83.2 (1981), pp. 531–546. DOI: 10.1016/0021-9797(81)90348-9.

[58] Emanuele Petretto, Pablo Campomanes, and Stefano Vanni. “Development of a coarse-grained model for surface-functionalized gold nanoparticles: towards an accurate description of their aggregation behavior”. In: *Soft Matter* 19 (2023), pp. 3290–3300. DOI: 10.1039/d3sm00094j.

[59] A. Ravichandran and et al. “Interactions Governing the Dispersion of Silver Nanoparticles in Ionic Liquids: A Combined All-Atom and Coarse-Grained Molecular Dynamics Study”. In: *J. Phys. Chem. B* 129.42 (2025), pp. 11031–11042. DOI: 10.1021/acs.jpcb.5c03773.

[60] Reuters. “Dutch grid operator TenneT unlocks 9 GW via off-peak contracts to ease congestion”. In: (Apr. 2025). Accessed 26 Oct 2025. URL: https://www.reuters.com/business/energy/dutch-power-grid-operator-allocates-9-gw-via-off-peak-contracts-2025-04-07/.

[61] Eli Ruckenstein and Dennis Prieve. “Adsorption and desorption of particles and their chromatographic separation”. In: *AIChE Journal* 22 (Mar. 1976), pp. 276–283. DOI: 10.1002/aic.690220209.

[62] A. Satoh. “Chapter 11 - The Methodology of Simulations”. In: *Introduction to Molecular-Microsimulation of Colloidal Dispersions*. Ed. by A. Satoh. Vol. 17. Studies in Interface Science. Elsevier, 2003, pp. 160–183. DOI: https://doi.org/10.1016/S1383-7303(03)80039-X. URL: https://www.sciencedirect.com/science/article/pii/S138373030380039X.

[63] M. Scott Shell. *Advanced Molecular Dynamics Techniques: Thermostats*. Lecture Notes, ChE 210D. 2009. URL: http://www.ccl.net/chemistry.

[64] L. J. A. Siqueira and M. C. C. Ribeiro. “Molecular Dynamics Simulation Study on the Stability of Gold Nanoparticles in Ionic Liquids”. In: *J. Phys. Chem. C* 127 (2023), ????

[65] Leonardo J. A. Siqueira and Mauro C. C. Ribeiro. “A Molecular Dynamics Simulation Study on the Stability of Gold Nanoparticles in Ionic Liquids”. In: *The Journal of Physical Chemistry C* 119.33 (2015), pp. 18814–18824. DOI: 10.1021/acs.jpcc.5c02807.

[66] Theodros Solomon. “The definition and unit of ionic strength”. In: *Journal of Chemical Education* 78.12 (2001), p. 1691.

[67] Leonard Susskind. “Complexity and Newton’s laws”. In: *Frontiers in Physics* 8 (2020), p. 262.

[68] Kyoko K. Tanaka et al. “Free energy of cluster formation and a new scaling relation for the nucleation rate”. In: *The Journal of Chemical Physics* 140.19 (May 2014). DOI: 10.1063/1.4875803.

[69] Reid Tanaka. “Quantifying the adhesion of noble metal foulants on structural materials in a Molten Salt Reactor”. PhD thesis. Jan. 2017.

[70] Jos Thijssen. *Lecture Notes Statistical Physics*. Delft University of Technology, 2022.

[71] Daniel M Tibaduiza. “Electrostatic Force Between Two Colloidal Spheres”. In: *arXiv: Soft Condensed Matter* (2016). URL: https://api.semanticscholar.org/CorpusID:119610315.

[72] M. E. Tuckerman. “Understanding Modern Molecular Dynamics: Techniques and Applications”. In: *The Journal of Physical Chemistry B* 104.10 (2000), pp. 159–178. DOI: 10.1021/jp992433y.

[73] Kuo-Lun Tung et al. “Effect of calendering of filter cloth on transient characteristics of cake filtration”. In: *Separation and Purification Technology* 48.1 (2006), pp. 1–15. ISSN: 1383-5866. DOI: https://doi.org/10.1016/j.seppur.2005.07.026. URL: https://www.sciencedirect.com/science/article/pii/S1383586605002327.

[74] Peter G. Vekilov. “Nucleation”. In: *Crystal Growth & Design* 10.12 (Nov. 2010), pp. 5007–5019. DOI: 10.1021/cg1011633.

[75] Loup Verlet. “Computer ”Experiments” on Classical Fluids. I. Thermodynamical Properties of Lennard-Jones Molecules”. In: *Phys. Rev.* 159 (1 July 1967), pp. 98–103. DOI: 10.1103/PhysRev.159.98. URL: https://link.aps.org/doi/10.1103/PhysRev.159.98.

[76] E. J. W. Verwey and J. Th. G. Overbeek. *Theory of the Stability of Lyophobic Colloids: The Interaction of Sol Particles Having an Electric Double Layer*. Amsterdam: Elsevier, 1948.

[77] S. Vijayaram et al. “Applications of Green Synthesized Metal Nanoparticles in Biomedical and Environmental Fields”. In: *Journal of Industrial and Engineering Chemistry* 55 (2020), pp. 6195–6241. DOI: 10.1016/j.jiec.2014.07.043.

[78] Marie-Madeleine Walz et al. “Phase-Transferable Force Field for Alkali Halides”. In: *Journal of Chemical Theory and Computation* 14.11 (2018). PMID: 30300552, pp. 5933–5948. DOI: 10.1021/acs.jctc.8b00507. eprint: https://doi.org/10.1021/acs.jctc.8b00507. URL: https://doi.org/10.1021/acs.jctc.8b00507.

[79] World Nuclear Association. *Molten Salt Reactors*. Accessed 26 Oct 2025. Sept. 2024. URL: https://world-nuclear.org/information-library/current-and-future-generation/molten-salt-reactors.

[80] Andrew Worrall et al. “Molten salt reactors and associated safeguards challenges and opportunities”. In: (2018).

[81] Jianzhong Wu. “Understanding the Electric Double-Layer Structure, Capacitance, and Charging Dynamics”. In: *Chemical Reviews* 122.12 (2022). PMID: 35594506, pp. 10821–10859. DOI: 10.1021/acs.chemrev.2c00097. eprint: https://doi.org/10.1021/acs.chemrev.2c00097. URL: https://doi.org/10.1021/acs.chemrev.2c00097.

[82] Jianzhong Wu et al. “A classical density functional theory for interfacial layering of ionic liquids”. In: *Soft Matter* 7.23 (2011), p. 11222. DOI: 10.1039/c1sm06089a.

[83] Toru Yamada and Yohei Morinishi. “Application of Nosé–Hoover dynamics for coarse-graining molecular systems: An evaluation of reproducibility in Lennard-Jones systems”. In: *The Journal of Chemical Physics* 162.13 (2025), p. 134107. DOI: 10.1063/5.0254868.

[84] Junpei Yamanaka, Tohru Okuzono, and Akiko Toyotama. “Fundamentals of Colloidal Self-Assembly”. In: *Colloidal Self-Assembly*. Singapore: Springer Nature Singapore, 2023, pp. 13–40. ISBN: 978-981-99-5052-2. DOI: 10.1007/978-981-99-5052-2_2. URL: https://doi.org/10.1007/978-981-99-5052-2_2.

[85] J Li Yarnell et al. “Structure factor and radial distribution function for liquid argon at 85 K”. In: *Physical Review A* 7.6 (1973), p. 2130.

[86] Kenji Yasuoka and Mitsuhiro Matsumoto. “Molecular dynamics of homogeneous nucleation in the vapor phase. I. Lennard-Jones fluid”. In: *The Journal of Chemical Physics* 109.19 (Nov. 1998), pp. 8451–8462. DOI: 10.1063/1.477509.

[87] Seokjoo Yoon et al. “Analysis of electroneutrality of fission products in molten salt reactors”. In: *Progress in Nuclear Energy* 185 (2025), p. 105764. ISSN: 0149-1970. DOI: https://doi.org/10.1016/j.pnucene.2025.105764. URL: https://www.sciencedirect.com/science/article/pii/S0149197025001623.

[88] Hideki Yukawa. “On the Interaction of Elementary Particles”. In: *Proceedings of the Physico-Mathematical Society of Japan* 17 (1935), pp. 48–57.

[89] Chao Zhang and Michael Simpson. “Density of Molten Salt Mixtures of Eutectic LiCl-KCl Containing UCl3, CeCl3, or LaCl3”. In: *Journal of Nuclear Fuel Cycle and Waste Technology* 15 (June 2017), pp. 117–124. DOI: 10.7733/jnfcwt.2017.15.2.117.

A

Derivation

In this section, we present a concise derivation of the Linearized Poisson–Boltzmann equation starting from fundamental electrostatic principles. Beginning with Poisson's equation coupled to the Boltzmann distribution for mobile ions, we then introduce the Debye screening parameter and perform a linearization that yields the Debye–Hückel (linearized Poisson–Boltzmann) form. Key assumptions, such as dilute solution conditions, small potentials, and symmetric electrolytes, are identified at each step to clarify the regime of validity.

A.1. Electrostatics

The electrostatic potential $\varphi(\mathbf{r})$ generated by a charge distribution $\rho(\mathbf{r})$ is governed by Poisson's equation [24]:

$$\nabla^2\varphi(\mathbf{r}) = -\frac{\rho(\mathbf{r})}{\varepsilon}, \tag{A.1}$$

where $\varepsilon = \varepsilon_0\varepsilon_r$ is the permittivity of the medium and ρ has units of $\mathrm{C\,m^{-3}}$. In an ionic liquid, such as a molten salt, the charge density $\rho(\mathbf{r})$ combines contributions from fixed external charges (e.g. on electrodes or colloidal particles) and from the dissolved ions. These ions migrate under electrostatic forces, moving toward oppositely charged regions and away from like charges. Consequently, the local concentrations of cations and anions, $n_+(\mathbf{r})$ and $n_-(\mathbf{r})$, redistribute in response to the potential generated by external charges. The resulting ionic concentrations follow the Boltzmann distribution, whose derivation follows.

$$\rho(\mathbf{r}) = ze\,n_+(\mathbf{r}) - ze\,n_-(\mathbf{r}) + \rho_{\mathrm{ext}}(\mathbf{r}), \tag{A.2}$$

where z is the ionic valence and e the elementary charge. Far from any charged object, the solution is electrically neutral, so $n_\pm(\infty) = n_0$ and $\varphi(\infty) = 0$.

A.1.1. Boltzmann Distribution of Ions

In statistical thermodynamics, the chemical potential μ_j of species j measures the change in free energy when an additional ion is added at constant T, V, and composition. In an ideal gas mixture at temperature T, the chemical potential of species i at partial pressure p_i is given by

$$\mu_i(p_i) = \mu_i^\circ + k_BT\ln\!\left(\tfrac{p_i}{p^\circ}\right), \tag{A.3}$$

and the ideal-gas law relates p_i to the number density n_i via $p_i = n_ik_BT$. Hence one may equivalently express the chemical potential as

$$\mu_i(n_i) = \mu_i^\circ + k_BT\ln\!\left(\tfrac{n_i}{n^\circ}\right), \tag{A.4}$$

with $n^\circ = p^\circ/(k_BT)$. The two forms differ only in the choice of reference state. In a dilute ionic solution, each ion of species j carries charge q_j and experiences an electrostatic potential $\varphi(\mathbf{r})$. The local chemical potential is then

$$\mu_j(\mathbf{r}) = k_B T \, \ln\!\left(\tfrac{n_i}{n^\circ}\right) + q_j \, \varphi(\mathbf{r}), \tag{A.5}$$

The term $q_j \, \varphi(\mathbf{r})$ comes from deriving the chemical potential from the Helmholtz Free energy (F), $\mu_j = \left(\frac{\partial F}{\partial N_j}\right)_{T,V}$. Because the atoms are interacting with a potential $\varphi(\mathbf{r})$, this term is added to the Free energy F. For an ideal monatomic gas interacting with a potential $\varphi(\mathbf{r})$, the Helmholtz Free Energy is given by

$$F = -k_B T N \left[\ln\!\left(\frac{V}{\lambda_T^3 N} \right) - 1 \right] + N q_j \varphi(\mathbf{r}) \tag{A.6}$$

Another derivation to show that this theory holds is given by the Gibbs Free energy G. Which is given by $G = F + PV$. The chemical potential is given by

$$\mu_j \;=\; \left(\frac{\partial G}{\partial N_j}\right)_{P,T} \;=\; -\,k_B T \ln\!\left(\frac{V}{\lambda_T^3 N_j} \right) \tag{A.7}$$

and at equilibrium this must equal the bulk value

$$\mu_j = k_B T \ln\!\left(\tfrac{n_i}{n^\circ}\right) \tag{A.8}$$

Equating (A.5) and (A.8), then solving for $n_j(\mathbf{r})$, one obtains the Boltzmann distribution:

$$n_j(\mathbf{r}) = n_0 \exp\!\Big[-\frac{q_j \, \varphi(\mathbf{r})}{k_B T} \Big]. \tag{A.9}$$

Substituting (A.9) into Poisson's equation (3.1), yields the nonlinear Poisson–Boltzmann equation

$$\nabla^2 \varphi = \frac{2 z e n_0}{\varepsilon} \sinh\!\left(\frac{z e \varphi}{k_B T} \right) + \frac{\rho_{\text{ext}}(\mathbf{r})}{\varepsilon}. \tag{A.10}$$

Introducing the dimensionless potential $\Phi = ze\varphi / k_B T$ give rise to another constant. This will be the Debye screening parameter given as.

$$\kappa^2 = \frac{2 z^2 e^2 n_0}{\varepsilon k_B T}, \tag{A.11}$$

Physically, the inverse screening parameter κ^{-1} is the Debye length λ_D, and the two symbols are interchangeable. The Debye length is the $1/e$ decay distance of the potential in the linear regime, and it scales as $\lambda_D = \sqrt{\varepsilon k_B T / (2 z^2 e^2 n_0)}$. Higher ionic strength or valence increases κ (reducing λ_D), thus enhancing screening.

Substituting the dimensionless potential Φ with (A.11) the nonlinear Poisson-Boltzmann equation yields

$$\nabla^2 \Phi(\mathbf{r}) = \kappa^2 \sinh\!\big[\Phi(\mathbf{r})\big] + \frac{\rho_{\text{ext}}(\mathbf{r})}{\varepsilon}. \tag{A.12}$$

Non-Ideal (Ionic Liquid) Corrections

In a non-ideal electrolyte solution the appropriate thermodynamic variable is the activity $a_j = \gamma_j (n_j / n^\circ)$ rather than the raw concentration n_j. The chemical potential becomes

$$\mu_j = \mu_j^\circ + k_B T \ln a_j = \mu_j^\circ + k_B T \ln\!\left(\gamma_j \, \frac{n_j}{n^\circ} \right), \tag{A.13}$$

where γ_j is the activity coefficient. For dilute electrolytes the Debye–Hückel limiting law gives

$$\ln \gamma_j \approx -\frac{z_j^2 e^2}{8 \pi \varepsilon k_B T} \sqrt{I}, \qquad I = \tfrac{1}{2} \sum_i z_i^2 \, n_i, \tag{A.14}$$

showing that increasing ionic strength I lowers γ_j, reducing the effective activity. Formally, the equilibrium distribution becomes

$$a_j(\mathbf{r}) = a_0 \exp\Big[-\frac{q_j\,\varphi(\mathbf{r})}{k_B T}\Big], \tag{A.15}$$

but interpretation of a_j requires knowledge of $\gamma_j(I)$, obtained experimentally or via models such as Pitzer or UNIQUAC.

A.1.2. Linearized Poisson–Boltzmann Equation

For $|\Phi| \ll 1$ one linearizes $\sinh(\Phi) \approx \Phi$, reducing (A.12) to

$$\nabla^2\Phi(\mathbf{r}) = \kappa^2\Phi(\mathbf{r}) + \frac{\rho_{\text{ext}}(\mathbf{r})}{\varepsilon}. \tag{A.16}$$

For a point charge Q at the origin

$$\rho_{\text{ext}}(\mathbf{r}) = Q\,\delta^{(3)}(\mathbf{r}), \tag{A.17}$$

the solution of the Helmholtz–Poisson equation

$$\nabla^2\Phi - \kappa^2\Phi = \frac{Q}{\varepsilon}\,\delta^{(3)}(\mathbf{r}) \tag{A.18}$$

is the Yukawa potential

$$\Phi(r) = \frac{Q}{4\pi\varepsilon r}\,e^{-\kappa r}, \quad r = |\mathbf{r}|, \tag{A.19}$$

recovering the Coulomb form

$$\Phi_{\text{uns}}(r) = \frac{Q}{4\pi\varepsilon r}, \tag{A.20}$$

in the limit $\kappa \to 0$.

A.2. Ionic Strength of KCl–LiCl Eutectic (42 mol% LiCl)

We compute the molar concentration and the total ionic strength (I) for a KCl–LiCl eutectic mixture. The values used for the calculation are from Zhang and Simpson [89] and are summarized in Table A.1.

Table A.1: Physical properties of the eutectic LiCl (58 mol%)–KCl (42 mol%).

LiCl–KCl eutectic salt	
Temperature (K)	Density (g/cm^3)
773	1.6226

To calculate equation (3.5) is used. Therefore, we need to calculate the respective concentrations of the components of the mixture. Knowing the molar masses of the components and their ratios gives the concentrations of LiCl-KCl.

The individual concentrations of the mixture can be calculated using

$$c_i = \frac{\rho_t}{M} x_i, \tag{A.21}$$

where the c_i is the individual concentration of atom i, ρ_t is the total density of the mixture and M is the molar mass of the mixture. The individual concentrations are added to table A.2

Mixture molar mass (per mole of formula units) can be calculated with:
$M_{\text{mix}} = x_{\text{LiCl}} M_{\text{LiCl}} + (1 - x_{\text{LiCl}}) M_{\text{KCl}} = 61.043$ g mol^{-1}. With the individual concentrations of all the cations and the anions of the mixture. Following (3.5) the ionic strength of the mixture equals

Table A.2: Atomic and compound molar masses used in the calculation.

Species	Formula	Molar mass (g mol^{-1})	Eutectic concentration	Molar concentration
Lithium	Li	6.94	21%	5.58
Potassium	K	39.10	29%	7.71
Chlorine	Cl	35.45	50%	13.29
Lithium chloride	LiCl	42.39	42%	11.16
Potassium chloride	KCl	74.55	58%	15.41

$$I_{LiCl-KCl} = \frac{1}{2}\sum_i z_i^2 c_i = 13.29 \text{ mol L}^{-1} \tag{A.22}$$

These values highlight the extreme ionic strength of the melt and the correspondingly short electrostatic screening length.

B

Nucleation Theory

Nucleation is the process by which a new thermodynamic phase emerges within a parent phase, forming the microscopic origin of phase transitions such as vapor-to-liquid condensation or liquid-to-solid freezing. In this work, the focus lies on the nucleation of solute atoms in a liquid medium, where individual atoms assemble into stable solid clusters. This section outlines the framework of Classical Nucleation Theory (CNT), which describes how the competition between bulk free energy gain and interfacial free energy cost results in a nucleation barrier and a corresponding critical nucleus size. While CNT captures the first-order thermodynamic driving forces through the Gibbs free-energy landscape, it is based on several simplifying assumptions, including macroscopic surface tension and spherical nuclei, which become inaccurate at the nanoscale. Various extensions, such as density-functional approaches, non-classical pathways, and molecular-scale corrections, have improved the predictive capability of CNT. Nevertheless, a general and quantitatively accurate description of nucleation processes remains a subject of ongoing research.

B.1. Gibbs Free Energy of Nucleation

The chemical potential of monomers in a solution is given by

$$\mu_1 = \mu_1^* + k_B T \ln\Big(\frac{c_1}{c_{eq}}\Big), \tag{B.1}$$

where the subscript states that the chemical potential is for a single atom alone. Thus when the concentration grows above the equilibrium concentration, the chemical potential will rise as well.

In a supersaturated solution, i.e., one in which the solute chemical potential is higher than that of molecules in the crystal so that $\Delta\mu = \mu_{\text{solute}} - \mu_{\text{crystal}} > 0$, the formation of such a cluster leads to a free energy loss of $-n\Delta\mu$. On the other hand, the creation of the phase boundary with area S and surface free energy α between the cluster and the solution leads to a free energy gain [74].

If $\Delta\mu > 0$, then one atom goes from the solute to the crystal because it lower G by $-n\Delta\mu$ with $n = 1$ for only 1 atom.

However, creating a surface requires energy as it creates a barrier between two states. For example, breaking a material creates two surfaces. In this process many bonds where broken to obtain two surfaces, which requires energy. This gives a full equation for the change in Gibbs Free energy when n atoms forms a cluster

$$\Delta G = n + \gamma A(n). \tag{B.2}$$

Now, we consider the formation of spherical clusters with volume $V = \frac{4}{3}\pi r^3$ and a surface $A = 4\pi r^2$. Futhermore, we define $\Delta_v g$ as the difference in gibbs free energy when an atom is absorbed or added in the bulk material of the cluster. This is generally known for most of the materials and is used often in nucleation theory. In addition, it is also convenient to be able to convert the volume of the cluster to amount of atoms needed for that specific volume. The definition is given as $n = V/v_m$, where v_m stands for the molecular volume (the volume of 1 mol of a given particle).

So the change in gibbs free energy is given

$$\Delta G = -\frac{4}{3}\pi r^3 \Delta_v g + \gamma 4\pi r^2 \tag{B.3}$$

Furthermore, by looking at equations (B.2) and (B.3), it can be stated that $\Delta g_v = \Delta\mu / v_m = RT\ln(S)/v_m$.

Differentiating equation (B.3) with respect to radius will give the radius for which the Gibbs Free energy does not change. This will be the minimal radius that is required for spontaneous nucleation to happen. After this radius, theory suggests that the cluster keeps growing. In reality, as the cluster grows, the concentration and the chemical potential of the single atoms will decrease. This continue till $\Delta\mu = \mu_{\text{solute}} - \mu_{\text{crystal}} = 0$. When this equality holds the cluster will stop growing. The critical radius $r*$ and critical atoms $n*$ are given by [86]

$$\begin{aligned} r* &= \frac{2\gamma}{\Delta g_v} = \frac{2\gamma v_m}{RT\ln(S)} \\ n* &= \frac{4\pi}{3}\frac{r*^3}{v_m} = \frac{32\pi}{3}\frac{\gamma^3 v_m^2}{(RT\ln(S))^3} \end{aligned} \tag{B.4}$$

It is interesting to see that nucleation is not energy-favorable at first. This induces the single atoms to stay soluded, eventually increasing the concentration of single atoms. In conclusion, important to see that the critical amount of atoms decreases as the concentration of monomers increases far above the equilibrium concentration.

B.1.1. Nucleation in Molten Salt Reactors

The nucleation of metallic clusters, particularly those composed of noble metal fission products such as palladium, ruthenium, or molybdenum, is an important process in molten salt reactors (MSRs). A single metal atom lacks a complete coordination environment and therefore does not possess the full set of metallic bonds characteristic of the bulk solid phase. When two or more metal atoms approach each other, metallic bonds are formed through delocalised electron sharing, leading to the aggregation of atoms into stable clusters.

Nucleation can occur via two primary mechanisms: homogeneous and heterogeneous nucleation. In homogeneous nucleation, atoms of a single species bond together to form clusters of the same composition. Heterogeneous nucleation, on the other hand, involves the formation of clusters consisting of multiple atom types or the spontaneous nucleation of clusters at surfaces or interfaces. Rough surfaces in particular provide energetically favourable sites, reducing the nucleation barrier. Consequently, heterogeneous nucleation typically proceeds faster than homogeneous nucleation. A common example of this phenomenon is the formation of bubbles on the surface of a glass when champagne is poured, as the surface irregularities act as nucleation sites.

To describe the thermodynamic driving forces pf nucleation, the Gibbs free energy is introduced. This thermodynamic potential applies to systems at constant temperature T and pressure P, conditions relevant to MSRs where the pressure is regulated over the system volume. As the molten salt heats or cools, its density, and therefore the occupied volume at constant pressure, changes slightly. The Gibbs free energy quantifies the energetic feasibility of a process: a process proceeds spontaneously only when the change in Gibbs free energy is negative, $\Delta G \leq 0$ [4]. The general expression for the Gibbs free-energy change is given by [70]:

$$dG = VdP - SdT + \sum_j \mu_j dn_j \tag{B.5}$$

when expanded by substituting $dU = TdS - PdV + \mu dN$. Combine the Gibss-Duhem equation which is given by $\sum_j n_j\mu_j = 0$. This equation states that the chemical potential of one component of a mixture cannot change independently without the remaining chemical potentials changing as well. So we have

$$\Delta_r G = \mu\Delta N \tag{B.6}$$

Where the molar Gibbs free energy is defined as $G = nG_m$, this will be a convenient way to compare the Gibbs free energy with the chemical potential.

$$\mu = \left(\frac{\partial G}{\partial n}\right)_{p,T} = \left(\frac{\partial (n\, G_m)}{\partial n}\right)_{p,T} = G_m \tag{B.7}$$

When we have our clusters that undergo the reaction: $A \rightarrow B$, the chemical potential of both reactants will change by as

$$\mathrm{d}G = \mu_A \,\mathrm{d}n_A + \mu_B \,\mathrm{d}n_B = -\mu_A \,\mathrm{d}\xi + \mu_B \,\mathrm{d}\xi = \big(\mu_B - \mu_A\big)\,\mathrm{d}\xi \qquad \Rightarrow \qquad \left(\frac{\partial G_r}{\partial \xi}\right)_{T,P} = \mu_B - \mu_A \quad \text{(B.8)}$$

Where $\Delta_r G$ is in (J mol^{-1}). So we have that the Gibbs free energy of the reaction $A \rightarrow B$ is defined as $\Delta G_r = \mu_B - \mu_A$ or can be rephrased as the difference between the chemical potentials of the reactants.

To derive an expression for the Gibbs free energy that is dependent on pressure changes from equilibrium. The temperature is set constant as the number of particles $dT = 0, dN = 0$ so equation (B.5) becomes $dG = VdP$. Integrating the said equation gives

$$G(P_f) = G(P_i) + \int_{P_i}^{P_f} V dP \quad \text{(B.9)}$$

For incompressible liquids or solids, (B.9) is reduced to $G(P_f) = G(P_i) + V\Delta P$. For an ideal-gas the volume can be substituted by $V_m = RT/p$ so that we get the following equation.

$$\mu(T,P) \;=\; \mu^{ideal}(T) \;+\; RT\,\ln\!\left(\frac{P}{P^{ideal}}\right). \quad \text{(B.10)}$$

Applied to the simplest situation where two individual atoms from a cluster $2A_1 \rightarrow A_2$ gives the following:

$$\Delta_r G(2A_1 \rightarrow A_2) = \mu_2 - 2\mu_1 = \mu_2^{ideal} + RT\ln\left(\frac{P_2}{P^{ideal}}\right) - \mu_1^{ideal} - RT\ln\left(\left(\frac{P_1}{P^{ideal}}\right)^2\right) \quad \text{(B.11)}$$

Combining gives

$$\Delta_r G(2A_1 \rightarrow A_2) = \Delta_r G^{ideal} + RT\ln\left(\frac{P_2/P^{ideal}}{(P_1/P^{ideal})^2}\right). \quad \text{(B.12)}$$

Giving a general definition for a reaction of the kind $nA_1 \rightarrow A_n$

$$\Delta_r G(nA_1 \rightarrow A_n) = \Delta_r G^{ideal} + RT\ln\left(\frac{P_n/P^{ideal}}{(P_1/P^{ideal})^n}\right). \quad \text{(B.13)}$$

This is a definition that works for ideal gases. For the sake of simplicity this approach is taken. For more accurate values the fugacity should be added into the equations. In short, fugacity is the escaping tendency of a particular phase to any other. This is true for all liquids and is defined to correct the ideal-gas definition for the chemical potential as it does not account for interacting gasses. For a nearly incompressible phase, most liquids and solids, the fugacitiy is equal to the the standard pressure so the whole correction term goes to zero $\mu_{solid/liquid}(T,P) \approx \mu^{ideal}_{solid/liquid}(T)$.

The reason that the partial pressures have an effect on the reaction could be solved with a mind experiment. When a reaction at equilibrium is compressed (from a to b), the reaction responds by reducing the number of molecules in the gas phase.

Futhermore, using the thermodynamic equilibrium constant (K) that is the ratio of partial pressures at equilibirum, to descirbe the to calculate the the ideal reaction energy [4]

$$\Delta_r G^{ideal}_m(nA_1 \rightarrow A_n) = -RT\ln\left(\frac{P_n^{eq}/P^{ideal}}{(P_1^{eq}/P^{ideal})^n}\right) = -RT\ln\left(\frac{P_n}{P_1}\right) + RT(n-1)\ln\left(\frac{P_1}{P^{ideal}}\right). \quad \text{(B.14)}$$

Ultimately, when the whole equations are derived, the following equation will roll out

$$\Delta_r G_m(nA_1 \rightarrow A_n) = \Delta G_{\mathrm{barrier}} + RT\ln\frac{P_n}{P_1}. \quad \text{(B.15)}$$

An important conclusion is that the Gibbs free energy associated with cluster formation is not solely determined by the free-energy barrier illustrated in Figure B.1. It also depends on the partial pressures and the concentration of n-atom clusters, which together lower the overall reaction free energy. As fission products gradually dissolve

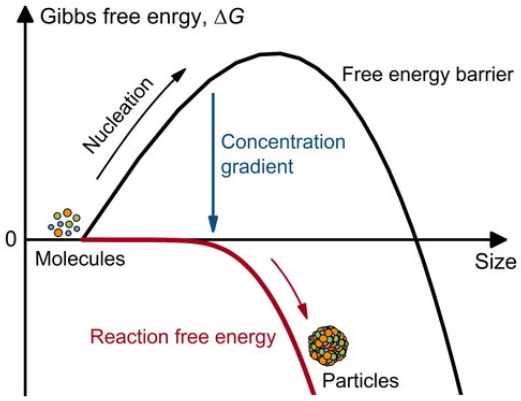

Figure B.1: Schematic representation of the Gibbs free-energy with different concentration. Indicating that an increase in the concentration of single molecules/atoms loweres the Gibbs Free Energy Barrier.

into the molten salt, the concentration of solute atoms increases, thereby reducing the energy required for cluster formation. Over time, this makes nucleation more favourable and eventually leads to the spontaneous formation of metallic clusters.

Although individual atoms can aggregate into clusters even when the Gibbs free-energy barrier remains positive, this process does not necessarily occur instantaneously. The atoms are not in a saturated state within the molten salt, and the diffusion coefficient becomes a key parameter in determining the likelihood of atomic encounters that lead to aggregation. As time progresses and the concentration gradient builds up, the reaction free energy approaches zero. At this point, an equilibrium is reached where the rate of cluster formation equals the rate of dissolution, provided that no additional atoms are introduced into the system.

Molecules forming part of a new cluster phase with a curved interface possess a higher potential than those in a flat configuration, meaning that additional surface energy is required for the formation of new clusters. This can be understood by considering that energy is needed to split a cluster into two smaller ones, as atomic bonds must be broken. The same reasoning applies to the nucleation process: dividing a single cluster into smaller ones increases the total surface area, which in turn increases the total surface energy required for stability [7].

C

Parameter variation study

In this chapter, a parameter study will be shown of the DLVO potential from Equation 3.25. In literature, not much is clear about aggregation of metal atoms in MSR. The parameter variation study will serve as a foundation to understand how the potential behaves under different parameter values. Each of the parameters will be varied over a wide range to get a good impression on the impact of the variation. Another reason this parameter study is conducted, is that some of the parameters in the potential could not be determined from literature. This uncertainty causes the probability that all simulation that would have run be considered very specific and not translatable to other studies or cases. For this particular reason, the parameter study is even extended to a non-dimensionalisation for the specific behavior of the potential. This study aims for the general understanding of the whole potential.

Bringing back the amount of parameters to two. Hereby, making it easier to identify the regions in a contour plot without loss of generality of understanding

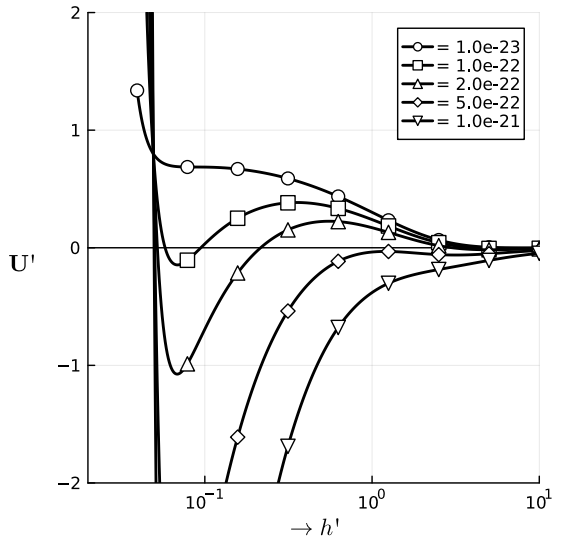

(a) Hamaker constant, $A_{Hamaker}$

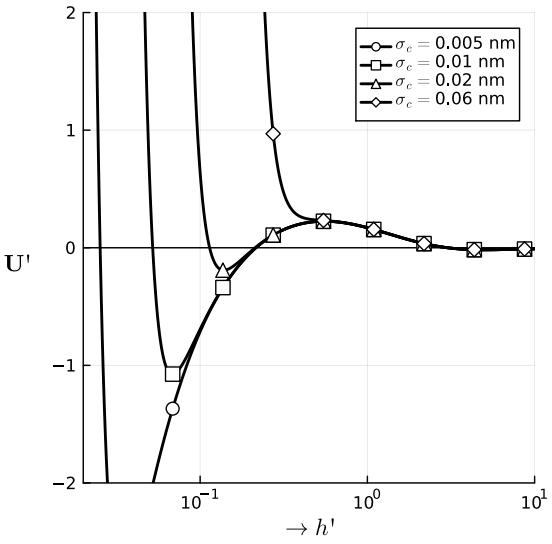

(b) Collision parameter, σ_c

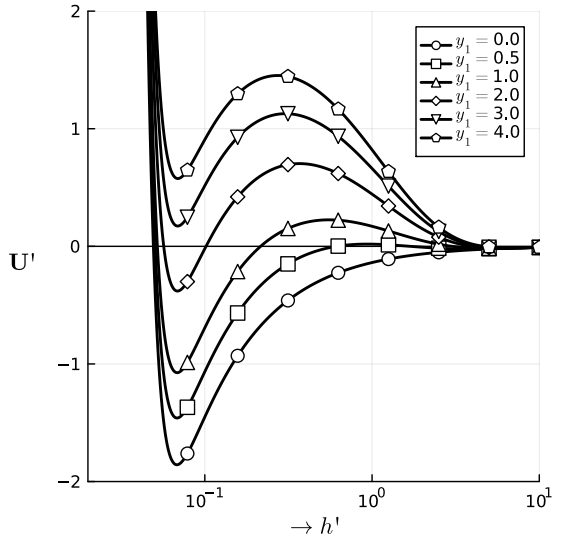

(c) Surface Potential, γ_1

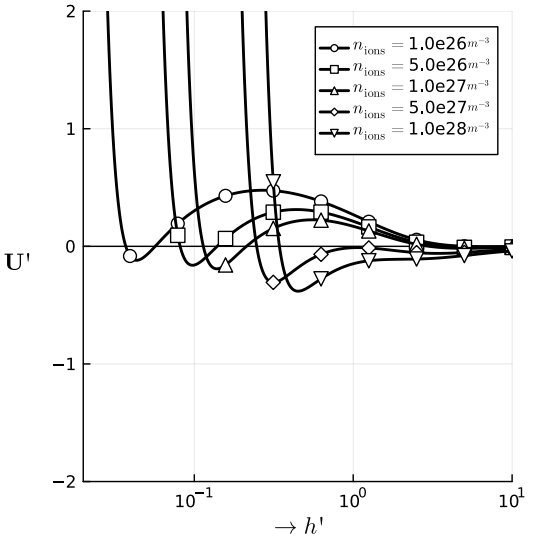

(d) Number of ions in solution, n_{ions}

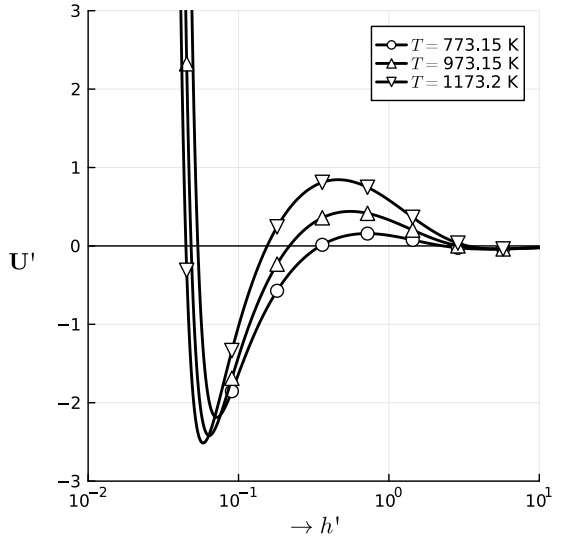

(e) Temperature, T

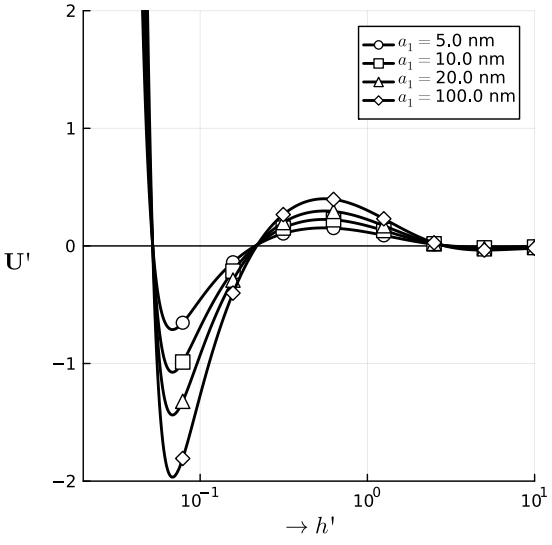

(f) Particle size, a_1

Figure C.1: Parameter Variation.

Figure C.1 shows the influence of several input parameters on the non-dimensional DLVO potential U'. Each subfigure varies one parameter while keeping the others fixed, illustrating how the shape of the potential changes.

In subfigure (a), the Hamaker constant A is varied. For larger values of A, the van der Waals attraction increases and the primary minimum becomes deeper. At low values of A the potential shows a repulsive barrier before aggregation can occur, whereas at higher values the barrier vanishes and aggregation is expected. This demonstrates how strongly A controls the overall potential.

Subfigure (b) presents the variation of the collision parameter σ. Smaller values of σ result in a steeper Born repulsion, while larger values soften the short-range repulsive wall. The effect is limited to very small separations but it determines how particles interact upon close contact.

In subfigure (c), the surface potential γ_1 is varied. Higher γ_1 strengthens the double-layer repulsion, raising the energy barrier and increasing the stability of the suspension. For lower γ_1, the potential becomes dominated by the attractive contribution and aggregation is more likely. This parameter is therefore crucial for setting the balance between attraction and repulsion.

Subfigure (d) shows the influence of the number of ions in solution, n_{ions}. Increasing the ionic concentration reduces the Debye length and thereby shortens the range of the electrostatic repulsion. At high n_{ions}, the potential becomes purely attractive and aggregation dominates. The ionic concentration thus controls the range of stability.

In subfigure (e), the temperature T is varied. Higher temperatures reduce the effective barrier height relative to $k_B T$, while lower temperatures increase it. Compared to the other parameters, the influence of temperature is less pronounced, but it still shifts the location of the minima and the overall stability.

Finally, subfigure (f) shows the variation of the particle radius a_1. Larger particles experience stronger van der Waals attraction, resulting in a deeper primary minimum. Smaller particles are relatively more stabilized by electrostatic repulsion. Particle size therefore shifts the balance between attractive and repulsive forces.

The parameter variation highlights that the DLVO potential is highly sensitive to the input parameters. In particular, the Hamaker constant A and the surface potential γ_1 play decisive roles in determining whether the system is stable, metastable, or unstable. Both of these parameters are, however, difficult to measure or estimate reliably. Furthermore, different combinations of parameters may produce similar potential curves, leading to the same simulated behaviour. For this reason, a generalized description is desired. In the following, the potential is expressed in terms of the dimensionless ratios B'/D' and C'/D', which allows for a universal classification of the interaction regimes independent of the precise parameter values.

C.1. Overfitting

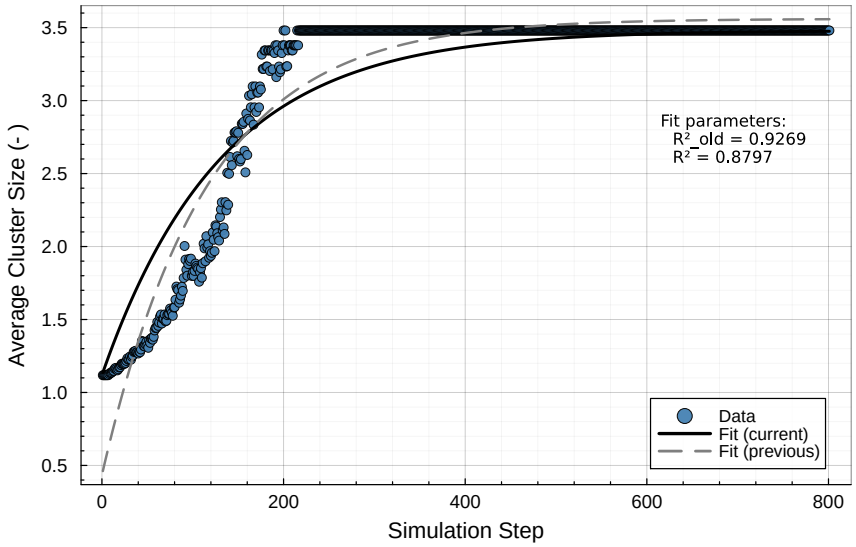

Figure C.2: Evolution of the average cluster size during the simulation. The blue markers represent the recorded data, the black line indicates the fitted model, and the dashed gray line shows the original fit for comparison. Only the initial growth regime is fitted to prevent overfitting, as discussed in Section 7.6.

Figure C.2 shows the evolution of the average cluster size together with two fitted models used for comparison. Both models reproduce the general trend of rapid early growth followed by saturation. However, the full three-parameter fit (dashed line) begins to deviate from the physical behavior at later stages, indicating overfitting. By constraining the final cluster size and initial condition, the simplified model (solid line) maintains a lower coefficient of determination ($R^2 = 0.8797$) but provides a more physically consistent representation of the aggregation dynamics.

D

Validation Molly: Argon simulation

In this chapter, validation of the Julia simulation with the Molly package will be shown. The results of the Argon simulation will be presented, hereby comparing the non-dimensionalised pressure with literature values from Verlet paper. As well as the radial distribution function for different phases will be compared. Furthermore, the regions for different behavior are calculated and presented in a heatmap with the non-dimensionalised coefficients, who are introduced in chapter 3.

D.1. Validation

To validate the simulation software as well as the Molly package in Julia, an argon simulation is carried out. The literature values are taken from the Verlet paper [75] and from a paper with published radial distribution function values of liquid argon [85].

To validate if the system works, it is important to calculate multiple observables and compare the values to the literature. This paper covers the pressure and the pair correlation function.

Pressure
The pressure can be calculated using the virial theorem:

$$\frac{\beta P}{\rho} = 1 - \frac{\beta}{3N} \left\langle \frac{1}{2} \sum_{i,j} r_{ij} \frac{\partial U}{\partial r_{ij}} \right\rangle \tag{D.1}$$

In this equation, β is defined as $\frac{1}{k_B T}$, where k_B is the Boltzmann constant and T is the temperature; P is the pressure, ρ is the density, U is the potential energy, and r_{ij} is the distance between particles i and j. The angle brackets denote ensemble averaging.

Pair correlation
Also known as the radial distribution function, the pair correlation function measures the probability of finding a particle at a distance r away from a reference particle. The pair correlation function can be computed in the following way:

$$g(r) = \frac{2V}{N(N-1)4\pi r^2 \Delta r} \langle n(r) \rangle \tag{D.2}$$

The result will be a histogram of all particle pairs within a distance [r, r + Δr].

A system of 864 particles is initialised in a face centred cubic (fcc) lattice, which corresponds to the crystal structure of solid argon. The lattice constant is determined from the dimensionless density ρ^* specified as an input parameter. The side length of the cubic simulation box is set to six times the lattice constant. Initial particle velocities are drawn from the Maxwell–Boltzmann distribution at the specified dimensionless temperature.

Since the system is not yet in equilibrium, the simulation is first allowed to evolve and the particle velocities are subsequently drawn from an external heat bath with the Andersen Thermostat, described in Chapter 7

$$\lambda = \sqrt{\frac{(N-1)\,3k_BT}{\sum_i m_i v_i^2}} \tag{D.3}$$

After the rescaling step, the pressure is calculated as the time average of the logged pressure values during the simulation. The results are shown in Figure D.1.

The simulated pressures for argon at various temperatures and densities showed good agreement with the reference data in the low- to medium-density and temperature regimes. Deviations were observed at low temperatures combined with high densities, where the simulated pressures were significantly lower than experimental values. These discrepancies are likely due to the simplified model used in the validation, which considered only Lennard-Jones interactions.

Figure D.2 shows the radial distribution function for the solid, liquid and gas phases. The solid phase exhibits a highly ordered structure, which is reflected by the sharp and periodic peaks. These peaks indicate that particles are positioned at well defined separation distances, consistent with a crystalline lattice. The liquid phase still shows positional correlation between neighbouring particles, although this correlation decays with increasing distance. In contrast, the gas phase displays no structural ordering and the radial distribution function approaches unity, meaning that particles are randomly distributed throughout the domain.

Since this research does not operate within low-temperature regimes, the accuracy of `Molly.jl` is sufficient for the intended simulations.

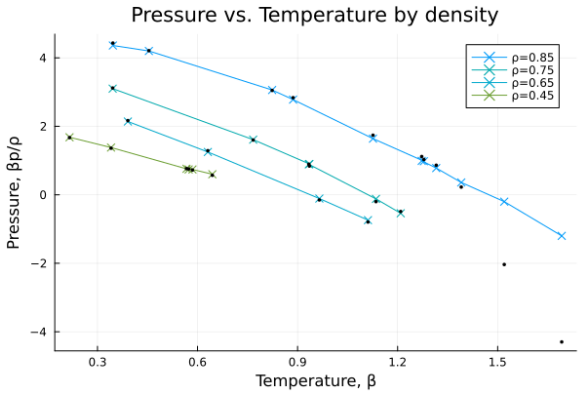

Figure D.1: Comparison between the simulated and Verlet's data. The solid lines correspond to Verlet's data. While the dots represent the simulated data.

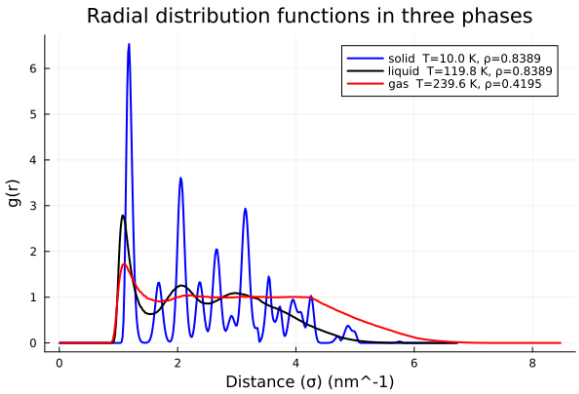

Figure D.2: The simulated radial distribution function for all phases of argon.